AIP Applied Physics Reviews

Compound semiconductor alloys: From atomic-scale structure to bandgap bowing

C. S. Schnohr

Citation: Applied Physics Reviews **2**, 031304 (2015); doi: 10.1063/1.4930002
View online: http://dx.doi.org/10.1063/1.4930002
View Table of Contents: http://scitation.aip.org/content/aip/journal/apr2/2/3?ver=pdfcov
Published by the AIP Publishing

Articles you may be interested in

Atomic-scale structure, cation distribution, and bandgap bowing in Cu(In,Ga)S2 and Cu(In,Ga)Se2
Appl. Phys. Lett. **103**, 081905 (2013); 10.1063/1.4819225

A simple analysis of interband absorption in quantum well structure of III-V ternary and quaternary semiconductors
J. Appl. Phys. **111**, 103104 (2012); 10.1063/1.4718414

Nonlinear variations in the electronic structure of II–VI and III–V wurtzite semiconductors with biaxial strain
Appl. Phys. Lett. **98**, 152108 (2011); 10.1063/1.3578193

Universal scaling of semiconductor nanowires bandgap
Appl. Phys. Lett. **95**, 073106 (2009); 10.1063/1.3211128

Phase diagram, chemical bonds, and gap bowing of cubic In x Al 1−x N alloys: Ab initio calculations
J. Appl. Phys. **92**, 7109 (2002); 10.1063/1.1518136

AIP Journal of Applied Physics

Journal of Applied Physics is pleased to announce André Anders as its new Editor-in-Chief

This article is copyrighted as indicated in the article. Reuse of AIP content is subject to the terms at: http://scitation.aip.org/termsconditions. Downloaded to IP: 131.169.38.71 On: Tue, 17 Nov 2015 09:25:17

CrossMark

APPLIED PHYSICS REVIEWS

Compound semiconductor alloys: From atomic-scale structure to bandgap bowing

C. S. Schnohr[a)]

Institut für Festkörperphysik, Friedrich-Schiller-Universität Jena, Max-Wien-Platz 1, 07743 Jena, Germany

(Received 20 May 2015; accepted 19 August 2015; published online 18 September 2015)

Compound semiconductor alloys such as $In_xGa_{1-x}As$, $GaAs_xP_{1-x}$, or $CuIn_xGa_{1-x}Se_2$ are increasingly employed in numerous electronic, optoelectronic, and photonic devices due to the possibility of tuning their properties over a wide parameter range simply by adjusting the alloy composition. Interestingly, the material properties are also determined by the atomic-scale structure of the alloys on the subnanometer scale. These local atomic arrangements exhibit a striking deviation from the average crystallographic structure featuring different element-specific bond lengths, pronounced bond angle relaxation and severe atomic displacements. The latter, in particular, have a strong influence on the bandgap energy and give rise to a significant contribution to the experimentally observed bandgap bowing. This article therefore reviews experimental and theoretical studies of the atomic-scale structure of III-V and II-VI zincblende alloys and I-III-VI_2 chalcopyrite alloys and explains the characteristic findings in terms of bond length and bond angle relaxation. Different approaches to describe and predict the bandgap bowing are presented and the correlation with local structural parameters is discussed in detail. The article further highlights both similarities and differences between the cubic zincblende alloys and the more complex chalcopyrite alloys and demonstrates that similar effects can also be expected for other tetrahedrally coordinated semiconductors of the adamantine structural family. © *2015 AIP Publishing LLC*.
[http://dx.doi.org/10.1063/1.4930002]

TABLE OF CONTENTS

I. INTRODUCTION 1
A. Compound semiconductor alloys 1
B. Scope and organization of the paper 4
II. X-RAY ABSORPTION SPECTROSCOPY 4
III. ZINCBLENDE MATERIALS 5
A. Atomic-scale structure 7
1. First nearest neighbor shell 7
2. Second nearest neighbor shell 9
3. Third nearest neighbor shell 12
4. Bond angles 13
B. Bond stretching and bond bending 14
1. Valence force field model 14
2. Thermal vibrations of atoms 15
C. Modeling of structural parameters 17
1. Models for the dilute limit 17
2. Models for the whole compositional range 18
3. Cluster and supercell calculations 20
4. Comparison of different first shell models 20
5. Modeling of higher shells 21
D. Atomic displacements 23
E. Bandgap bowing 25
1. Experimental bowing parameters 25
2. Theoretical models 26
3. Volume deformation, charge redistribution, and structural relaxation . . 28
4. Structural and electronic effects 29
IV. CHALCOPYRITE MATERIALS 30
A. Atomic-scale structure 32
B. Anion displacement 35
C. Bandgap bowing 36
D. Local electronic states 38
V. CONCLUSIONS AND OUTLOOK 39

I. INTRODUCTION

A. Compound semiconductor alloys

Compound semiconductor alloys have received tremendous attention over the last decades due to their enormous potential for application in electronic, optoelectronic, and photonic devices. III-V ternary alloys such as $In_xGa_{1-x}As$, $In_xGa_{1-x}P$, or $GaAs_xP_{1-x}$ are increasingly employed as light emitting diodes and lasers, infrared detectors, modulators, high mobility transistors, field effect transistors, and power amplifiers.[1–10] Multi-junction concentrator solar cells based on ternary III-V alloys have reached a record efficiency of

a)Electronic mail: c.schnohr@uni-jena.de

 © 2015 AIP Publishing LLC

This article is copyrighted as indicated in the article. Reuse of AIP content is subject to the terms at: http://scitation.aip.org/termsconditions. Downloaded to IP: 131.169.38.71 On: Tue, 17 Nov 2015 09:25:17

more than 44%.[11,12] The development of high-quality GaN and GaN based ternary alloys such as $Ga_xAl_{1-x}N$ and $In_xGa_{1-x}N$ has paved the way for efficient blue light emitting diodes and was awarded the 2014 Nobel Prize in Physics.[13] Applications of II-VI ternary alloys such as $Hg_xCd_{1-x}Te$, $Cd_xZn_{1-x}Te$, or $Cd_xZn_{1-x}Se$ range from infrared and X-ray detectors to light emitting diodes and nanoparticle lasers.[14–22] The more complex I-III-VI_2 quaternary or pentanary alloys are most prominently used for thin film photovoltaics. Solar cells based on the $CuIn_xGa_{1-x}(Se_yS_{1-y})_2$ system have repeatedly reached efficiencies well above 20% with a current record of 21.7% thus closing the gap to silicon-based technologies.[23–25] Furthermore, these record efficiencies have been achieved on both conventional glass substrates and flexible polymer foils.[25] The latter, in particular, offers tantalizing new applications in the fields of architecture and product design.

The basis for the success of all these semiconductor alloys is the possibility to purposefully tune the material properties by adjusting the alloy composition. This is due to the fact that many physical properties of these alloys change continuously between the values of the corresponding parent compounds. As an example, Fig. 1 displays the lowest bandgap energy, E_g, as a function of the lattice constant, a, for selected III-V and II-VI ternary alloys. Clearly, by choosing a suitable material with the appropriate composition, E_g or a can be selected within a wide parameter range. Alloying cations and anions, like in $In_xGa_{1-x}As_yP_{1-y}$, even allows to adjust both bandgap energy and lattice constant independently.[26] Semiconductor alloys thus provide a large and versatile group of materials that offer a wide range of physical properties highly suitable for advanced device applications.

Many III-V and II-VI semiconductors crystallize in the cubic zincblende structure (space group $F\bar{4}3m$) shown schematically in Fig. 2(c). It can be derived from the simpler diamond structure (space group $Fd\bar{3}m$) shown in Fig. 2(a), by populating one of the two crystallographic sites with the group-III or group-II cations and the other with the group-V

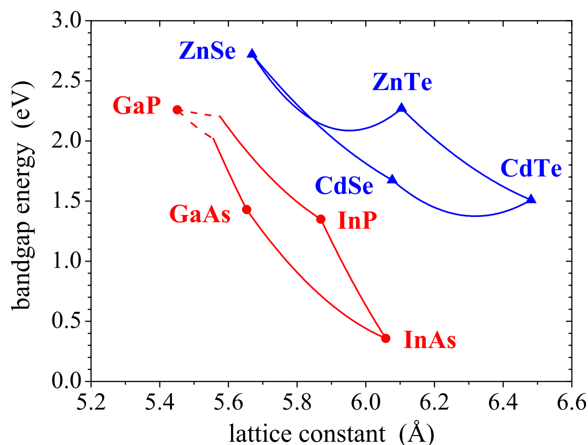

FIG. 1. Lowest bandgap energy versus lattice constant for selected III-V (red) and II-VI (blue) ternary semiconductor alloys with zincblende structure.[26] Solid and dashed lines represent direct and indirect bandgaps, respectively.

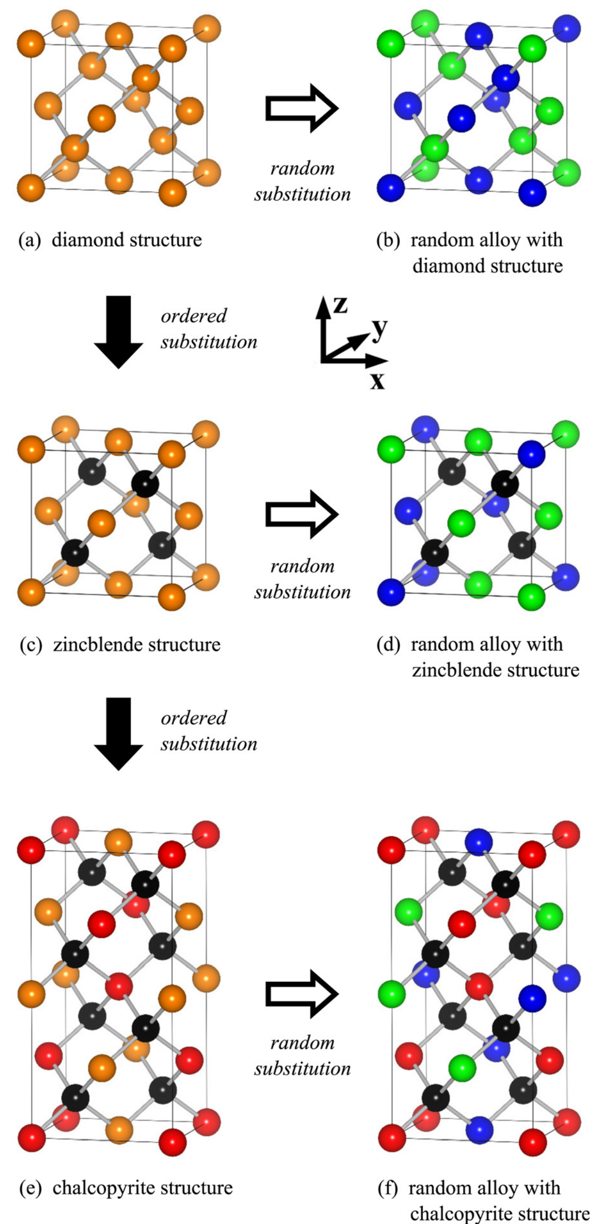

FIG. 2. Schematics of the tetrahedrally coordinated (a) diamond, (c) zincblende, and (e) chalcopyrite structure. Population of the two different lattice sites of the diamond structure with cations and anions yields the zincblende structure. Ordered substitution of one lattice site in the zincblende structure with two different atomic species leads to a number of possible structures one of which is the chalcopyrite structure. In contrast, random substitution of a lattice site with two different atoms leads to an alloy with the same crystal structure as the parent compounds as shown in panels (b), (d), and (f). Images created with VESTA.[29]

or group-VI anions thereby creating two distinct sublattices. Due to the tetrahedral coordination of these adamantine structures,[27,28] each cation is bonded to four anions and each anion is bonded to four cations.

Semiconductor alloys typically crystallize in the same crystal structure as the parent compounds. Mixing two group-IV semiconductors with the diamond structure such as Ge and Si yields a Ge_xSi_{1-x} alloy, where each lattice site of the diamond structure is occupied randomly by either Ge or Si atoms as shown schematically in Fig. 2(b). For ternary $A_xB_{1-x}C$ or CA_xB_{1-x} alloys with the zincblende structure,

This article is copyrighted as indicated in the article. Reuse of AIP content is subject to the terms at: http://scitation.aip.org/termsconditions. Downloaded to IP: 131.169.38.71 On: Tue, 17 Nov 2015 09:25:17

one of the two sublattices is occupied solely by the C atoms while the other sublattice is populated randomly with the isovalent A and B atoms (see Fig. 2(d)). In contrast, a new crystal structure is obtained if the occupation of the mixed sublattice with the two different atomic species occurs in an ordered periodic manner. One possible structure that can result from such an ordered substitution is the chalcopyrite structure (space group $I\bar{4}2d$) shown in Fig. 2(e).

The chalcopyrite structure is typically observed for the ternary I-III-VI_2 compounds that are derived from the II-VI zincblende semiconductors by replacing the group-II atoms with equal portions of group-I and group-III atoms. Each of these cations is still bonded to four group-VI anions; however, the anions are now bonded to two group-I and two group-III first nearest neighbors. This leads to a doubling of the unit cell and consequently to two different lattice constants, a and c. Ideally, the ratio $\eta = c/2a$ equals one and the anions occupy the ideal tetrahedral lattice site characterized by the fractional coordinates $(x, y, z) = (1/4, 1/4, 1/8)$ within the chalcopyrite unit cell. Due to the different physical and chemical properties of the group-I and group-III cations, however, many chalcopyrite materials exhibit a tetragonal distortion given by $\eta \neq 1$ and a displacement of the anions away from the ideal tetrahedral site characterized by $x \neq 1/4$. The latter is accompanied by two unequal bond lengths, d_I and d_{III}. Chalcopyrite materials are thus intrinsically more complex than zincblende semiconductors but they still feature the characteristic tetrahedral coordination central to the structures of the adamantine family. A random alloy is again formed by mixing two chalcopyrite compounds such that one crystallographic site is occupied randomly by two different but isovalent elements as shown schematically in Fig. 2(f).

For most semiconductor alloys, the lattice constants a_A and a_B of the parent compounds are not identical and the alloy lattice constant, $a(x)$, changes more or less linearly with composition x between the two end values

$$a(x) = xa_A + (1-x)a_B = A' + B'x, \tag{1}$$

where $A' = a_B$ and $B' = a_A - a_B$. This behavior is known as Vegard's Law[30] and has been observed for most zincblende and chalcopyrite semiconductor alloys using X-ray or neutron diffraction techniques.[26,31–45] The virtual crystal approximation (VCA) therefore assumes a perfect crystal structure for the random alloy where each atom is located at the ideal lattice site and the lattice constant is given by Eq. (1).[46] As a consequence, the A and B atoms of the mixed sublattice are surrounded by the same local structural environment. In particular, they both have the same first nearest neighbor bond length, $d_A = d_B$, which changes linearly with alloy composition x and the bond angles remain unchanged. The VCA model has been used extensively in the literature due to its inherent simplicity. It does, however, fail to fully explain the composition dependence of other properties such as the bandgap energy, E_g, which changes nonlinearly for many semiconductor alloys. In most cases, E_g can be described by a quadratic dependence of the form

$$\begin{aligned} E_g(x) &= xE_g^A + (1-x)E_g^B - bx(1-x) \\ &= A'' + B''x + C''x^2, \end{aligned} \tag{2}$$

with $A'' = E_g^B$, $B'' = E_g^A - E_g^B - b$, and $C'' = b$. The first two terms in this equation represent the weighted average of the bandgaps of the binary parent compounds

$$\bar{E}_g(x) = xE_g^A + (1-x)E_g^B. \tag{3}$$

The difference $\Delta E_g(x)$ between the average bandgap, $\bar{E}_g(x)$, and the alloy bandgap, $E_g(x)$, is called the bandgap bowing and is given by

$$\Delta E_g(x) = \bar{E}_g(x) - E_g(x) = bx(1-x). \tag{4}$$

In order to fully understand this bandgap bowing, the *local* atomic arrangements in semiconductor alloys have to be considered. As it turns out, this atomic-scale structure shows a striking deviation from the VCA model and thus from the average long-range crystallographic structure. It has been pointed out already very early that the lattice mismatch in semiconductor alloys can also be accommodated by a change in the bond angles rather than by a change in the bond lengths.[47] In the extreme case, the two first nearest neighbor distances, d_A and d_B, are independent of composition x and identical to those of the parent compounds while the lattice mismatch is accommodated entirely by an adjustment of the bond angles.

The atomic-scale structure of semiconductor alloys, in particular, the extent of bond length and bond angle relaxation has been extensively studied using X-ray absorption spectroscopy (XAS). This technique measures the X-ray absorption coefficient as a function of X-ray energy above a given absorption edge. The energy-dependent fine structure of the absorption coefficient depends on the atomic environment of the absorbing atoms and thus provides element-specific local structural parameters such as interatomic distances, coordination numbers, and measures for structural and thermal disorder.[48–50] XAS can be applied to both ordered and disordered systems making it an extremely powerful technique for structural analysis of advanced semiconductor materials.[51] Using XAS, the d_A and d_B bond lengths of a vast number of III-V, II-VI, and I-III-VI_2 semiconductor alloys were shown to be very different from each other. Furthermore, they remain nearly constant over the whole compositional range even if the lattice constants change considerably. The element-specific bond lengths are thus much closer to the values of the corresponding parent compounds than to the ones predicted by the VCA and the lattice mismatch is accommodated primarily by bond angle relaxation. Consequently, significant displacements of the atoms from their ideal lattice sites are observed in nearly all semiconductor alloys. Interestingly, these local atomic arrangements have a strong influence on many important material properties most prominently the bandgap energy. It is therefore the aim of this paper, to review both experimental and theoretical studies of the atomic-scale structure in compound semiconductor alloys and to discuss the correlation between these

This article is copyrighted as indicated in the article. Reuse of AIP content is subject to the terms at: http://scitation.aip.org/termsconditions. Downloaded to IP: 131.169.38.71 On: Tue, 17 Nov 2015 09:25:17

subnanometer structural parameters and the characteristic bandgap bowing.

B. Scope and organization of the paper

The review is focused on *compound* semiconductor alloys such as III-V and II-VI ternary alloys and I-III-VI_2 quaternary alloys that feature distinct cation and anion sublattices. The atomic-scale structure of group-IV semiconductor alloys such as Ge_xSi_{1-x} has also been studied extensively using both experimental[52–57] and theoretical[58,59] techniques and was recently reviewed in Ref. 60. While it shows many similarities with the local structure of compound semiconductor alloys, it also exhibits some unique features and will not be discussed here. Regarding the III-V and II-VI ternary alloys, the paper mainly concentrates on materials with the *zincblende* structure although some results will also be presented for materials with other crystal structures such as the nitride alloys. Among the I-III-VI_2 alloys with *chalcopyrite* structure, Cu(In,Ga)Se_2 and Cu(In,Ga)S_2 are so far the only materials for which detailed experimental studies of the atomic-scale structure have been reported. These works will be reviewed to highlight both the similarities with the ternary III-V and II-VI alloys and the differences arising from the increased complexity of the chalcopyrite structure compared to the zincblende structure.

Different types of short- and long-range order have been observed for some III-V and II-VI ternary alloys depending on the growth conditions (see Refs. 26, 61–63, and references therein). These structural modifications can affect many material properties and thus present another possibility to purposefully tailor semiconductor alloys. However, the correlation between growth conditions, type and degree of ordering, and alloy properties is complex and presents a large field of its own. The focus of this review is therefore on *random* semiconductor alloys with no short- or long-range order. Moreover, the paper is focused on alloys with *one mixed sublattice* including III-V and II-VI ternary alloys and I-III-VI_2 quaternary alloys. Systems with two mixed sublattices show very similar features yet the additional degrees of freedom increase the complexity of the material. For example, preferential bonding between the two different cation and anion species has been observed for several III-V and II-VI $A_xB_{1-x}C_yD_{1-y}$ quaternary alloys.[64–66] Finally, the review concentrates on studies of *bulk* semiconductor alloys although the effects of tensile or compressive strain on the atomic-scale structure of epitaxial thin films is discussed for ternary alloys with the zincblende structure.

The paper is organized as follows. Section II constitutes a very brief introduction to XAS highlighting its characteristic features that allow the study of local structural parameters in semiconductor alloys. Section III then deals with III-V and II-VI ternary alloys that crystallize in the zincblende structure presenting first the experimental findings for the atomic-scale structure. This is followed by a discussion of the competing mechanisms of bond stretching and bond bending. Subsequently, different approaches to model the atomic-scale structure of ternary semiconductor alloys are reviewed and the atomic displacements associated with the local structural arrangements are analyzed. The last part of Sec. III presents a detailed discussion of the correlation between atomic-scale structure and bandgap bowing in these zincblende semiconductor alloys. Section IV reviews studies of Cu(In,Ga)Se_2 and Cu(In,Ga)S_2 alloys with chalcopyrite structure elaborating first on the atomic-scale structure and anion displacement followed by a discussion of the bandgap energy and the local electronic states. It builds on the ideas and concepts explained in detail in Sec. III but can also be read independently to gain a first insight into the features observed for chalcopyrite alloys. Conclusions are given in Sec. V summarizing similarities and differences of the various materials presented and highlighting the strong influence of the atomic-scale structure of semiconductor alloys on important material properties.

II. X-RAY ABSORPTION SPECTROSCOPY

X-ray absorption spectroscopy is a powerful tool for structural analysis applicable to a vast range of materials and widely used in physics, chemistry, material science, geology, biology, and environmental science.[48–51] It is based on the measurement of the material specific and energy-dependent X-ray absorption coefficient, $\mu(E)$, where E denotes the X-ray energy. As shown in Fig. 3, $\mu(E)$ decreases with increasing photon energy until the binding energy of a core electron is reached. For X-ray energies larger than this binding energy, the photon can be absorbed thereby creating a free photoelectron and a core hole. The X-ray absorption coefficient therefore exhibits a sharp increase at the binding energy of the core electron and then continues to decrease with increasing photon energy. The binding energy of the core electron and hence the position of the absorption edge depend on the type of the absorbing atom and are thus element-specific.

The photoelectron wave created during the absorption process propagates outwards and is scattered at the neighboring atoms. The final state is therefore a superposition of the

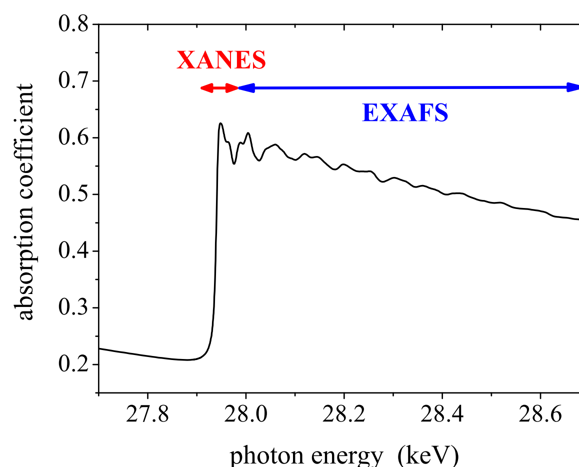

FIG. 3. X-ray absorption coefficient versus photon energy measured at the In K-edge (27.94 keV) of crystalline InP. The red and blue arrows indicate the region of the X-ray absorption near edge structure (XANES) and the extended X-ray absorption fine structure (EXAFS), respectively.

This article is copyrighted as indicated in the article. Reuse of AIP content is subject to the terms at: http://scitation.aip.org/termsconditions. Downloaded to IP: 131.169.38.71 On: Tue, 17 Nov 2015 09:25:17

outgoing and scattered photoelectron waves as shown schematically in Fig. 4. The interference pattern thus created depends on the number and type of neighboring atoms, on their distance to the absorber and on the photoelectron wavelength which is determined by the initial X-ray energy. For a given absorber environment, different X-ray energies will thus lead to constructive or destructive interference at the site of the absorbing atom which enhances or diminishes the probability for absorption, respectively. The resulting modulation of the X-ray absorption coefficient above the absorption edge is known as the X-ray absorption fine structure, $\chi(E)$, and can be easily seen in Fig. 3. Since the interference pattern depends on the geometric arrangement of the neighboring atoms, $\chi(E)$ contains information about the structural environment of the absorbing atom.

Two different regions of the fine structure are typically distinguished as indicated in Fig. 3. The X-ray absorption near edge structure (XANES) constitutes the edge itself and the region very close to it while the extended X-ray absorption fine structure (EXAFS) extends from approximately 30 eV above the edge up to 1000 eV or more above the edge. The XANES region is sensitive to chemical bonding and to the three-dimensional symmetry of the surrounding structure. It thus provides information about the valence state of the absorbing atom and the kind of first nearest neighbors and about the crystallinity and phase of the material. The EXAFS region mostly depends on the geometric arrangement of the atoms surrounding the absorber. It therefore provides information about coordination numbers, interatomic distances, and structural and thermal disorder.

The X-ray absorption fine structure is measured for a particular absorption edge and thus for a particular element in the sample. The structural information provided by EXAFS is therefore element-specific and describes the environment of a particular atomic species within the material.

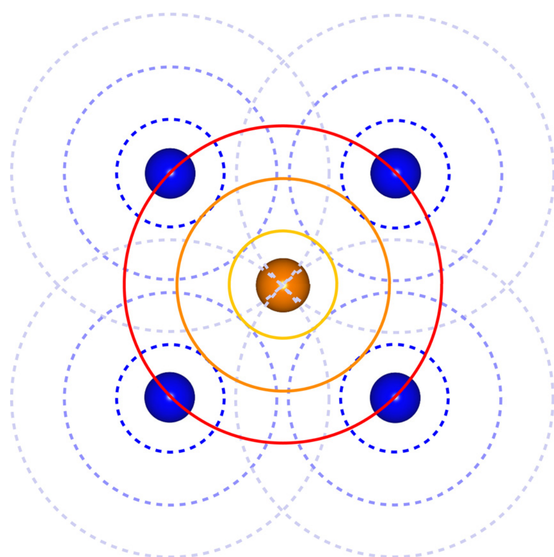

FIG. 4. Schematic of the central absorbing atom (orange) and its surrounding first nearest neighbors (blue). The outgoing photoelectron wave (solid orange lines) is reflected at the neighboring atoms (dashed blue lines) thus creating an interference pattern that depends on the photoelectron wavelength and on the geometric arrangement of the neighboring atoms.

Furthermore, the spatial range probed by EXAFS is usually of the order of six to ten angstroms due to the finite lifetime of the core hole and the finite mean free path of the photoelectron. This makes EXAFS a very local probe typically limited to the first three or four coordination shells. As a consequence, EXAFS does not require any long-range order and is equally applicable to crystalline, disordered, and even amorphous materials. The X-ray absorption process occurs on a time scale much shorter than that for atomic motion. The interference pattern shown schematically in Fig. 4 thus depends on the instantaneous configuration around the absorbing atom and EXAFS is sensitive to the correlated motion of neighboring atoms. The measured fine structure of the absorption coefficient as shown in Fig. 3 therefore represents the average over all atomic configurations present in the sample.

In particular, EXAFS measures the interatomic distance distribution of a given coordination shell as shown schematically in Fig. 5. Analysis of the EXAFS signal then yields (i) the mean value of the distance distribution which corresponds to the bond length in case of the first nearest neighbor shell; (ii) the variance or width of the distance distribution which is a measure for static disorder and relative thermal vibrations; and (iii) the potential asymmetry of the distance distribution which may be significant at high temperatures or for highly strained or disordered materials. This structural information together with the short-range and element-specific nature of EXAFS makes it an ideal tool for studying the atomic-scale structure of compound semiconductor alloys. A short introduction to the technique is given in Ref. 67, while detailed discussions of both theoretical and experimental aspects are provided in Refs. 48–50.

III. ZINCBLENDE MATERIALS

Most of the III-V semiconductors crystallize in the cubic zincblende structure shown in Fig. 2(c). Only the nitride compounds prefer the similar but hexagonal wurtzite structure (space group $P6_3mc$). Among the II-VI semiconductors, the zincblende structure is again most commonly

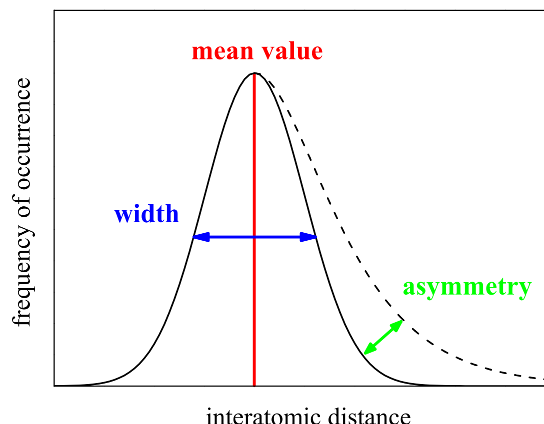

FIG. 5. Schematic of the interatomic distance distribution characterized by the mean value (red) corresponding to the bond length, the variance or standard deviation (blue) corresponding to the width of the distance distribution and a potential asymmetry (green) corresponding to an excess of either long or short distances.

This article is copyrighted as indicated in the article. Reuse of AIP content is subject to the terms at: http://scitation.aip.org/termsconditions. Downloaded to IP: 131.169.38.71 On: Tue, 17 Nov 2015 09:25:17

encountered although some compounds are found to crystallize in the wurtzite or rocksalt structure (space group F$m\bar{3}m$). However, different crystal structures can be stabilized for many materials depending on the growth conditions. This results in different physical properties even for one and the same compound. Table I lists some basic properties for a number of III-V and II-VI semiconductors with zincblende structure. The Phillips ionicity[68,69] varies between 0.25 and 0.42 for the III-V compounds, while it is found between 0.61 and 0.79 for the II-VI materials. The lattice constant ranges from 5.45 and 5.41 Å for GaP and ZnS, respectively, to 6.48 Å for InSb and CdTe. The bandgap energy is lowest for compounds consisting of high Z elements and highest for compounds made up of light elements. The values range from nearly zero to 1.43 and 3.73 eV for the direct III-V and II-VI semiconductors, respectively. For the indirect III-V semiconductors, the lowest bandgap energy varies between 1.62 and 2.48 eV. This brief comparison already demonstrates very clearly the wide range of properties spanned by this class of semiconductor materials.

Most III-V and II-VI semiconductors with a common element are completely miscible over the entire compositional range forming ternary alloys with the same crystal structure as the parent compounds. Prominent examples for lattice-matched systems include AlAs-GaAs and CdSe-HgSe where the difference in the lattice constants of the binary parent compounds is less than 0.2%. Many other systems, however, are lattice-mismatched with differences in the binary lattice constants of up to ~10%. Most of these alloys were found to obey Vegard's Law and the ternary lattice constant can be described to a very good approximation by

TABLE I. Phillips ionicity, f_i,[68,69] lattice constant, a, first nearest neighbor bond length, d, lowest direct and indirect bandgap energy, $E_g^{(d)}$ and $E_g^{(i)}$, respectively, and nature, n, of the lowest bandgap at 300 K for different III-V and II-VI binary compounds with zincblende structure.[26,70]

Material	f_i	a (Å)	d (Å)	$E_g^{(d)}$ (eV)	$E_g^{(i)}$ (eV)	n
AlP	0.307	5.464	2.366	3.91	2.48	i
AlAs	0.274	5.661	2.451	3.01	2.15	i
AlSb	0.250	6.136	2.657	2.27	1.62	i
GaP	0.327	5.451	2.360	2.76	2.26	i
GaAs	0.310	5.653	2.448	1.43	1.72	d
GaSb	0.261	6.096	2.640	0.72	0.76	d
InP	0.421	5.869	2.541	1.35	2.05	d
InAs	0.357	6.058	2.623	0.36	1.07	d
InSb	0.321	6.479	2.805	0.17	0.93	d
ZnS[a]	0.623	5.410	2.343	3.73	5.14	d
ZnSe	0.630	5.669	2.455	2.72	3.40	d
ZnTe	0.609	6.104	2.643	2.27	3.05	d
CdS[b]	0.685	5.825	2.522	2.46	5.24	d
CdSe[b]	0.699	6.077	2.631	1.68	4.37	d
CdTe	0.717	6.481	2.806	1.51	3.48	d
HgS[a]	0.790	5.851	2.534	−0.04		d
HgSe	0.680	6.084	2.634	−0.08		d
HgTe	0.650	6.460	2.797	−0.15		d

[a]Materials for which the zincblende structure is one of the preferred crystal structures.

[b]Materials typically crystallize in the wurtzite structure but can also be observed in the zincblende modification.

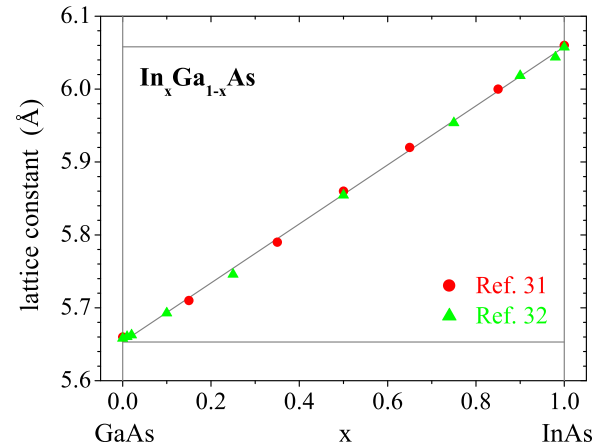

FIG. 6. Lattice constant versus composition x for $In_xGa_{1-x}As$. The data are taken from Refs. 31 (red circles) and 32 (green triangles). The thin gray lines represent the binary values and Vegard's Law.

Eq. (1).[26] As an example, Fig. 6 plots the lattice constant, $a(x)$, of $In_xGa_{1-x}As$ versus alloy composition x.[31,32] The values clearly increase linearly with increasing In content as expected from Vegard's Law and the VCA starting at the lattice constant of GaAs for $x = 0$ and reaching the lattice constant of InAs for $x = 1$. In contrast, the bandgap energy often exhibits a notably nonlinear change with alloy composition and can often be described satisfactorily by Eq. (2).[26,71] The lowest bandgap energy, $E_g(x)$, of $In_xGa_{1-x}As$ is shown as a function of alloy composition x in Fig. 7.[72–74] The values are well described by the quadratic behavior of Eq. (2) yielding an average bowing parameter b of 0.58 eV.[26] The bandgap bowing observed for other III-V and II-VI ternary alloys is discussed in detail in Sec. III E. Despite the nonlinearity, the bandgap energy changes continuously with changing alloy composition and can be purposefully tuned to any intermediate value by adjusting the In to Ga ratio. As shown in Fig. 1, this enables the precise tailoring of important material properties, most prominently the lattice constant and the bandgap energy, over a wide parameter range.

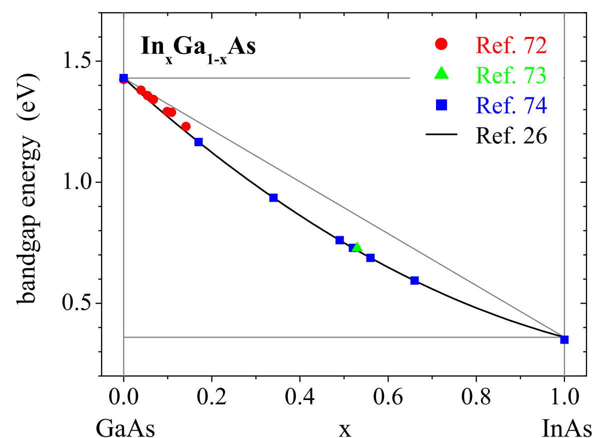

FIG. 7. Bandgap energy versus composition x for the direct semiconductor $In_xGa_{1-x}As$. The data are taken from Refs. 72 (red circles), 73 (green triangles), and 74 (blue squares). The black solid line corresponds to a quadratic dependence as given by Eq. (2) with an average bowing parameter b = 0.58 eV.[26] The thin gray lines represent the binary values and their weighted average.

This article is copyrighted as indicated in the article. Reuse of AIP content is subject to the terms at: http://scitation.aip.org/termsconditions. Downloaded to IP: 131.169.38.71 On: Tue, 17 Nov 2015 09:25:17

A. Atomic-scale structure

1. First nearest neighbor shell

The first EXAFS study of the atomic-scale structure of semiconductor alloys was the pioneering work on $In_xGa_{1-x}As$.[32,75] This cation-mixed alloy crystallizes in the zincblende structure and the lattice constant closely follows Vegard's Law (see Fig. 6). As shown schematically in Fig. 2(d), one sublattice is occupied by the As anions while the other sublattice is populated randomly by In and Ga cations. Each cation is bonded to four As anions, whereas each anion is surrounded by a mixed first nearest neighbor shell consisting of both In and Ga atoms. The system is thus characterized by two different bonds, namely, In-As and Ga-As. Based on Vegard's Law and the VCA, the corresponding bond lengths should be identical and should change linearly with composition x. Using EXAFS, the *individual* element-specific bond length have been measured for the first time thus assessing the validity of the VCA. Figure 8 plots the In-As and Ga-As bond lengths as a function of the composition x. The two bond lengths are very different from each other and remain much closer to the values of the binary parent compounds than to the ones predicted by the VCA. They do exhibit a linear increase with increasing In content; however, the change amounts to only 20% of the difference between the two binary bond lengths. As a consequence, there is a striking deviation of the local atomic arrangements from the average long-range crystallographic structure. The weighted average of the In-As and Ga-As bond lengths, however, agrees well with the prediction of the VCA as expected from diffraction studies which measure the *average* III-As bond length.

Similar EXAFS studies have subsequently been performed for a large number of III-V and II-VI ternary alloys with zincblende structure including the cation-mixed systems $In_xGa_{1-x}P$,[76–78] $In_xGa_{1-x}Sb$,[76,77,79] $Cd_xZn_{1-x}Se$,[80] $Cd_xZn_{1-x}Te$,[81–85] $Hg_xZn_{1-x}Te$,[86] and $Hg_xCd_{1-x}Te$[83,84,87,88] and the anion-mixed systems $GaAs_xP_{1-x}$,[76,77,89,90] $InSb_xP_{1-x}$,[91] $ZnTe_xSe_{1-x}$,[76,77,92] $CdTe_xSe_{1-x}$,[93] and $HgTe_xSe_{1-x}$.[83,84] As an example for an anion-mixed system, Fig. 9 plots the Ga-As and Ga-P bond lengths of $GaAs_xP_{1-x}$ versus composition x.[90] Here the cation sublattice is occupied solely by Ga atoms whereas the anion sublattice is populated randomly by As and P atoms thus creating the two different first nearest neighbor pairs. Similar to $In_xGa_{1-x}As$, the two bond lengths are very different from each other. They exhibit a linear increase with increasing As content; however, the change amounts again to only ~20% of the difference between the two binary bond lengths. A very similar behavior was observed for all other zincblende alloys studied. In each case, the bond length distribution is bimodal and the values are closer to those of the binary parent compounds than to the ones predicted by the VCA. The latter is thus an inadequate description for the atomic-scale structure of semiconductor alloys. Furthermore, most studies find a small linear change in the element-specific bond lengths with changing composition x. Only in case of $Cd_xZn_{1-x}Te$, a slightly nonlinear behavior is reported, although the nonlinearity is of the same order as the uncertainty and scatter of the data.[85] Numerous EXAFS studies were also performed on II-VI semiconductors with Mn substitution on the cation sublattice including $Zn_xMn_{1-x}S$,[94–97] $Zn_xMn_{1-x}Se$,[87,98,99] $Zn_xMn_{1-x}Te$,[100] $Cd_xMn_{1-x}Te$,[84,101,102] and $Hg_xMn_{1-x}Te$.[87,88] All works report a bimodal bond length distribution with values closer to those of the binary parent compounds than to the ones predicted by the VCA.

The bimodal bond length distribution for ternary zincblende alloys was also confirmed with other experimental techniques. Qualitatively, the difference between the In-V and Ga-V bond length was referred from cross-section scanning tunneling microscopy studies for $In_xGa_{1-x}P$[103] and $In_xGa_{1-x}As$.[104] The element-specific bond lengths further have a strong influence on the phonon modes observed with Raman spectroscopy, particularly on the impurity modes of the dilute limit.[105–112] It has been pointed out, however, that a full quantitative understanding of the relation between the local atomic arrangements and the various transverse and longitudinal optical modes is not trivial.[109,111,112] An independent determination of structural and vibrational properties of semiconductor alloys such as the EXAFS studies

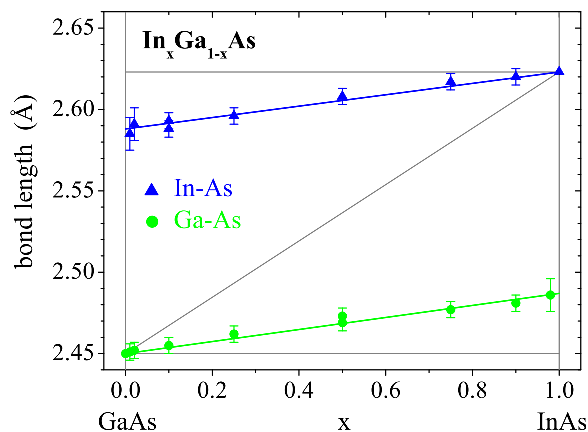

FIG. 8. Element-specific In-As (blue triangles) and Ga-As (green circles) bond lengths as a function of composition x for $In_xGa_{1-x}As$.[32,75] The solid lines show the best linear fits to the experimental data while the thin gray lines represent the binary values and the ones predicted by the VCA.

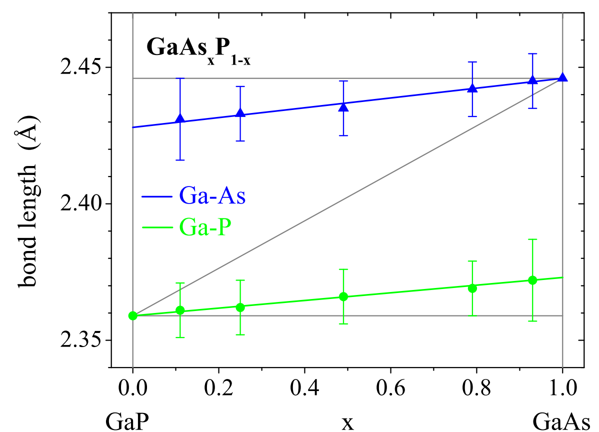

FIG. 9. Element-specific Ga-As (blue triangles) and Ga-P (green circles) bond lengths as a function of composition x for $GaAs_xP_{1-x}$.[90] The solid lines show the best linear fits to the experimental data while the thin gray lines represent the binary values and the ones predicted by the VCA.

This article is copyrighted as indicated in the article. Reuse of AIP content is subject to the terms at: http://scitation.aip.org/termsconditions. Downloaded to IP: 131.169.38.71 On: Tue, 17 Nov 2015 09:25:17

shown above can thus in fact advance the understanding and interpretation of complex Raman spectra. In contrast, the element-specific bond lengths of $In_xGa_{1-x}As$ were determined quantitatively over the whole compositional range by analyzing the high-resolution pair distribution functions obtained from X-ray diffraction measurements.[113–115] The results are in excellent agreement with those obtained from EXAFS measurements[32,75] and confirm the characteristic behavior of the element-specific bond lengths discussed above.

Slightly different results are obtained for strained epitaxial thin films where the lattice constant of the underlying substrate constrains the atomic-scale structure of the alloy.[116–126] If the lattice constant of the substrate is smaller than that of the ternary thin film, the bond lengths are reduced compared to the values found in bulk alloys. Similarly, substrates with larger lattice constants result in an increase of the bond length values. Figure 10 plots the In-As and Ga-As bond lengths as a function of the composition x for $In_xGa_{1-x}As$ thin films grown epitaxially on InP substrates.[122] For $x \sim 0.5$, the system is lattice matched and the bond lengths are identical to those obtained for bulk $In_xGa_{1-x}As$.[32,75] For decreasing x, the lattice constant of the alloy decreases and both the In-As and Ga-As distances increase due to the larger lattice constant of the underlying InP substrate. In contrast, for $x > 0.5$, the lattice constant of the alloy is larger than that of the InP substrate and the In-As and Ga-As bond lengths are reduced. This behavior can be explained by the tensile or compressive strain arising from the lattice mismatch between the substrate and the epitaxially grown thin film. For films grown beyond the critical thickness of some nanometers, the difference between the bond lengths of the strained layer and the bulk alloy decreases with increasing layer thickness and vanishes completely for films with a thickness of some tens of nanometers.[116,117] In all cases, however, the element-specific bond lengths of the ternary alloy remain much closer to the binary values than to the ones predicted by the VCA.

This characteristic behavior is not limited to ternary alloys with zincblende structure. The nitride alloys $In_xGa_{1-x}N$ and $Ga_xAl_{1-x}N$ crystallize in the wurtzite structure. EXAFS measurements have revealed that the In-N and Ga-N first nearest neighbor distances of $In_xGa_{1-x}N$ and the Ga-N first nearest neighbor distance of $Ga_xAl_{1-x}N$ are again closer to their respective binary values than to the ones predicted by the VCA.[127–130] Furthermore, they typically show a small change with changing composition similar to their zincblende counterparts. However, clustering, phase segregation, strain, and atomic ordering due to the specific preparation conditions may significantly influence the structural parameters of these nitride alloys.[130,131] Two distinctly different element-specific bond lengths were also observed for the I-VII ionic alloys $Rb_xK_{1-x}Br$ and RbI_xBr_{1-x} which crystallize in the rocksalt structure.[132,133] The bimodal bond length distribution is thus a characteristic feature of III-V, II-VI, and I-VII ternary alloys independent of their crystal structure.

To assess the change in the element-specific bond lengths with respect to the change in lattice constants for different alloy systems, the dimensionless relaxation parameter, ϵ, was introduced. It is defined for the dilute limit as the difference between the impurity bond length (d_A^{dil} or d_B^{dil}) and the host bond length (d_A^{bin} or d_B^{bin}) divided by the difference between the two binary values

$$\begin{aligned} \epsilon_A &= (d_A^{dil} - d_B^{bin})/(d_A^{bin} - d_B^{bin}), \\ \epsilon_B &= (d_A^{bin} - d_B^{dil})/(d_A^{bin} - d_B^{bin}). \end{aligned} \quad (5)$$

Figure 11 shows a schematic representation of the typical bimodal bond length distribution and the corresponding properties. An ϵ value equal to zero (no relaxation) corresponds

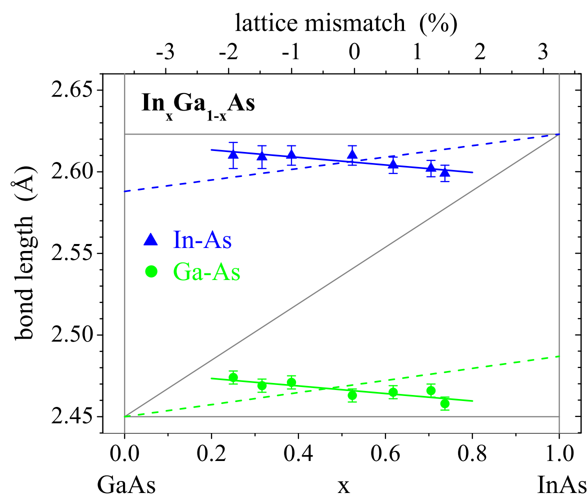

FIG. 10. Element-specific In-As (blue triangles) and Ga-As (green circles) bond lengths as a function of composition x for strained $In_xGa_{1-x}As$ thin films grown epitaxially on InP substrates.[122] The solid lines show the best linear fits to the experimental data while the dashed lines represent the fits to the bond lengths of unstrained $In_xGa_{1-x}As$ shown in Fig. 8. The thin gray lines represent the binary values and the ones predicted by the VCA for unstrained bulk material. The top axis shows the lattice mismatch between the $In_xGa_{1-x}As$ alloy and the InP substrate based on Vegard's Law.

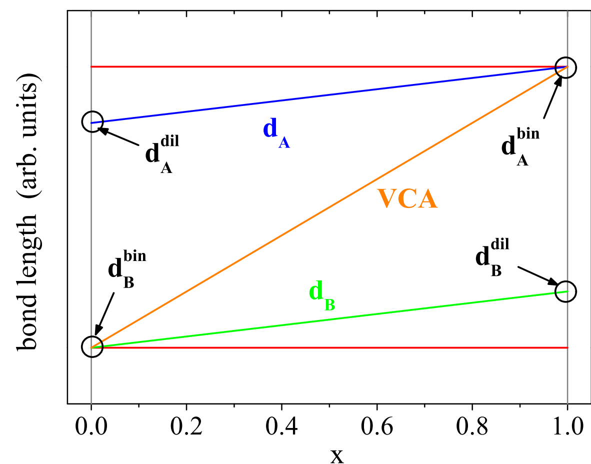

FIG. 11. Schematic of the element-specific bond lengths, d_A (blue) and d_B (green), as a function of composition x for cation-mixed alloys $A_xB_{1-x}C$ or anion-mixed alloys CA_xB_{1-x}. The binary values, d_A^{bin} and d_B^{bin}, and the values for the dilute limit, d_A^{dil} and d_B^{dil}, are also indicated. The orange line corresponds to the VCA prediction and represents the extreme case of zero relaxation where the lattice mismatch is accommodated solely by bond stretching. In contrast, the red lines correspond to the binary values and represent the extreme case of full relaxation where the lattice mismatch is accommodated solely by bond bending.

This article is copyrighted as indicated in the article. Reuse of AIP content is subject to the terms at: http://scitation.aip.org/termsconditions. Downloaded to IP: 131.169.38.71 On: Tue, 17 Nov 2015 09:25:17

to an impurity bond length that is identical to the host bond length. In this case, the lattice is completely rigid, forcing the impurity bond length to adopt the value of the host lattice in accordance with the VCA.[46] The lattice mismatch is therefore accommodated solely by bond stretching. In contrast, an ϵ value equal to one (full relaxation) corresponds to an impurity bond length equal to the value of its own binary compound. In this case, the lattice is completely floppy, allowing all bond lengths to retain their binary values in accordance with the model proposed by Pauling and Huggins.[47] The lattice mismatch is therefore accommodated solely by bond bending. Table II lists the experimentally determined ϵ values for III-V and II-VI ternary alloys with zincblende structure. As can be seen, the values are mostly between 0.75 and 0.85. While some works report a slightly smaller ϵ for the longer A bond compared to the shorter B bond, the differences are typically within the experimental uncertainty of ± 0.05. For comparison, ϵ values of approximately 0.75 and 0.60 to 0.65 were found for the nitride alloys $Ga_xAl_{1-x}N$ and $In_xGa_{1-x}N$, respectively, that crystallize in the wurtzite structure.[127,128,130] For the ionic alloy $Rb_xK_{1-x}Br$ with the rocksalt structure, ϵ amounts to 0.55 while ϵ values of 0.65 and 0.80 are reported for RbI_xBr_{1-x}.[132,133] These relaxation parameters are somewhat smaller than those of the zincblende alloys indicating that the nature of the bonding and the local coordination may affect the degree of bond length relaxation. Nevertheless, all ϵ values clearly show that bond bending is strongly favored over bond stretching resulting in the characteristic bimodal bond length distribution.

TABLE II. Relaxation parameter, ϵ, for the two different bonds of III-V and II-VI ternary alloys with zincblende structure. The uncertainty of the values is typically around ± 0.05.

Cation-mixed alloys			
$A_xB_{1-x}C$	ϵ_A	ϵ_B	References
$In_xGa_{1-x}P$	0.76	0.80	76
	0.76	0.79	77
	0.80	0.80	78
$In_xGa_{1-x}As$	0.80	0.79	32
	0.80	0.77	76 and 77
$In_xGa_{1-x}Sb$	0.78	0.79	76 and 77
	0.79	0.87	79
$Cd_xZn_{1-x}Te$	0.70	0.76	81–84
	0.86	0.92	85
$Hg_xZn_{1-x}Te$	0.95	0.95	86
Anion-mixed alloys			
CA_xB_{1-x}	ϵ_A	ϵ_B	References
$GaAs_xP_{1-x}$	0.60		89
	0.75	0.76	76 and 77
	0.79	0.84	90
$ZnTe_xSe_{1-x}$	0.78	0.80	76
	0.75	0.80	77
	0.79	0.80	92
$CdTe_xSe_{1-x}$		0.82	93
$HgTe_xSe_{1-x}$	0.96	0.74	83 and 84

The element-specific bond lengths represent the mean values of the corresponding first nearest neighbor distance distributions as discussed in Sec. II. Analysis of the EXAFS spectra further yields the widths of these distributions characterized by the standard deviation, σ, or the variance, σ^2. In the binary parent compounds, the width of the first nearest neighbor distance distribution is predominantly caused by the thermal motion of the atoms, whereas static contributions due to defects or strain can typically be neglected. Surprisingly, most studies report that the element-specific distance distributions of the ternary alloys show the same variation as those of the binary materials within experimental uncertainty.[32,75–78,80,86,89,90] As an example, Fig. 12 plots the variance of the In-P and Ga-P distance distribution of $In_xGa_{1-x}P$ versus composition x.[78] Clearly, no trend is observed for the σ^2 values with changing alloy composition. Similar conclusions were also drawn from high-resolution pair distribution functions obtained for $In_xGa_{1-x}As$ by X-ray diffraction measurements.[113–115] The only exception reported so far is $ZnTe_xSe_{1-x}$ for which the variance of the Zn-Te distance was found to be independent of x, whereas the variance of the Zn-Se distance slightly increased with decreasing Se content.[92] Interestingly, a broadening of the distance distributions due to an increase in structural disorder in the alloy is thus not apparent for the first nearest neighbor bonds in most of the alloys studied.

2. Second nearest neighbor shell

In the zincblende structure, each atom has twelve second nearest neighbors all occupying the same sublattice as the central atom (see Figs. 2(c) and 2(d)). However, for $In_xGa_{1-x}As$, each pair of second nearest neighbor As anions is linked by one cation that can be either In or Ga. This leads to two different types of second nearest neighbor As pairs, namely, As-In-As and As-Ga-As. Similarly, the second nearest neighbor cations are always linked by one As anion but there are three possible cation combinations. Therefore, three different types of second nearest neighbor cation pairs can be distinguished, namely, In-As-In, In-As-Ga (Ga-As-In),

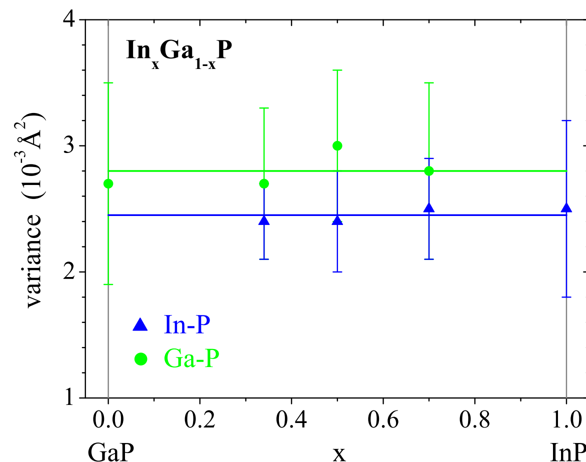

FIG. 12. Variance of the element-specific In-P (blue triangles) and Ga-P (green circles) first nearest neighbor distance distribution as a function of composition x for $In_xGa_{1-x}P$.[78] The solid lines represent the average values.

This article is copyrighted as indicated in the article. Reuse of AIP content is subject to the terms at: http://scitation.aip.org/termsconditions. Downloaded to IP: 131.169.38.71 On: Tue, 17 Nov 2015 09:25:17

and Ga-As-Ga. Figure 13 plots all second nearest neighbor distances for $In_xGa_{1-x}As$ versus composition x.[32] Regarding the anion sublattice, the scattering contribution stemming from the second nearest neighbor shell around the As atoms cannot be fit with a single peak. Instead, a bimodal distance distribution with two distinct second nearest neighbor distances is necessary to satisfactorily represent the experimental data. Based on their average values and relative weights, these two contributions can be assigned to As-In-As and As-Ga-As pairs. As can be seen from Fig. 13, the two distances remain close to their corresponding binary values and show only a small increase with increasing In content. In fact, the change amounts to only 15% of the difference between the two binary values. A bimodal second nearest neighbor distance distribution for the anion sublattice was also observed for other cation-mixed alloys including $Cd_xZn_{1-x}Te$,[81–85] $Zn_xMn_{1-x}Se$,[99] and $Zn_xMn_{1-x}Te$.[100]

For the anion-mixed alloy $GaAs_xP_{1-x}$, the cation sublattice is occupied solely by Ga atoms. However, the linking anion can be either As or P resulting in two different cation-cation second nearest neighbor pairs, namely, Ga-As-Ga and Ga-P-Ga. Similarly, the anion sublattice features three different second nearest neighbor pairs all linked by a Ga cation, namely, As-Ga-As, As-Ga-P (P-As-Ga), and P-Ga-P. Figure 14 plots all second nearest neighbor distances for $GaAs_xP_{1-x}$ as a function of composition x.[90] Similar to the case of $In_xGa_{1-x}As$, two distinct contributions are needed to represent the second nearest neighbor distance distribution around the Ga atoms corresponding to Ga-As-Ga and Ga-P-Ga pairs. The average values of these two contributions are again closer to their binary values

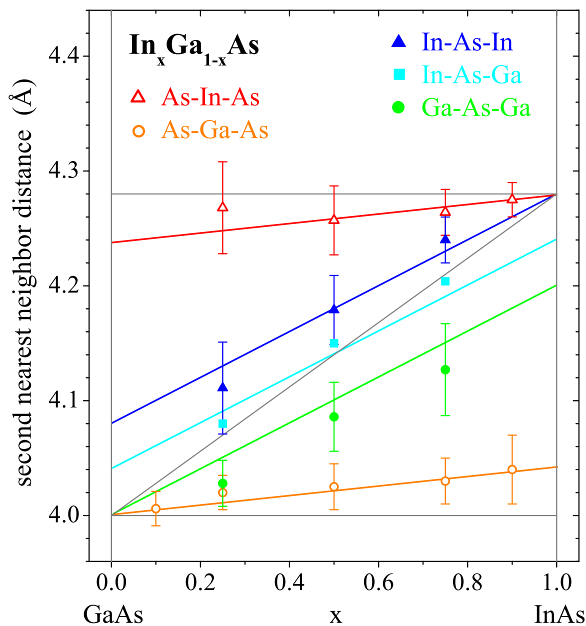

FIG. 13. Element-specific second nearest neighbor distances as a function of composition x for $In_xGa_{1-x}As$.[32] The anion sublattice features As-In-As (red open triangles) and As-Ga-As (orange open circles) pairs, while the cation sublattice is characterized by three different second nearest neighbor pairs, namely, In-As-In (blue full triangles), In-As-Ga or Ga-As-In (cyan full squares), and Ga-As-Ga (green full circles). The solid lines are a guide to the eye with one slope for the cation-cation pairs and a different slope for the anion-anion pairs. The thin gray lines represent the binary values and the ones predicted by the VCA.

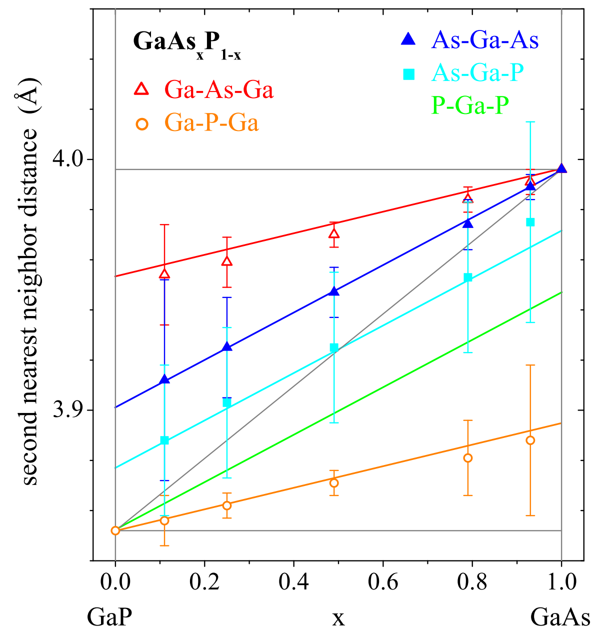

FIG. 14. Element-specific second nearest neighbor distances as a function of composition x for $GaAs_xP_{1-x}$.[90] The cation sublattice features Ga-As-Ga (red open triangles) and Ga-P-Ga (orange open circles) pairs, while the anion sublattice is characterized by three different second nearest neighbor pairs, namely, As-Ga-As (blue full triangles), As-Ga-P or P-Ga-As (cyan full squares), and P-Ga-P (green). The solid lines are a guide to the eye with one slope for the anion-anion pairs and a different slope for the cation-cation pairs. The thin gray lines represent the binary values and the ones predicted by the VCA.

than to the ones predicted by the VCA and exhibit only a moderate linear change with composition x that amounts to ~30% of the difference between the binary values. Two very different second nearest neighbor distances were also observed for the Zn sublattice in $ZnTe_xSe_{1-x}$.[77,92] Thus, the *common* sublattice in both cation- and anion-mixed alloys features a bimodal second nearest neighbor distance distribution with values that remain much closer to the second nearest neighbor distances of the binary parent compounds than to the ones predicted by the VCA.

Regarding the mixed sublattice, the second nearest neighbor distance distributions around the In and Ga cations in $In_xGa_{1-x}As$ are again best fit with two separate distances each corresponding to In and Ga second nearest neighbors. The three resulting cation-cation distances In-As-In, In-As-Ga (Ga-As-In) and Ga-As-Ga are, however, much closer to each other and to the ones predicted by the VCA than the two As-In-As and As-Ga-As distances as shown in Fig. 13. Nevertheless, they consistently follow the relation In-As-In > In-As-Ga > Ga-As-Ga. A similar behavior of the three different cation-cation distances was also observed for $In_xGa_{1-x}P$,[78] $Cd_xZn_{1-x}Te$,[85] and $Zn_xMn_{1-x}Se$.[99] For the anion-mixed alloy $GaAs_xP_{1-x}$, the As-Ga-As and As-Ga-P distances are also close to the ones predicted by the VCA and follow the relation As-Ga-As > As-Ga-P as can be seen from Fig. 14. A similar behavior was found for the Te-Zn-Se and Se-Zn-Se distances in $ZnTe_xSe_{1-x}$.[92] Thus, the *mixed* sublattice in both cation- and anion-mixed alloys features three distinct second nearest neighbor distances. However, the values are much closer to each other and to the ones

This article is copyrighted as indicated in the article. Reuse of AIP content is subject to the terms at: http://scitation.aip.org/termsconditions. Downloaded to IP: 131.169.38.71 On: Tue, 17 Nov 2015 09:25:17

predicted by the VCA than to the second nearest neighbor distances of the binary parent compounds.

The situation is somewhat less clear for the nitride alloys with wurtzite structure. For cation-mixed $Ga_xAl_{1-x}N$, the Ga-N-Ga second nearest neighbor distance was found to be close to the values predicted by the VCA.[127,128] In contrast, the Ga-N-Al distance was reported either to be close to the values predicted by the VCA[127] or to be independent of composition and close to the second nearest neighbor distance of AlN.[128] For $In_xGa_{1-x}N$, the cation-cation second nearest neighbor distances of the mixed sublattice were again found to be close to the ones predicted by the VCA in agreement with the behavior discussed above.[129,130] However, differences between the In-N-Ga and Ga-N-In distances for low In contents point to differences in the second nearest neighbor environment for the two cation species and were taken as an indication for phase segregation in these samples.[130] As already mentioned above, clustering, phase segregation, or atomic ordering may significantly influence the atomic-scale structural parameters of these semiconductor alloys.[130,131]

In contrast to the first nearest neighbor shell, the second nearest neighbor distance distributions are significantly broadened in the ternary alloys compared to the binary parent compounds.[32,78,92,134] Figure 15 plots the variance of the two anion-anion pairs in $In_xGa_{1-x}As$ and of two cation-cation pairs in $In_xGa_{1-x}P$ versus composition x.[134] It is readily apparent that the width of both the As-In-As and the As-Ga-As distance distribution is significantly higher in $In_xGa_{1-x}As$ than in InAs or GaAs, respectively. A similar behavior was also observed in high-resolution pair distribution functions obtained from X-ray diffraction measurements.[113–115] This increase is caused by the fact that each As atom has four In or Ga first nearest neighbors all of which affect its position and thus the second nearest neighbor As-As distances. Similarly, the widths of the cation-cation distributions are significantly higher in $In_xGa_{1-x}P$ than in InP or GaP due to the different atomic arrangements present in the ternary alloy. Typically, the variation of second nearest neighbor distances is larger for the common sublattice than for the mixed sublattice.[92,113,114]

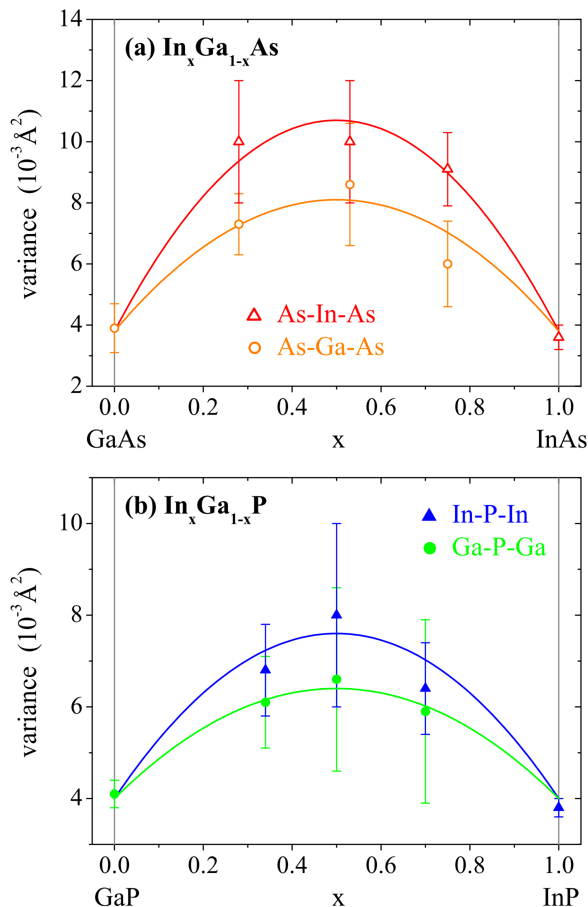

FIG. 15. Variance of the distance distribution for the second nearest neighbor pairs as a function of composition x for (a) the anion-anion pairs As-In-As (red open triangles) and Ga-As-Ga (orange open circles) in $In_xGa_{1-x}As$ and (b) the cation-cation pairs In-P-In (blue full triangle) and Ga-P-Ga (green full circles) in $In_xGa_{1-x}P$.[134] The solid lines are a guide to the eye.

While there exists an increased variation in the second nearest neighbor distances of III-V and II-VI ternary alloys, the mixed sublattice already closely resembles the VCA. In contrast, the common sublattice is severely distorted with two distinct second nearest neighbor distances close to the corresponding binary values. The atoms occupying the common sublattice are thus significantly more displaced from the ideal lattice sites than the atoms occupying the mixed sublattice.

The situation is more complex and again somewhat different when studying strained epitaxial thin films.[119,126,135] Here, the alloy unit cell is tetragonally distorted with different lattice constants parallel to the layer (*in plane*) and perpendicular to the layer, i.e., parallel to the sample normal (*out of plane*). As a consequence, the second nearest neighbor distance distributions split depending on the position of the atoms. Second nearest neighbors that are located in a plane parallel to the layer have a different distance than second nearest neighbors that are located in a plane perpendicular to the layer. Such differences can be probed by polarization-dependent EXAFS measurements where the angle between the X-ray polarization and the sample normal is varied.[51] Figure 16 plots the *in plane* and *out of plane* second nearest neighbor distances for strained $In_xGa_{1-x}As$ layers grown epitaxially on [001] InP substrates.[126,135] Similar to bulk $In_xGa_{1-x}As$, the second nearest neighbor distances for the various anion-anion and cation-cation pairs clearly differ from each other. Furthermore, the *out of plane* values, i.e., the second nearest neighbor distances perpendicular to the layer, increase with increasing In content and agree quite well with the bulk values. In contrast, the *in plane* values, i.e., the second nearest neighbor distances parallel to the layer, clearly decrease with increasing In content and differ significantly from the bulk values. Their behavior resembles that observed for the first nearest neighbor distances in strained epitaxial layers shown in Fig. 10. (Note that the first nearest neighbor distances do not split because all bonds have the same orientation with respect to the layer.) The *in plane* second nearest neighbor distances are thus increased or decreased compared to the bulk values depending on the lattice mismatch between the alloy film and the substrate. This clearly shows how anisotropic tensile or compressive strain can significantly modify the atomic-scale

This article is copyrighted as indicated in the article. Reuse of AIP content is subject to the terms at: http://scitation.aip.org/termsconditions. Downloaded to IP: 131.169.38.71 On: Tue, 17 Nov 2015 09:25:17

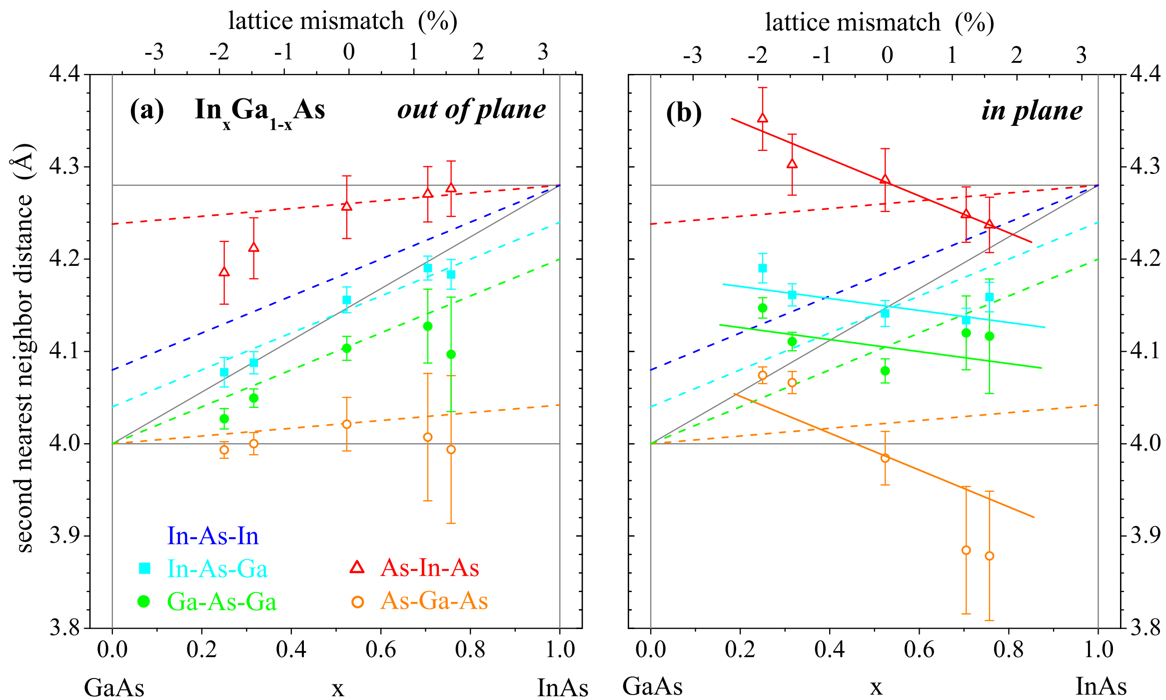

FIG. 16. Element-specific second nearest neighbor distances either (a) *out of plane* or (b) *in plane* as a function of composition x for strained $In_xGa_{1-x}As$ thin films grown epitaxially on InP substrates. The values were calculated from those given in Table II of Ref. 135 using their Eq. (4). They were further offset by -0.045 Å to match the bulk $In_xGa_{1-x}As$ values for $x = 0.53$ for which the layer is lattice-matched to the underlying InP substrate. The anion-anion pairs are As-In-As (red open triangles) and As-Ga-As (orange open circles), while the cation-cation pairs are In-As-In (blue), In-As-Ga or Ga-As-In (cyan full squares), and Ga-As-Ga (green full circles). The dashed lines represent the results for bulk $In_xGa_{1-x}As$ shown in Fig. 13, whereas the solid lines in panel (b) are a guide to the eye with one slope for the cation-cation pairs and a different slope for the anion-anion pairs. The thin gray lines represent the binary values and the ones predicted by the VCA for unstrained bulk material.

structure of semiconductor alloys grown as quantum dot or quantum well heterostructures.

3. Third nearest neighbor shell

Regarding the third nearest neighbor shell, four cation-anion pairs can be distinguished that differ with respect to the atoms of the mixed sublattice. For $In_xGa_{1-x}P$, for example, they are In-P-In-P, In-P-Ga-P, Ga-P-In-P, and Ga-P-Ga-P. However, the third nearest neighbor EXAFS signal is already significantly dampened and suffers from increasing overlap with other single or multiple scattering contributions. This usually inhibits the determination of separate In-P-In-P and In-P-Ga-P distances. Likewise, the Ga-P-In-P and Ga-P-Ga-P distances cannot be distinguished experimentally. Nevertheless, the *average* In-P or Ga-P third nearest neighbor distances have been determined for $In_xGa_{1-x}P$ as plotted in Fig. 17 versus composition x.[78] The values agree well with each other and are identical to the ones predicted by the VCA. The latter thus provides a very good description for interatomic distances beyond the second nearest neighbor shell. X-ray fluorescence holography of dilute $In_xGa_{1-x}Sb$

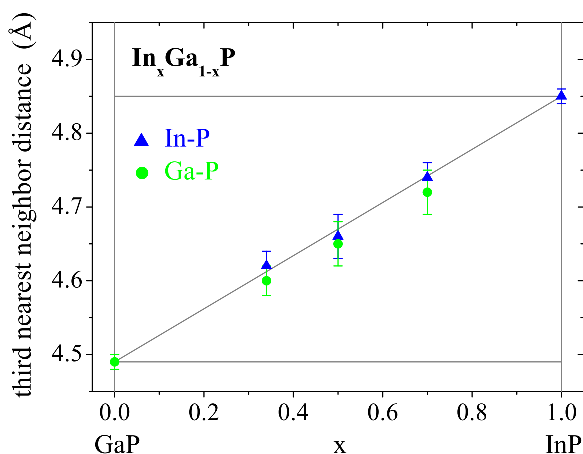

FIG. 17. Average In-P (blue triangles) and Ga-P (green circles) third nearest neighbor distances as a function of composition x for $In_xGa_{1-x}P$.[78] The thin gray lines represent the binary values and the ones predicted by the VCA.

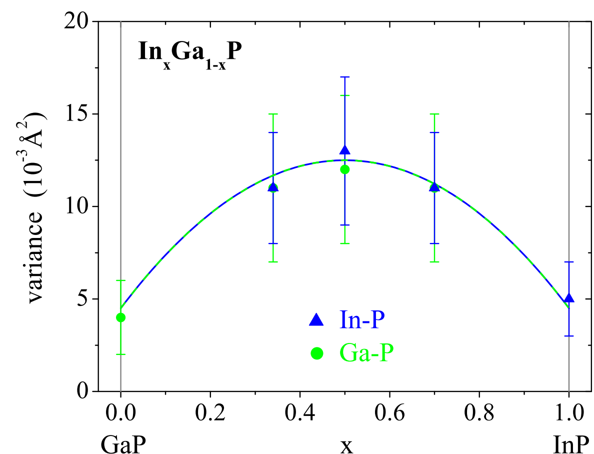

FIG. 18. Variance of the distance distribution versus composition x for third nearest neighbor In-P (blue triangles) and Ga-P (green circles) pairs in $In_xGa_{1-x}P$.[78] The solid lines are a guide to the eye.

This article is copyrighted as indicated in the article. Reuse of AIP content is subject to the terms at: http://scitation.aip.org/termsconditions. Downloaded to IP: 131.169.38.71 On: Tue, 17 Nov 2015 09:25:17

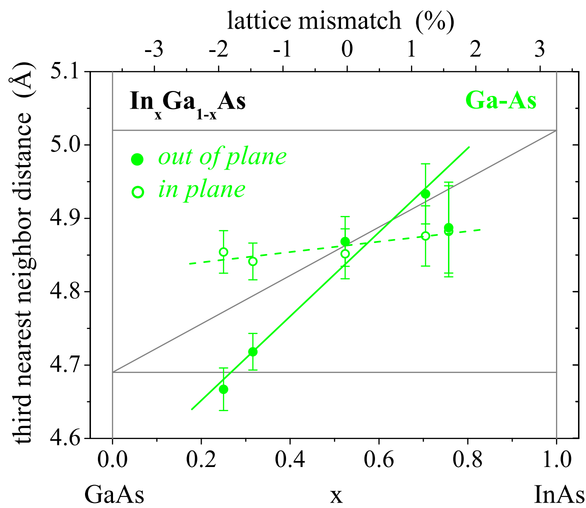

FIG. 19. Average Ga-As third nearest neighbor distances *out of plane* (full symbols) or *in plane* (open symbols) as a function of composition x for strained $In_xGa_{1-x}As$ thin films grown epitaxially on InP substrates. The values were calculated from those given in Table II of Ref. 135 using their Eq. (5). They were further offset by -0.045 Å to match the bulk (VCA) value for $x = 0.53$ for which the layer is lattice-matched to the underlying InP substrate. The dashed and solid lines are a guide to the eye. The thin gray lines represent the binary values and the ones predicted by the VCA for unstrained bulk material.

also showed that lattice distortions are limited to the first and second nearest neighbor shell and mostly vanish for the third shell and beyond.[136]

The distance distributions are, however, strongly broadened compared to those of the binary compounds due to the averaging over different atomic arrangements present in the ternary alloys. Figure 18 shows the variance of the In-P and Ga-P third nearest neighbor distance distribution as a function of composition x for $In_xGa_{1-x}P$.[78] A strong increase of the width of the distance distributions is clearly visible for the ternary alloys compared to InP or GaP.

In strained epitaxial layers, the third nearest neighbor distance distributions split depending on the orientation of the atomic pair with respect to the alloy thin film similar to what was observed for the second nearest neighbor shell. Figure 19 shows the *in plane* and *out of plane* Ga-As third nearest neighbor distances versus composition x for $In_xGa_{1-x}As$ layers grown epitaxially on [001] InP substrates.[126,135] The *out of plane* values show an increase with increasing In content similar to that predicted by the VCA or even higher. In contrast, the *in plane* values are nearly constant with composition. This clearly demonstrates once more the competing effects of alloying on the one hand and strain on the other hand, which determine the atomic-scale structural parameters of strained semiconductor alloys.

4. Bond angles

The tetrahedral bond angles can be evaluated from the first and second nearest neighbor distances. Figure 20 plots the As-*i*-As and *i*-As-*j* angles calculated for $In_xGa_{1-x}As$ using the data given in Ref. 32. Here, *i* and *j* denote either In or Ga. The In-As and Ga-As bond lengths and the two As-*i*-As second nearest neighbor distances remain close to their respective binary values. As a consequence, the As-*i*-As bond angle agrees well with the ideal zincblende value of 109.5° as shown in Fig. 20(a). In contrast, the three cation-cation second nearest neighbor distances are much closer to the ones predicted by the VCA than to the binary values. Specifically, the In-As-In distance is much smaller than that in InAs while the In-As first nearest neighbor distances are very similar. The In-As-In bond angle is therefore significantly smaller than the ideal tetrahedral value as can be seen in Fig. 20(b). Similarly, the Ga-As-Ga distance is much larger than that in GaAs leading to an increase of the Ga-As-Ga bond angle. The mixed In-As-Ga bond angle is found to be intermediate. The *i*-As-*j* bond angles thus deviate significantly from the ideal value and increase linearly with composition x in accordance with the increase of the cation-cation second nearest neighbor distances. Similar findings were observed for $In_xGa_{1-x}P$,[78] $Cd_xZn_{1-x}Te$ (using the data from Refs. 81–85), $Zn_xMn_{1-x}Se$,[99] $Zn_xMn_{1-x}Te$,[100] $GaAs_xP_{1-x}$ (using the data from Ref. 90), and $ZnTe_xSe_{1-x}$.[92] Analyzing all the angle information of the anion-mixed $ZnTe_xSe_{1-x}$ in detail, it was concluded that the tetrahedra which are formed by the Zn atoms are essentially undistorted but have a different size depending on the type of anion (Te

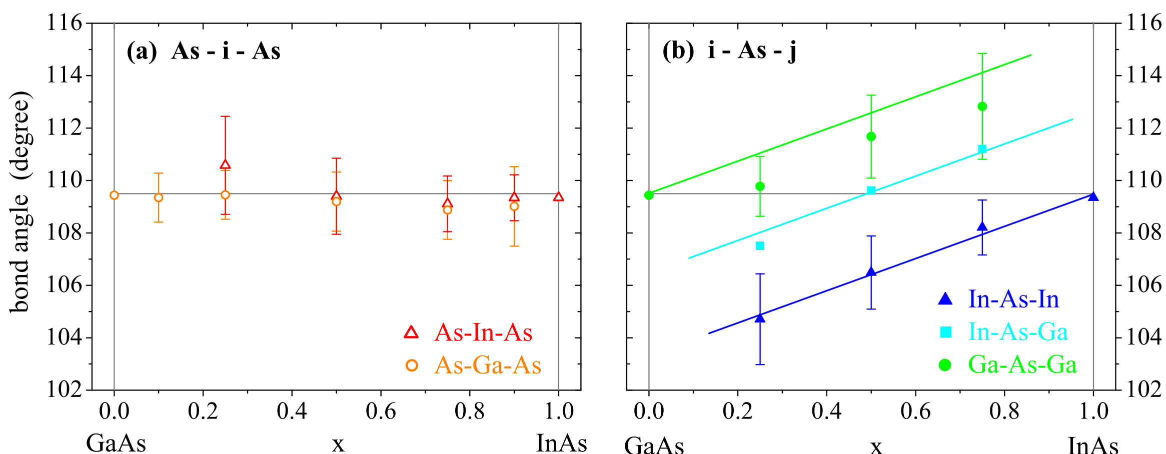

FIG. 20. (a) As-*i*-As and (b) *i*-As-*j* bond angles as a function of composition x calculated for $In_xGa_{1-x}As$ from the data reported in Ref. 32. The solid lines in panel (b) all have the same slope and are a guide to the eye. The ideal zincblende value of 109.5° is given as a thin gray line.

This article is copyrighted as indicated in the article. Reuse of AIP content is subject to the terms at: http://scitation.aip.org/termsconditions. Downloaded to IP: 131.169.38.71 On: Tue, 17 Nov 2015 09:25:17

or Se) around which they are centered.[92] These Zn tetrahedra are thus forced to tilt from their ideal zincblende orientation corresponding to a severe displacement of the Zn cations occupying the common sublattice as already discussed in Sec. III A 2.

B. Bond stretching and bond bending

1. Valence force field model

The relaxation parameters summarized in Table II clearly show that bond bending is favored over bond stretching. In fact, the bond angles change by up to 7% while the bond lengths typically change by only up to 1.5% over the compositional range. The lattice mismatch in the ternary alloys is thus accommodated mostly by bond angle relaxation and only to a small extent by bond length relaxation. The competing effects of bond stretching and bond bending can be described using the valence force field (VFF) approach.[137–142] In the notation introduced by Keating,[139] the distortion energy, U, is given by

$$U = \sum_i \left(\frac{3\alpha_i}{8\left(d_i^{bin}\right)^2} \right) \left[\mathbf{d}_i \cdot \mathbf{d}_i - \mathbf{d}_i^{bin} \cdot \mathbf{d}_i^{bin} \right]^2 + \sum_{ij} \left(\frac{3\beta_{ij}}{8 d_i^{bin} d_j^{bin}} \right) \left[\mathbf{d}_i \cdot \mathbf{d}_j - \mathbf{d}_i^{bin} \cdot \mathbf{d}_j^{bin} \right]^2. \quad (6)$$

The sum of the first term includes all bond vectors, $\mathbf{d}_i$, which are allowed to relax and represents the distortion energy due to bond stretching. The corresponding force constants, α_i, depend on the type of atoms that constitute the particular bond and $\mathbf{d}_i^{bin}$ denotes the undistorted bond vectors in the corresponding binary compounds. The second sum includes all bond angles (formed by the bond vectors $\mathbf{d}_i$ and $\mathbf{d}_j$) which are allowed to relax and represents the distortion energy due to bond bending with the corresponding force constants, β_{ij}. Note that the force constants α and β are different from the force constants k_r and k_θ often used together with further interaction constants in other VFF notations.[138] In fact, it can be shown that they relate to each other by[140]

$$k_r = 3\alpha + \frac{1}{2}\beta, \qquad k_\theta = \frac{2}{3}\beta. \quad (7)$$

The VFF models describe the distortion energy associated with bond length and bond angle variations. These variations are a response to strain which can be caused by alloying of lattice-mismatched parent compounds, by growth of thin films or nanostructures on lattice-mismatched substrates or by macroscopic strain or stress. As a consequence of the latter, the distortion energy can also be expressed in terms of the elastic constants thus providing a set of equations that relate these elastic constants to the bond stretching and bond bending force constants, α and β.[139–142] The latter can then be determined from experimentally measured elastic constants and bulk moduli. Different sets of parameters are reported for α and β in the literature depending on the experimental data used and on the treatment of the contribution of long-range Coulomb forces.[140–144] Tables III and IV list bond stretching and bond bending force constants, respectively, for a number of III-V and II-VI binary compounds. For most materials, the differences between the various values reported are in the order of 10% or less. Only for AlP, ZnS and ZnSe, differences exceeding 15% are observed.

Clear trends in the force constants are found when comparing the different materials with each other. From Tables I and III, it can be seen that the bond stretching force constant, α, decreases with increasing lattice constant, a, and thus increasing bond length, d.[141,145,146] The bond bending force

TABLE III. Bond stretching force constant, α, of the Keating VFF potential given in Eq. (6) obtained from experimentally determined elastic constants and bulk moduli for different III-V and II-VI binary compounds.

α (N/m)	Ref. 140	Ref. 143	Ref. 144	Ref. 141	Ref. 142
AlP		47.29	44.32		60.30
AlAs		43.05	40.85		41.20
AlSb	35.35		34.07	35.74	33.42
GaP	47.32		44.76	48.57	44.50
GaAs	41.19		39.24	43.34	41.25
GaSb	33.16		31.88	34.42	31.85
InP	43.04		40.36	44.29	39.52
InAs	35.18		33.20	37.18	33.17
InSb	29.61		28.56	30.44	29.61
ZnS	44.92		40.43	44.73	38.70
ZnSe	35.24		32.20	38.61	32.22
ZnTe	31.35		29.45	32.04	29.51
CdS					34.07
CdSe					31.72
CdTe	29.02		26.57	29.44	26.39
HgS		41.33			
HgSe		36.35		37.43	
HgTe		27.95	26.40	29.32	29.75

TABLE IV. Bond bending force constant, β, of the Keating VFF potential given in Eq. (6) obtained from experimentally determined elastic constants and bulk moduli for different III-V and II-VI binary compounds.

β (N/m)	Ref. 140	Ref. 143	Ref. 144	Ref. 141	Ref. 142
AlP		9.08	8.07		14.19
AlAs		9.86	8.72		8.94
AlSb	6.77		6.90	6.63	6.79
GaP	10.44		10.74	10.40	10.69
GaAs	8.95		9.16	8.88	9.25
GaSb	7.22		7.35	7.16	7.33
InP	6.24		6.54	6.26	6.60
InAs	5.50		5.75	5.47	5.75
InSb	4.77		4.89	4.73	5.07
ZnS	4.78		5.27	4.36	4.78
ZnSe	4.23		4.56	4.65	4.56
ZnTe	4.45		4.66	4.49	4.66
CdS					4.75
CdSe					4.37
CdTe	2.43		2.72	2.48	2.72
HgS		2.56			
HgSe		2.36		2.37	
HgTe		2.57	2.75	2.54	2.93

This article is copyrighted as indicated in the article. Reuse of AIP content is subject to the terms at: http://scitation.aip.org/termsconditions. Downloaded to IP: 131.169.38.71 On: Tue, 17 Nov 2015 09:25:17

constant, β, is significantly smaller than α as apparent from Tables III and IV. The ratio β/α follows the simple relation[140,141,146]

$$\beta/\alpha \propto 1 - f_i, \quad (8)$$

where f_i denotes the Phillips ionicity listed in Table I. Fitting the data available for III-V and II-VI compounds yields a β/α ratio of approximately 0.28 for $f_i = 0$ which is in good agreement with the values 0.285 and 0.294 reported for Si and Ge, respectively.[140,141] As the ionicity increases, β/α decreases approaching a value of zero for $f_i = 1$. Consequently, the difference between the bond stretching and bond bending force constants increases with increasing ionicity. Regarding the III-V semiconductors, α is approximately 4–5 times larger than β for the Al and Ga compounds, whereas the factor is already 6–7 for the In compounds. Regarding the II-VI semiconductors, the factor increases from about 8 for the Zn compounds to more than 10 for the Hg compounds. This means that bond stretching requires considerably more energy than bond bending. The lattice mismatch in semiconductor alloys is therefore accommodated mostly by a change in the bond angles and only to a small extent by a change in the bond lengths.

2. Thermal vibrations of atoms

Bond stretching and bond bending force constants do not only determine atomic-scale structural parameters, they also govern the vibrational behavior of the material. Vibrations of the atoms necessarily involve changes of the bond lengths and bond angles and the frequency of vibrational modes directly depends on the bond stretching and bond bending force constants. The latter can thus also be obtained from experimental phonon frequencies measured with Raman or infrared spectroscopy.[147–151] Information about the vibrational behavior of the atoms can also be deduced from temperature-dependent EXAFS measurements. Since the absorption process occurs on a time scale much shorter than that of atomic motion, EXAFS is sensitive to the instantaneous configuration surrounding the absorber and the X-ray absorption fine structure contains information about the correlated motion of neighboring atoms. Diffraction techniques typically measure the mean square displacement (MSD) of the atoms associated with a specific lattice site. The MSD of the absorber-backscatterer pair projected along the direction of the unit vector $\hat{\mathbf{e}}$ is then given by[152–154]

$$\mathrm{MSD} = \langle (\mathbf{u}_a \cdot \hat{\mathbf{e}})^2 \rangle + \langle (\mathbf{u}_b \cdot \hat{\mathbf{e}})^2 \rangle, \quad (9)$$

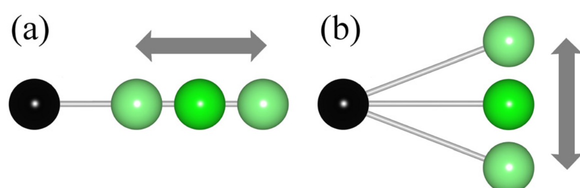

FIG. 21. Vibration of the absorber (black) and its first nearest neighbor (green) relative to each other (a) parallel to the bond direction and (b) perpendicular to the bond direction.

where $\mathbf{u}_a$ and $\mathbf{u}_b$ denote the instantaneous displacements of the absorbing and backscattering atom from its respective lattice site and the angular brackets represent a time or thermal average. In contrast, EXAFS measures vibrations of the absorber and its neighboring atoms relative to each other and is thus sensitive to the mean square *relative* displacement (MSRD). The projection of the MSRD of the absorber-backscatterer pair along the direction of the unit vector $\hat{\mathbf{e}}$ can thus be written as[152–154]

$$\mathrm{MSRD} = \langle [(\mathbf{u}_a - \mathbf{u}_b) \cdot \hat{\mathbf{e}}]^2 \rangle. \quad (10)$$

Regarding the first nearest neighbor, it is helpful to distinguish between relative vibrations parallel to the bond direction and perpendicular to the bond direction as shown schematically in Fig. 21. Relative vibrations *parallel* to the bond mostly involve bond stretching and the distance between the two atoms can be either shorter or longer than the equilibrium distance depending on the instantaneous position of the atoms. Averaging over all absorber-backscatterer pairs thus yields a first nearest neighbor distance distribution the width of which depends on the strength of the relative vibrations. It can be shown that the MSRD parallel to the bond direction equals the variance, σ^2, of the distance distribution measured by EXAFS[152,155–157]

$$\mathrm{MSRD}_{||} \simeq \sigma^2. \quad (11)$$

Relative vibrations *perpendicular* to the bond mostly involve bond bending and the instantaneous distance between the two atoms is always larger than the equilibrium distance (see Fig. 21). Averaging over all absorber-backscatterer pairs thus yields a mean first nearest neighbor distance that is larger than the equilibrium distance by a value that depends on the strength of the relative vibrations. It can be shown that the mean value, d_{EXAFS}, of the first nearest neighbor distance distribution measured by EXAFS is related to the crystallographic distance, d_C, between the two lattice sites and the MSRD projected onto a line perpendicular to the bond direction by[155–157]

$$d_{EXAFS} \simeq d_C + \frac{\mathrm{MSRD}_{\perp}}{d_C} \quad (12)$$

and

$$\mathrm{MSRD}_{\perp} \simeq d_C (d_{EXAFS} - d_C). \quad (13)$$

Analyzing the first nearest neighbor EXAFS signal in terms of the mean value and the variance of the distance distribution thus directly yields the $\mathrm{MSRD}_{||}$ while a comparison with crystallographic data obtained from diffraction measurements provides the $\mathrm{MSRD}_{\perp}$.

The strength of the relative vibrations at a given temperature is determined by the effective force constants for vibrations parallel or perpendicular to the bond direction. With increasing temperature, the atomic vibrations become stronger leading to an increase of $\mathrm{MSRD}_{||}$ and $\mathrm{MSRD}_{\perp}$. This temperature dependence can be described by a correlated Debye or Einstein model.[153,154,158] However, for non-Bravais systems such as compound semiconductors, the derivation of the correlated Debye model for the MSRD is not physically sound[158]

This article is copyrighted as indicated in the article. Reuse of AIP content is subject to the terms at: http://scitation.aip.org/termsconditions. Downloaded to IP: 131.169.38.71 On: Tue, 17 Nov 2015 09:25:17

and its application to experimental data yields unreasonable values for the Debye temperatures.[152,159] Therefore, only the correlated Einstein model should be used in these systems. The original Einstein model treats each atom as an independent oscillator. In contrast, the correlated Einstein model used for describing the temperature dependence of the $MSRD_{||}$ and $MSRD_{\perp}$ assumes each absorber-backscatterer pair to be an independent oscillator. The frequency of relative vibrations, $\omega_E = \sqrt{k/\mu}$, depends on the effective force constant, k, and the reduced mass, μ, of the atomic pair. The force constant represents an *effective* force constant because it also depends on the statistically averaged influence of the other neighboring atoms and should not be confused with the force constant of an isolated single bond.[160] The following relations have been obtained for the temperature dependence of $MSRD_{||}$ and $MSRD_{\perp}$ using either a lattice dynamical approach[154,158] or a quantum mechanical perturbation approach[161,162]

$$\begin{aligned} MSRD_{||} &= \frac{\hbar^2}{2\mu k_B}\frac{1}{\Theta_{E,||}}\coth\left(\frac{\Theta_{E,||}}{2T}\right) + \sigma^2_{static,||}, \\ MSRD_{\perp} &= \frac{\hbar^2}{2\mu k_B}\frac{1}{\Theta_{E,\perp}}\coth\left(\frac{\Theta_{E,\perp}}{2T}\right) + \sigma^2_{static,\perp}. \end{aligned} \tag{14}$$

Here, $\hbar$ and k_B denote Planck's constant divided by 2π and Boltzmann's constant, respectively, while T stands for the temperature of the material. The Einstein temperature Θ_E is related to the vibrational frequency, ω_E, by $\omega_E = \Theta_E k_B/\hbar$ and thus

$$k = \mu\frac{\Theta_E^2 k_B^2}{\hbar^2}. \tag{15}$$

The static contribution, σ^2_{static}, accounts for structural disorder potentially present in the sample as discussed in Sec. II.

As an example, Fig. 22 plots the $MSRD_{||} = \sigma^2$ values obtained for In-P first nearest neighbors in crystalline and amorphous InP as a function of temperature.[163] The amorphous phase was prepared by ion irradiation of crystalline InP.[164] This non-equilibrium process typically yields a preparation-specific amorphous structure that is characterized by a free energy greater than that of the intrinsic minimum-energy configuration of the amorphous phase.[165,166] Thermal annealing at temperatures well below that required for recrystallization leads to structural relaxation of the amorphous phase thus approaching the minimum-energy configuration.[164,166] The temperature dependence of the $MSRD_{||} = \sigma^2$ was determined for both the as-prepared and relaxed state of the amorphous phase as shown in Fig. 22.[163] The corresponding Einstein fits show good agreement with the data demonstrating that this simple model describes very well the temperature evolution of relative atomic vibrations in compound semiconductors. Obviously, the $MSRD_{||}$'s of all three samples show a very similar change with changing temperature yet their absolute values are quite different. This is reflected by the static contribution which equals zero for the crystalline phase but amounts to $\sigma^2_{static} = 3.1\pm0.2 \times 10^{-3}$ Å^2 and $2.6\pm0.2 \times 10^{-3}$ Å^2 for the as-prepared and relaxed amorphous phase, respectively. The amorphous material is thus characterized by strongly increased structural disorder compared to the crystalline phase as expected. The effective In-P bond stretching force constants $k_{||}$ are 107 ± 4, 95 ± 5, and 101 ± 5 N/m for crystalline, as-prepared amorphous, and relaxed amorphous phase, respectively. These values are very similar to each other reflecting the similar change in $MSRD_{||}$ with changing temperature. However, subtle differences can also be observed between the different samples which turn out to be significant given the typical uncertainty of about 5% or less for the determination of the effective bond stretching force constants.[163,167–169] The In-P bonds in the amorphous phase are thus slightly softer than in the crystalline material. Furthermore, relaxation of the as-prepared amorphous state yields a change in both static and dynamical properties towards the crystalline material as manifested by the reduction of structural disorder and by a slight strengthening of the In-P bonds.

A similar comparison between crystalline and amorphous material using temperature-dependent EXAFS measurements was also performed for Ge[159] and InSb.[170] Again, the amorphous phase is characterized by a strong increase of structural (static) disorder and a slight softening of the bonds when compared to the crystalline phase. The capability of

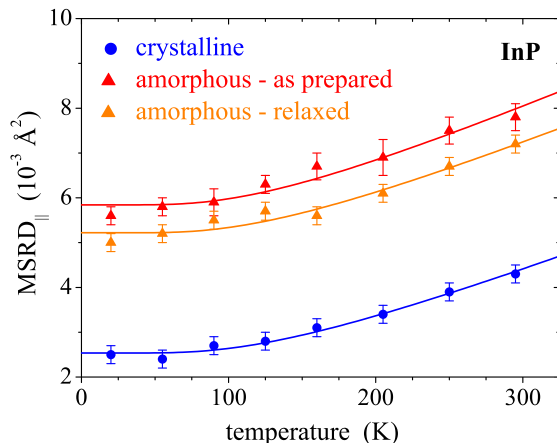

FIG. 22. First nearest neighbor $MSRD_{||}$ versus temperature for crystalline InP (blue circles) and amorphous InP in the as-prepared (red triangles) and relaxed (orange triangles) state.[163] The solid lines represent the best fits with the correlated Einstein model.

TABLE V. Effective force constants for relative vibrations of neighboring atoms parallel to the bond and perpendicular to the bond, $k_{||}$ and $k_{\perp}$, respectively, as determined from temperature-dependent EXAFS and X-ray diffraction measurements for binary III-V and II-VI compounds.

Material	Phase	$k_{\|\|}$ (N/m)	$k_{\perp}$ (N/m)	$k_{\|\|}/k_{\perp}$	References
GaAs	Crystalline	133 ± 15			172
		112 ± 3	30 ± 1	3.8	167
InP	Crystalline	107 ± 4	18 ± 4	5.9	163
	Amorphous				
	As-prepared	95 ± 5			163
	Relaxed	101 ± 5			163
InSb	Crystalline	94 ± 2			170
	Amorphous	82 ± 1			170
CdSe	Crystalline	76			173
CdTe	Crystalline	59 ± 1	13 ± 1	4.5	174 and 168

This article is copyrighted as indicated in the article. Reuse of AIP content is subject to the terms at: http://scitation.aip.org/termsconditions. Downloaded to IP: 131.169.38.71 On: Tue, 17 Nov 2015 09:25:17

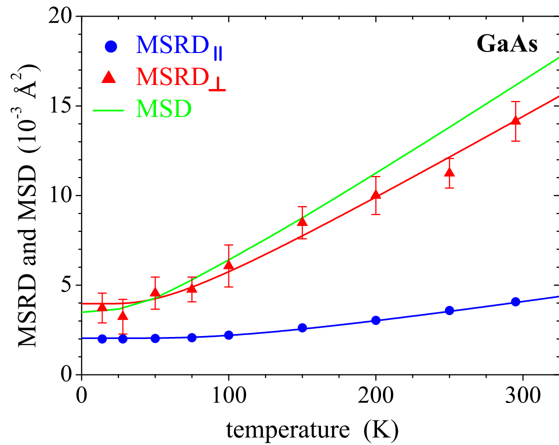

FIG. 23. First nearest neighbor $MSRD_{||}$ (blue circles) and $MSRD_{\perp}$ (red triangles) versus temperature for crystalline GaAs.[167] The blue and red solid lines represent the best fits with the correlated Einstein model. The uncorrelated MSD of the Ga-As pair is given as green solid line.[175,176]

EXAFS to determine vibrational properties was further demonstrated in a study comparing different Ge isotopes.[171] While the frequency is slightly different for ^{70}Ge and ^{76}Ge, the effective bond stretching force constant $k_{||}$ is the same for both materials showing that the differences originate from the different isotopic masses and not from variations in the strength of the bonds. Table V summarizes the $k_{||}$ values obtained from temperature-dependent EXAFS measurements of binary III-V and II-VI compounds.[163,167,168,170,172–174]

As discussed above, the combination of temperature-dependent EXAFS measurements and diffraction studies allows the determination of relative vibrations both parallel and perpendicular to the bond direction. Figure 23 plots the $MSRD_{||}$ and $MSRD_{\perp}$ for Ga-As first nearest neighbors in crystalline GaAs versus temperature.[167] The striking difference between these two types of relative vibrations is apparent immediately. While the $MSRD_{||}$ shows only a very small increase with increasing temperature, the $MSRD_{\perp}$ values are significantly higher and exhibit a pronounced increase with increasing temperature. Consequently, relative vibrations perpendicular to the bond are much stronger than relative vibrations parallel to the bond at any given temperature. It is very instructive to compare the MSRD's with the uncorrelated MSD of the Ga and As atoms given by the green solid line in Fig. 23.[175,176] Note that for cubic materials such as III-V and II-VI zincblende compounds the MSD is isotropic and atomic vibrations have the same strength in any direction.[176,177] However, the $MSRD_{||}$ is much smaller than the MSD, whereas the $MSRD_{\perp}$ is similar or only slightly lower. This means that *relative* vibrations parallel to the bond direction are strongly suppressed and the atoms tend to move in phase. In contrast, *relative* vibrations perpendicular to the bond direction are comparable to the uncorrelated motion of the atoms and no significant correlation effect occurs. This striking anisotropy in the relative vibrations of first nearest neighbor atoms is a direct consequence of the fact that bond stretching requires significantly more energy than bond bending as discussed in Sec. III B 1. The difference between the $MSRD_{||}$ and the MSD rapidly decreases for higher nearest neighbor shells since the absorber and backscattering atoms are no longer connected by a physical bond and a change in the interatomic distance can be achieved by a variation of bond lengths and bond angles.[152,159,160,163,167,172,174]

The anisotropic behavior of relative first nearest neighbor vibrations is also reflected by the corresponding force constants determined with the correlated Einstein models in Eq. (14). As can be seen in Fig. 23, the Einstein fits are again in excellent agreement with the experimental data and accurately represent the temperature evolution of the MSRDs. For GaAs, a $k_{||}$ value of 112 ± 3 N/m is obtained whereas $k_{\perp}$ amounts to only 30 ± 1 N/m. A similar vibrational anisotropy was also observed for InP,[163] CdTe,[168,174] and other tetrahedrally coordinated systems[160,168,174] and is believed to be the origin of the negative thermal expansion observed for these materials at very low temperatures.[160,174,178,179] The $k_{\perp}$ values obtained for GaAs, InP, and CdTe are listed in Table V together with $k_{||}$ and the ratio $k_{||}/k_{\perp}$. Similar to the bond stretching and bond bending force constants of the VFF model, $k_{||}$ and $k_{\perp}$ decrease with increasing ionicity of the bond.[160,167] The anisotropy tends to increase with increasing ionicity but also seems to depend on the mass ratio of the constituent elements.[160] Comparing the first part of the VFF potential in Eq. (6) with the oscillator potential used in the correlated Einstein model, $k_{||}$ should be roughly equal to 3α. The values of $k_{||}$ in Table V are indeed similar to the α values in Table III multiplied by a factor of 3, although small differences can also be observed. Similarly, the $k_{\perp}$ values in Table V are comparable to the β values in Table IV multiplied by a factor of 3. Effective bond stretching and bond bending force constants can thus also be determined from temperature-dependent EXAFS measurements.

C. Modeling of structural parameters

1. Models for the dilute limit

A number of different models have been proposed to describe the atomic-scale structure of ternary $A_xB_{1-x}C$ or CA_xB_{1-x} semiconductor alloys. Many of the early works sought to predict the first nearest neighbor impurity bond length in the dilute limit and thus the relaxation parameter, ϵ. In the dilute limit, a single impurity atom A is embedded into the host matrix BC as shown schematically in Fig. 24(a). The symmetry around this impurity atom strongly

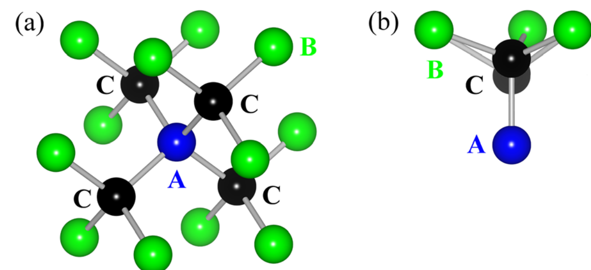

FIG. 24. Schematic for the dilute limit geometry of ternary zincblende alloys. (a) Impurity atom A (blue) embedded in a BC matrix (B—green and C—black). (b) Resulting displacement of the first nearest neighbor C atoms. Images created with VESTA.[29]

This article is copyrighted as indicated in the article. Reuse of AIP content is subject to the terms at: http://scitation.aip.org/termsconditions. Downloaded to IP: 131.169.38.71 On: Tue, 17 Nov 2015 09:25:17

TABLE VI. Relaxation parameter, ϵ, for the In-P and Ga-P bonds of $In_xGa_{1-x}P$ obtained with different models proposed to describe the atomic-scale structure of ternary semiconductor alloys. The experimental values determined from EXAFS measurements are also listed for comparison.

$In_xGa_{1-x}P$	ϵ_{In}	ϵ_{Ga}	Reference
Model 1	0.75	0.75	180
Model 2a	0.63	0.73	143
Model 2b	0.73	0.77	143
Model 3	0.70	0.80	144
Model 4	0.49	0.66	106
Model 5	0.78	0.73	102
With A1	0.78	0.73	78
With A2	0.73	0.77	78
Model 6a	0.72	0.72	142
Model 6b	0.66	0.77	142
Model 7	0.70	0.80	182
Model 8	0.72	0.80	183
Model 9	0.82	0.78	184
EXAFS	0.76 ± 0.05	0.80 ± 0.05	76
	0.76 ± 0.05	0.79 ± 0.05	77
	0.80 ± 0.04	0.80 ± 0.04	78

simplifies the calculation of the resulting A-C bond length. The most basic model (model 1) calculates the displacement of the first nearest neighbor C atoms surrounding the impurity A while keeping all other atoms fixed as shown schematically in Fig. 24(b).[180] A harmonic potential, i.e., a simple spring, is assumed for the first nearest neighbor interactions and a geometric approximation is made to correlate the A-C and B-C distances. Furthermore, a single bond stretching force constant is used for both types of bonds. Then the displacement corresponding to the minimum of the bond stretching energy of all four bonds is determined. The resulting relaxation is independent of the nature of the A, B, and C atoms and depends only on the crystal geometry. For the zincblende structure, $\epsilon = 0.75$ is obtained.

More elaborate models use the VFF potential in Eq. (6) (see Sec. III B) to describe the distortion energy associated with the presence of the impurity atom. The two different A-C and B-C bonds are characterized by individual force constants given by those of the binary parent compounds. This procedure implies that the binary force constants also apply to the ternary alloy system. Good results have been obtained with this methodology supporting the transferability of the force constants, although recent theoretical studies suggest that it may not be strictly valid.[181] In the framework of the VFF models, structural parameters such as the impurity bond length are again determined by minimizing the distortion energy associated with all bonds that are allowed to relax. Model 2a relaxes the first and second nearest neighbor shells surrounding the impurity atom.[143] Including the bond bending terms in the VFF potential and relaxing the second nearest neighbor shell change the relaxation parameter, ϵ, in opposite directions.[102,143] Including neither bond bending nor second nearest neighbor relaxation (model 2b) thus yields better results compared to experimental values than including only bond bending *or* second nearest neighbor relaxation.[143] Both models further apply two additional approximations during the calculation. They include only the harmonic terms of the VFF potential and they approximate the geometric relation between A-C and B-C distances as done in model 1 discussed above. The ϵ values obtained for $In_xGa_{1-x}P$ are listed in Table VI together with the experimental results.

Other models also consider chemical effects associated with the different types of atoms such as differences in the binding energy and chemically driven charge redistribution. In model 3, the distortion energy due to bond stretching and bond bending is again evaluated using the VFF potential while chemical effects are treated based on the bond orbital model.[144] The authors further calculate various VFF models that differ in whether or not bond bending terms are included in the potential and in how the relaxation of higher nearest neighbor shells is treated. For the case of In impurities in GaP, for example, the ϵ values obtained with the different VFF versions vary by up to $\Delta\epsilon \sim 0.30$ illustrating the huge influence such choices have on the calculated results. In contrast, model 4 does not apply the VFF approach but calculates the impurity bond lengths and the associated relaxation parameter using a semi-empirical tight-binding method based solely on the bond orbital model.[106] The ϵ values obtained with models 3 and 4 for $In_xGa_{1-x}P$ are listed in Table VI.

2. Models for the whole compositional range

A number of models have been developed that predict the A-C and B-C bond lengths not only in the dilute limit but also over the whole compositional range. To that end, the different configurations of A, B, and C atoms present in the alloy have to be considered. As shown schematically in Fig. 25, the atoms of the common sublattice can be surrounded by one of five possible first nearest neighbor environments characterized by the number, n, of A atoms varying between 0 and 4. The number of B first nearest neighbors is given by $4 - n$.

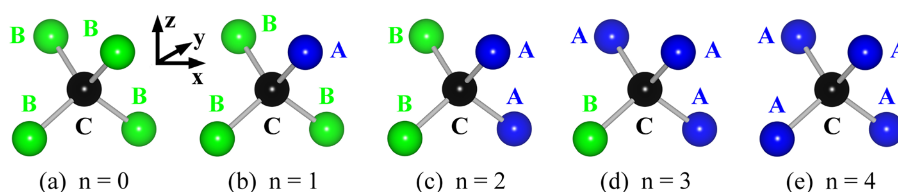

FIG. 25. Different first nearest neighbor configurations surrounding the central C atom (black) of the common sublattice in ternary III-V and II-VI semiconductor alloys with zincblende structure. The mixed sublattice, and thus the first nearest neighbor shell, is populated with A (blue) and B (green) atoms. The configurations are characterized by the number, n, of A atoms. Images created with VESTA.[29]

This article is copyrighted as indicated in the article. Reuse of AIP content is subject to the terms at: http://scitation.aip.org/termsconditions. Downloaded to IP: 131.169.38.71 On: Tue, 17 Nov 2015 09:25:17

In model 5,[83,84,101,102] the *individual* composition-dependent A-C and B-C distances are calculated for each configuration based on the following approach: (i) The lattice constant, $a(x)$, is derived as the weighted average of the two binary lattice constants according to Vegard's Law. (ii) The four first nearest neighbor atoms of the mixed sublattice are located on their ideal lattice sites, i.e., they occupy corners of a cube with the size $a(x)/2$. This assumption is justified by the results discussed in Sec. III A 2 where it was shown that the atoms of the mixed sublattice are much closer to the ideal lattice sites than the atoms of the common sublattice. (iii) The position of the central C atom and thus the first nearest neighbor distances are obtained by minimizing the sum of the bond stretching terms of the VFF potential. Neglecting the bond bending terms is reasonable as the bond bending force constants are significantly smaller than the bond stretching force constants as discussed in Sec. III B. Furthermore, including neither bond bending nor second nearest neighbor relaxation yields better results than including only one of the two effects.[102,143] The composition-dependent *average* A-C and B-C distances are then obtained as the weighted average of the individual first nearest neighbor distances of the five different configurations. To that end, the probability of finding a particular configuration at a certain composition x is needed. For a truly random alloy, this is given by the binomial Bernoulli distribution. Figure 26 plots the results obtained for $In_xGa_{1-x}As$ together with the best linear fit to the experimental data shown in Fig. 8.[102] The average In-As and Ga-As distances change linearly with composition x and are in very good agreement with the experimental data. Similar results were also obtained for $In_xGa_{1-x}P$,[78,185] $Cd_xZn_{1-x}Te$,[81–83] and $Cd_xMn_{1-x}Te$.[102] In the dilute limit, this model corresponds to model 2b except that it does not apply the two approximations made by all the VFF models described in Sec. III C 1, namely, including only the harmonic terms of the VFF potential (A1) and approximating the geometric relation between A-C and B-C distances (A2). In order to investigate the influence of these approximations, the element-specific bond lengths were calculated for the dilute limit based on model 5 but applying either A1 or A2.[78] The associated ϵ values for $In_xGa_{1-x}P$ are listed in Table VI.

In a similar approach, the minimum-energy structural parameters of the five different first nearest neighbor configurations were calculated for $In_xGa_{1-x}As$ relaxing not only the central As atom but also its first nearest neighbor cations and its second nearest neighbor As atoms.[126,186,187] The resulting clusters consist of seventeen atoms connected by sixteen bonds and are embedded in a virtual crystal media. Furthermore, bond stretching and bond bending terms of the VFF potential were included in the calculation. The element-specific In-As and Ga-As bond lengths are then obtained as the weighted average over the five different clusters assuming again a binomial Bernoulli distribution. The results are in excellent agreement with the experimental values not only for $In_xGa_{1-x}As$ bulk alloys but also for strained thin films.

A somewhat different approach considers the alloy as a network of springs described by the Kirkwood VFF potential[137] with one set of bond stretching and bond bending force constants.[142,188,189] Within this framework, the element-specific first nearest neighbor distance distributions are calculated using a Green's function formalism.[189] The average distance thus obtained for each atomic pair is a linear function of composition x with a slope determined by the topological rigidity parameter, a^{**}. This property describes the competing effects of bond length and bond angle relaxation in the alloy structure and is identical to the relaxation parameter, ϵ. Evaluating a^{**} with the Green's function formalism, an interpolation formula is derived that expresses a^{**} in terms of the ratio of bond bending to bond stretching force constants. For most III-V and II-VI semiconductor alloys, β/α is between 0.1 and 0.2 (see Tables III–V) resulting in a topological rigidity parameter of around 0.75.[189] The basic model (model 6a) takes a^{**} as the mean value of the binary parent compounds and yields two parallel lines for the

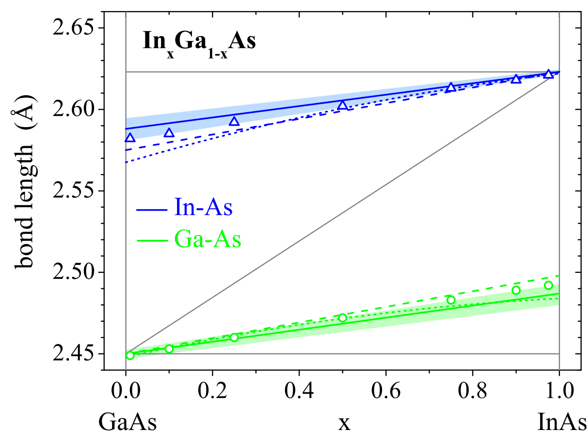

FIG. 26. Element-specific In-As (blue) and Ga-As (green) bond lengths as a function of composition x for $In_xGa_{1-x}As$. The solid lines show the best linear fits to the experimental data plotted in Fig. 8 and the shaded areas represent the associated experimental uncertainties. The open symbols show the bond lengths calculated with model 5 (Ref. 102) while the dashed and dotted lines represent the predictions made by models 6a (Ref. 142) and 7 (Ref. 182), respectively. The thin gray lines represent the binary values and the ones predicted by the VCA.

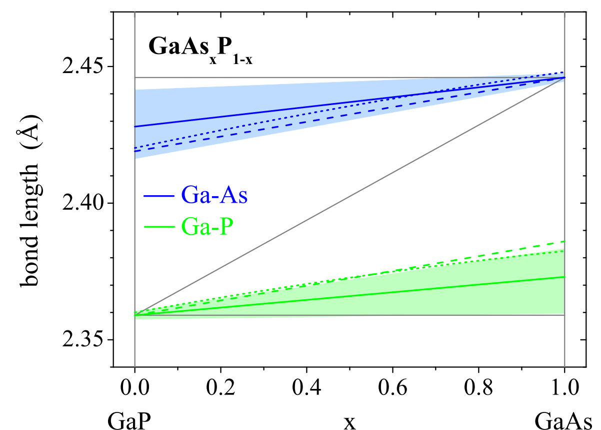

FIG. 27. Element-specific Ga-As (blue) and Ga-P (green) bond lengths as a function of composition x for $GaAs_xP_{1-x}$. The solid lines show the best linear fits to the experimental data plotted in Fig. 9 and the shaded areas represent the associated experimental uncertainties. The dashed and dotted lines represent the predictions made by models 6a (Ref. 142) and 7 (Ref. 182), respectively. The thin gray lines represent the binary values and the ones predicted by the VCA.

This article is copyrighted as indicated in the article. Reuse of AIP content is subject to the terms at: http://scitation.aip.org/termsconditions. Downloaded to IP: 131.169.38.71 On: Tue, 17 Nov 2015 09:25:17

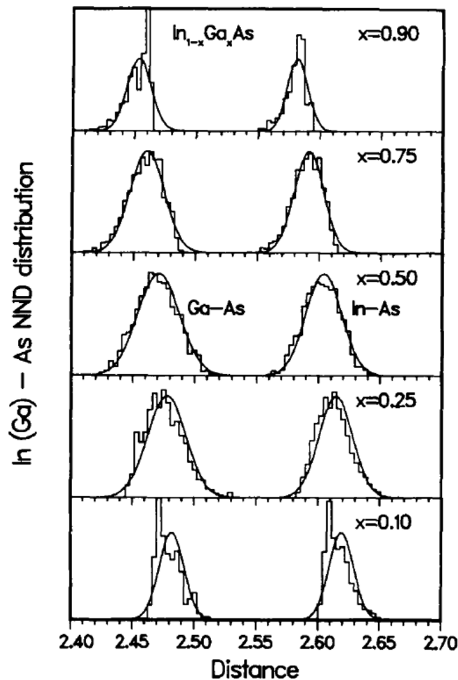

FIG. 28. Calculated first nearest neighbor distance distribution obtained by minimizing the VFF distortion energy of a large $In_{1-x}Ga_xAs$ cluster. Note that here the composition x represents the Ga content of the material. Reprinted with permission from Podgórny *et al.*, "Crystallographic structure of ternary semiconducting alloys," Solid State Commun. **55**, 413–417 (1985). Copyright 1985 Elsevier.

two different bond lengths as shown in Figs. 26 and 27 for $In_xGa_{1-x}As$ and $GaAs_xP_{1-x}$, respectively.[142] The calculation slightly overestimates the change in the first nearest neighbor distances but is still in fairly good agreement with the experimental values. An extended model (model 6b) takes into account the different force constants of the binary parent compounds using an effective-medium approximation.[142] The resulting curves exhibit a slightly nonlinear behavior; however, the bowing is typically within the uncertainty of the experimental data and is thus difficult to be verified. The ϵ values obtained for $In_xGa_{1-x}P$ with both versions are listed in Table VI.

3. Cluster and supercell calculations

The local structure of ternary alloys was also modeled by simulating large atomic clusters or supercells. Using the VFF potential with bond stretching and bond bending terms to relax the atomic positions of $In_xGa_{1-x}As$ clusters yielded a bimodal first nearest neighbor distance distribution corresponding to In-As and Ga-As bonds in good agreement with the experimental EXAFS results.[83,84,113,190] Figure 28 plots the first nearest neighbor distance distribution for five different alloy compositions as an example.[190] It was also demonstrated once more, that neglecting cation relaxation *or* bond bending leads to values that differ significantly more from the experimental data than those obtained with calculations neglecting both effects.[83,84,190] A bimodal first nearest neighbor distance distribution was also obtained for clusters relaxed on the basis of the VFF potential for $In_{0.5}Ga_{0.5}P$,[62,191,192] $Hg_xZn_{1-x}Te$,[86] $GaAs_xP_{1-x}$,[193] $GaAs_xN_{1-x}$,[193] and $ZnTe_xSe_{1-x}$.[194]

In a similar approach (model 7), the atomic-scale structure of eighteen III-V and eleven II-VI ternary alloys was modeled by minimizing the VFF distortion energy for a variety of compositions.[182] In all cases, two distinct bond length distributions were observed corresponding to the two different types of first nearest neighbor pairs. The average values exhibit a slightly nonlinear change with composition x and can be fitted with quadratic polynomials the parameters of which are reported for all 29 materials. The results for $In_xGa_{1-x}As$ and $GaAs_xP_{1-x}$ are plotted in Figs. 26 and 27, respectively. The values slightly overestimate the change in the first nearest neighbor distances similar to the predictions by model 6a. The ϵ values obtained for $In_xGa_{1-x}P$ are listed in Table VI.

A somewhat different approach (model 8) starts from a thermodynamic description of the alloy structure including energetic and entropic terms in order to model local structural parameters of $In_xGa_{1-x}P$.[183] The distortion energy is again taken as a modified VFF potential while the configurational and vibrational degrees of freedom are treated using Monte Carlo calculations. Distinct In-P and Ga-P bond lengths are obtained that change linearly with composition x and are close to the experimental EXAFS values. The corresponding ϵ values are listed in Table VI. Molecular dynamics simulations were applied to model large clusters of $In_xGa_{1-x}As$ yielding once more a bimodal bond length distribution with average Ga-As and In-As distances closer to those of GaAs and InAs than to the ones predicted by the VCA.[195–197] Last but not least, model 9 uses first-principles self-consistent local-density total-energy minimization to calculate the first nearest neighbor distances of $In_xGa_{1-x}P$.[184] The In-P and Ga-P bond lengths are again very different from each other, show a linear dependence on the composition x, and yield a relaxation parameter $\epsilon \sim 0.80$ in excellent agreement with experimental results (see Table VI). For *ordered* alloys, the calculated In-P and Ga-P first nearest neighbor distances deviate even less from the binary values[184,185,191,192] while local clustering of the cations is predicted to yield a somewhat larger change in the In-P and Ga-P bond lengths than observed for the random alloy.[62]

4. Comparison of different first shell models

All models for ternary alloys discussed above yield a bimodal first nearest neighbor distance distribution with bond lengths closer to those of the binary parent compounds than to the ones predicted by the VCA. The models differ, however, with regard to how much the first nearest neighbor distances are predicted to change with composition x and whether they vary linearly or not. Table VI lists the relaxation parameter ϵ obtained with various models for the case of $In_xGa_{1-x}P$ together with the experimental EXAFS results from Table II. Using different values of bond stretching and bond bending force constants (see Tables III–V) for any given model yields only small differences in ϵ, typically less than 0.02.

In contrast, the choice of approximations turns out to be a crucial factor in determining the resulting ϵ value. As discussed above, including neither the bond bending terms nor the relaxation of the second nearest neighbor shell gives

This article is copyrighted as indicated in the article. Reuse of AIP content is subject to the terms at: http://scitation.aip.org/termsconditions. Downloaded to IP: 131.169.38.71 On: Tue, 17 Nov 2015 09:25:17

better results than including only one of the two effects. In the dilute limit, model 5 corresponds to model 2b except that it does not use the two approximations applied in the latter, namely, including only the harmonic terms of the VFF potential (A1) and approximating the geometric relation between A-C and B-C distances (A2). A detailed analysis of these models and approximations reveals that using a harmonic approximation to the VFF potential does not influence the calculated ϵ values. In contrast, approximating the geometric relationship between the A-C and B-C distances not only changes the absolute values of ϵ but also the ratio between them (see Table VI).[78]

Most models predict a smaller ϵ for the longer In-P bond compared to the shorter Ga-P bond, however, the differences are typically smaller or of similar order as the variation between the different models and caused by the different assumptions. It has been argued that the relaxation in semiconductors extends out to a long range.[189] Nevertheless, the simple models that only consider relaxation of the first nearest neighbor shell yield ϵ values similar to those of the more complex calculations. It is therefore very difficult to judge the appropriateness of certain approximations without performing the complete calculation and comparing the results with experimental values such as those obtained from EXAFS measurements.

Some of the theoretical studies also discuss the widths of the element-specific first nearest neighbor distance distributions.[83,84,142,143,183,188–190] All models and simulations predict an increase of the variance, σ^2, for the alloy compared to the binary parent compounds which is not observed experimentally (see Sec. III A 1). However, in most cases the theoretical values are still within the experimental uncertainties for all alloy compositions.

5. Modeling of higher shells

Second and third nearest neighbor distances of $In_xGa_{1-x}As$ were calculated as weighted average over the structural parameters of the five different cation configurations shown in Fig. 25.[126,187] The clusters consist of the central As atom, the first nearest neighbor cation shell characterized by the number n of In atoms and the twelve second nearest neighbor As atoms. As described in Sec. III C 2, these 17-atom clusters are embedded in a virtual crystal media and structural parameters are determined by minimizing the VFF potential including both bond stretching and bond bending terms. Similar to the first nearest neighbor shell, good agreement between calculated and measured As-In-As, As-Ga-As, In-As-In, In-As-Ga, and Ga-As-Ga second nearest neighbor distances is obtained for both bulk alloys and strained thin films. Regarding the third nearest neighbor shell of bulk alloys, the model predicts similar splittings and behaviors as for the cation-cation second nearest neighbor pairs. As discussed in Sec. III A 3, the various third nearest neighbor distances cannot be distinguished experimentally. Nevertheless, the calculated average In-As and Ga-As third nearest neighbor distances closely follow the ones predicted by the VCA in perfect accord with the experimental results for $In_xGa_{1-x}P$.[78] For strained epitaxial films, the splitting between *in plane* and *out of plane* third nearest neighbor distances observed experimentally is also very well reproduced by the calculations demonstrating the strong capabilities of this rather simple model.[126,187]

General analytic expressions for the average distances of the various second nearest neighbor pairs of $A_xB_{1-x}C$ or CA_xB_{1-x} ternary alloys were derived based on the spring network model and a Green's function formalism (model 6a, see Sec. III C 2).[142,189] For the common sublattice, two distinct second nearest neighbor distances were obtained corresponding to the two possible bridging atoms on the mixed sublattice, namely, C-A-C and C-B-C. These two distances remain close to the binary values over the whole compositional range. For $a^{**} \equiv \epsilon = 0.80$, the slope of the two parallel, linear curves amounts to 20% of that predicted by the VCA similar to what is observed for the first nearest neighbor distances. For the mixed sublattice, three second nearest neighbor distances can be distinguished corresponding to the three possible A-C-A, A-C-B, and B-C-B second nearest neighbor pairs. These distances also vary linearly with composition x but they are much closer to the ones predicted by the VCA than to the binary values. For $a^{**} \equiv \epsilon = 0.80$, the slope equals 70% of that predicted by the VCA. The curves for $In_xGa_{1-x}As$ and $GaAs_xP_{1-x}$ are shown in Figs. 29 and 30, respectively, using $a^{**} \equiv \epsilon = 0.80$ in accordance with the best linear fit to the first nearest neighbor distances (see Table II). The model predictions agree well with the experimental data for all five second nearest neighbor pairs. Excellent agreement was also found for the cation-cation distances of $In_xGa_{1-x}P$.[78]

Second nearest neighbor distances of $In_xGa_{1-x}As$ were also evaluated with cluster simulations by minimizing the

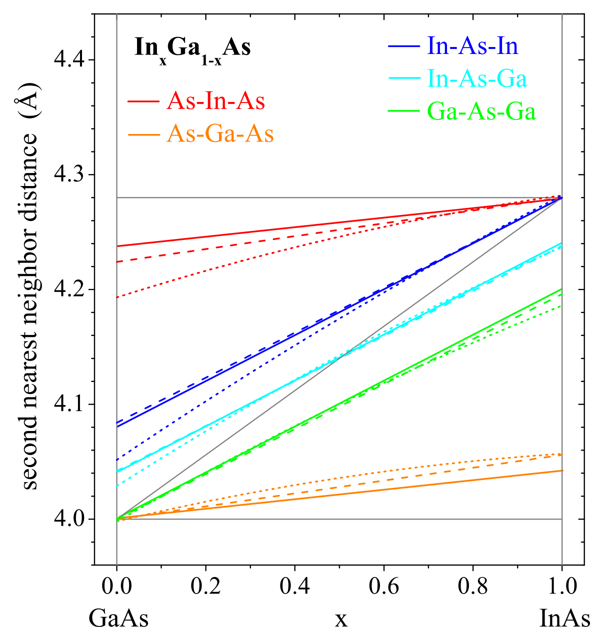

FIG. 29. Element-specific second nearest neighbor distances as a function of composition x for $In_xGa_{1-x}As$. The solid lines are taken from Fig. 13 and represent the experimental data. The uncertainties have been omitted for clarity but can be assessed in Fig. 13. The dashed and dotted lines represent the predictions made by models 6a (Ref. 142) and 7 (Ref. 182), respectively. The thin gray lines represent the binary values and the ones predicted by the VCA.

This article is copyrighted as indicated in the article. Reuse of AIP content is subject to the terms at: http://scitation.aip.org/termsconditions. Downloaded to IP: 131.169.38.71 On: Tue, 17 Nov 2015 09:25:17

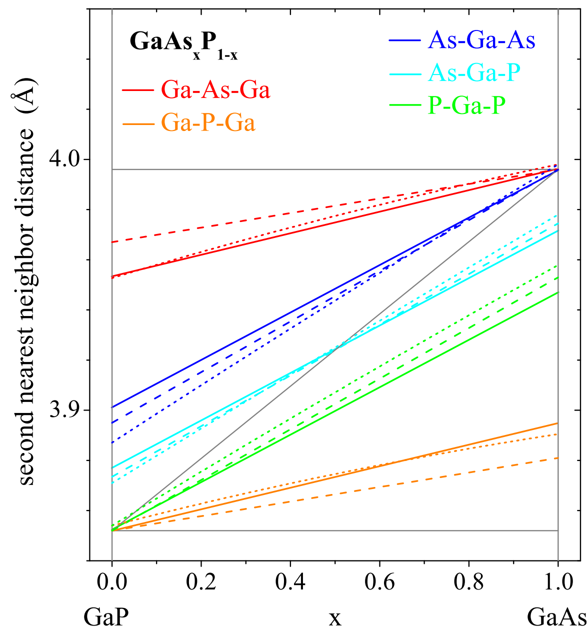

FIG. 30. Element-specific second nearest neighbor distances as a function of composition x for $GaAs_xP_{1-x}$. The solid lines are taken from Fig. 14 and represent the experimental data. The uncertainties have been omitted for clarity but can be assessed in Fig. 14. The dashed and dotted lines represent the predictions made by models 6a (Ref. 142) and 7 (Ref. 182), respectively. The thin gray lines represent the binary values and the ones predicted by the VCA.

distortion energy taken as the VFF potential including bond stretching and bond bending terms as described in Sec. III C 3.[83,84,102,113,115,190] Figures 31(a) and 31(b) plot the second nearest neighbor distance distributions associated with the mixed cation sublattice and the common anion sublattice, respectively, for five different alloy compositions.[190] For the In-As-In and Ga-As-Ga pairs, broad Gaussian-shaped distance distributions are observed the average values of which increase by approximately 0.2 Å when going from $x = 0$ to $x = 1$. Furthermore, the average In-As-In distance is about 0.08 Å larger than the average Ga-As-Ga distance for all compositions studied. In contrast, the second nearest neighbor As distance distribution is extremely broad and features multiple peaks. They can be grouped into an As-In-As and an As-Ga-As distribution with up to three peaks each. A multimodal anion-anion distribution was also observed for $Cd_xZn_{1-x}Te$ in a similar approach.[81,82] The average As-In-As distance is larger than the average As-Ga-As distance by approximately 0.2 Å while both values change by only 0.05 Å over the whole compositional range. These findings are in excellent agreement with the experimental data shown in Fig. 13. The widths of the In-As-In, Ga-As-Ga, As-In-As, and As-Ga-As distance distributions are larger for the alloys than for the binary parent compounds and reach maximum values at $x \sim 0.5$.[83,113,115,190] A splitting of the second nearest neighbor As distance distribution and a significant broadening of both cation-cation and anion-anion distance distributions in the ternary alloys were further observed by molecular dynamics simulations of large $In_xGa_{1-x}As$ clusters.[195,196]

Second nearest neighbor structural parameters were also modeled for eighteen III-V and eleven II-VI ternary alloys by minimizing the VFF distortion energy for clusters of different alloy composition (model 7, see Sec. III C 3).[182] The resulting distance distribution for each of the five second nearest neighbor pairs consists of three different peaks determined by the configuration of the surrounding coordination shells. For the atoms of the mixed sublattice, the spacing is rather small and the peaks mostly overlap leading to one broad distribution as already observed for $In_xGa_{1-x}As$.[190] In contrast, the spacing is large for the common sublattice resulting in a multimodal distribution as reported above. The composition dependence of the average distances is again well represented by quadratic polynomials with a small non-linear contribution. The parameters are reported for all 29 materials. The results for $In_xGa_{1-x}As$ and $GaAs_xP_{1-x}$ are

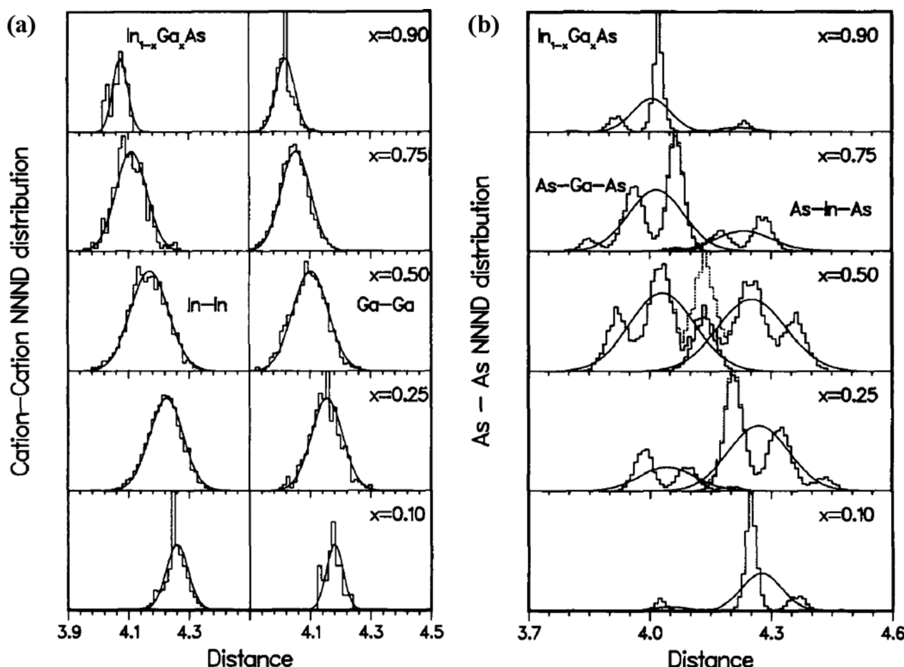

FIG. 31. Calculated second nearest neighbor distance distribution for (a) the mixed cation sublattice and (b) the common anion sublattice of $In_{1-x}Ga_xAs$. Note that here the composition x represents the Ga content of the material. The distributions were obtained by minimizing the VFF distortion energy of a large atomic cluster. Reprinted with permission from Podgórny *et al.*, "Crystallographic structure of ternary semiconducting alloys," Solid State Commun. **55**, 413–417 (1985). Copyright 1985 Elsevier.

This article is copyrighted as indicated in the article. Reuse of AIP content is subject to the terms at: http://scitation.aip.org/termsconditions. Downloaded to IP: 131.169.38.71 On: Tue, 17 Nov 2015 09:25:17

plotted in Figs. 29 and 30, respectively. Good agreement is observed with both the experimental data and the spring network model (model 6a). Similar findings are reported for $Cd_xZn_{1-x}Te$.[85]

Similar second nearest neighbor distance distributions were also obtained for $In_xGa_{1-x}P$ using a thermodynamic description of the alloy structure including energetic and entropic terms (model 8, see Sec. III C 3).[183] Again, the In-P-In, In-P-Ga and Ga-P-Ga pairs of the mixed sublattice show broad Gaussian-shaped distance distributions while the P-*i*-P pairs of the common sublattice (*i* denoting either In or Ga) exhibit a clearly multimodal distance distribution with several distinct peaks. The widths of the distributions are once more larger for the ternary alloys than for the binary parent compounds and reach maximum values at a composition of approximately 0.5. Hence, both anions and cations are displaced from their ideal lattice sites; however, the displacement of the anions is much larger for these cation-mixed systems.[113,182,183,190] The distortion of the common sublattice is thus significantly greater than the distortion of the mixed sublattice as already inferred from the experimental second nearest neighbor distances discussed in Sec. III A 2.

Analyzing the simulated bond angles of $In_xGa_{1-x}P$, broad distributions with angles as low as 100° and as high as 120° where found for the *i*-P-*j*, P-Ga-P, and P-In-P angles where *i* and *j* denote either In or Ga.[183] This clearly demonstrates that the lattice mismatch is accommodated to a large extent by bond angle relaxation as already discussed in Sec. III A. Nevertheless, all three distributions are mostly centered around the ideal value of 109.5° in good agreement with experimental findings. As can be seen in Fig. 20(a), the average As-In-As and As-Ga-As angles of $In_xGa_{1-x}As$ remain close to the ideal value over the whole compositional range. Given the similarity of the materials, the same can be expected for $In_xGa_{1-x}P$. In contrast, the *i*-As-*j* and *i*-P-*j* angles strongly deviate from the ideal value depending on the kind of atoms involved (Fig. 20(b) and Ref. 78, respectively). Nevertheless, the weighted average over all *i*-As-*j* or *i*-P-*j* angles still closely resembles the ideal value as predicted by the cluster calculations.

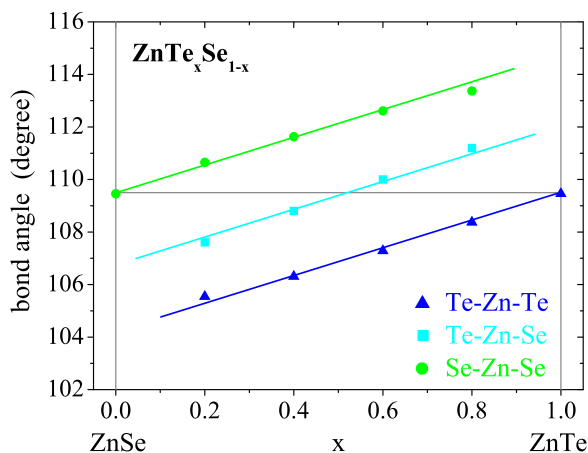

FIG. 32. Simulated *i*-Zn-*j* bond angles as a function of composition *x* for $ZnTe_xSe_{1-x}$, where *i* and *j* denote either Te or Se.[194] The solid lines all have the same slope and are a guide to the eye while the ideal zincblende value of 109.5° is given as a thin gray line.

Tetrahedral bond angles were also obtained for $ZnTe_xSe_{1-x}$ clusters relaxed by minimizing the VFF distortion energy.[194] Figure 32 plots the simulated Te-Zn-Te, Te-Zn-Se, and Se-Zn-Se angles as a function of composition *x*. The Te-Zn-Te angle of the ternary alloy is always smaller than the ideal zincblende value whereas the Se-Zn-Se angle is larger for all alloy compositions. The Te-Zn-Se angle exhibits intermediate values. Furthermore, all three angles show a similar linear increase with increasing Te content. These findings are in excellent agreement with the experimental results for $ZnTe_xSe_{1-x}$,[92] $In_xGa_{1-x}As$ (see Fig. 20(b)), and $In_xGa_{1-x}P$[78] and highlight once more the large extent of bond angle relaxation in ternary III-V and II-VI zincblende alloys.

D. Atomic displacements

As discussed in Secs. III A and III C, the A-C and B-C bond lengths of $A_xB_{1-x}C$ or CA_xB_{1-x} ternary alloys with zincblende structure are distinctly different from each other and remain close to the values of the binary parent compounds. The lattice mismatch between the latter is thus accommodated mostly by bond angle relaxation and only to a small extent by bond length relaxation. Furthermore, the second nearest neighbor distance distributions in the ternary alloys are significantly broadened compared to the binary parent compounds for both the common and the mixed sublattice as deduced from experiments[32,78,92,113–115,134] and simulations.[83,182,183,190,195,196] As a consequence, the atoms on both sublattices are displaced from their ideal crystallographic positions depending on the nature of the neighboring atoms.

Nevertheless, the resulting atomic displacements are distinctly different for the common and mixed sublattices as seen by both experiment[32,77,78,81–85,90,92,99,100] and simulation.[83,182,183,190,195,196] The second nearest neighbor distances associated with the common sublattice show a well-spaced multimodal distribution that can be divided into two distinct C-A-C and C-B-C contributions the average values of which are closer to the values of the binary parent compounds than the ones predicted by the VCA. In contrast, the second nearest neighbor distance distributions associated with the different atomic pairs of the mixed sublattice exhibit broadened yet nearly Gaussian shapes the average values of which are much closer to the ones predicted by the VCA than to the values of the binary parent compounds. The atoms of the common sublattice are thus significantly more displaced from their ideal crystallographic positions than the atoms occupying the mixed sublattice.[92,113–115,182,183,190]

Apart from the magnitude of displacement, the common and mixed sublattices also differ with respect to the direction in which the atoms are displaced. Analyzing the atomic positions of $In_xGa_{1-x}As$ supercells relaxed by minimizing the VFF distortion energy yields the average three-dimensional atomic probability distribution of As anions and In and Ga cations.[115] Figures 33 and 34 plot the isoprobability surfaces for anions and cations, respectively. Clearly, the displacements of the As atoms are highly symmetric yet strongly directional and occur predominantly in the ⟨100⟩ and ⟨111⟩ directions. In contrast, the probability distribution of the In

This article is copyrighted as indicated in the article. Reuse of AIP content is subject to the terms at: http://scitation.aip.org/termsconditions. Downloaded to IP: 131.169.38.71 On: Tue, 17 Nov 2015 09:25:17

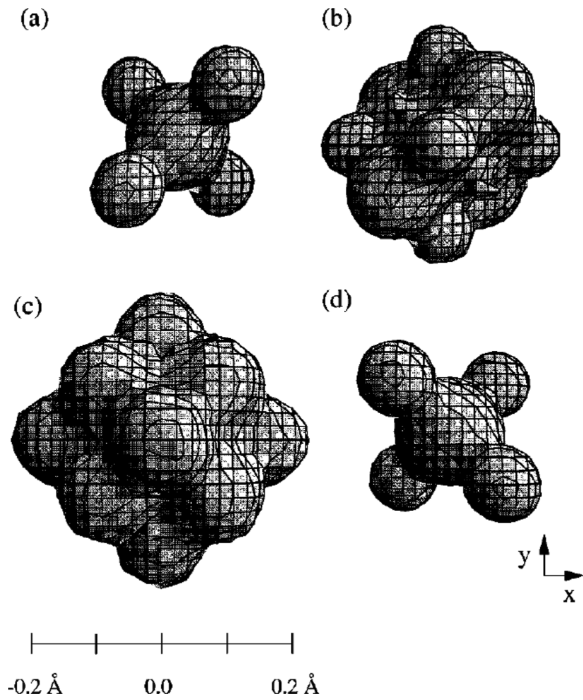

FIG. 33. Isoprobability surface viewed along the [001] direction for the ensemble averaged As atom distribution of $In_xGa_{1-x}As$ with (a) $x = 0.17$, (b) $x = 0.33$, (c) $x = 0.50$, and (d) $x = 0.83$. The surfaces enclose the volume where the anion will be found with a probability of 68%. Reprinted with permission from Jeong *et al.*, Phys. Rev. B **63**, 205202 (2001). Copyright 2001 The American Physical Society.

and Ga atoms is nearly isotropic and sharply peaked at the ideal crystallographic lattice site. Furthermore, the As displacements are about two times larger than those of the In or Ga atoms. These findings thus partly explain the success of

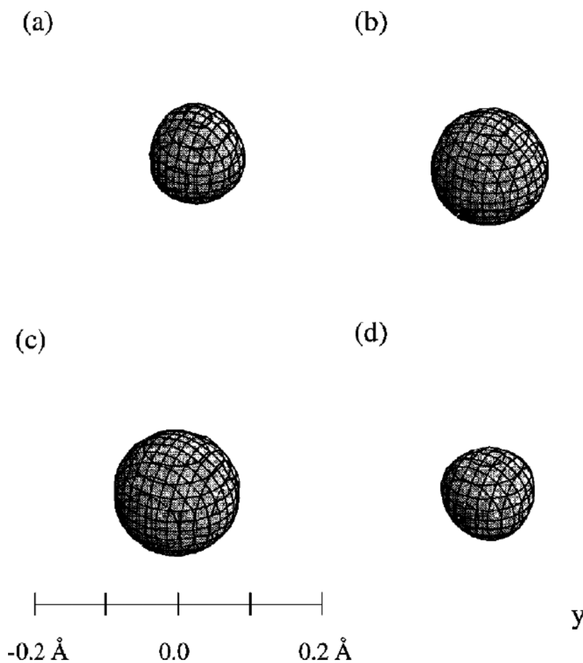

FIG. 34. Isoprobability surface viewed along the [001] direction for the ensemble averaged In and Ga atom distribution of $In_xGa_{1-x}As$ with (a) $x = 0.17$, (b) $x = 0.33$, (c) $x = 0.50$, and (d) $x = 0.83$. The surfaces enclose the volume where the cations will be found with a probability of 68%. Reprinted with permission from Jeong *et al.*, Phys. Rev. B **63**, 205202 (2001). Copyright 2001 The American Physical Society.

the model predictions discussed in Sec. III C, which neglect both the relaxation of the mixed sublattice and the bond bending distortion energy.

The highly directional displacements of the atoms occupying the common sublattice can be easily understood in terms of the different first nearest neighbor environments shown in Fig. 25.[115,185] For $n = 0$ and 4, the first nearest neighbor shell is symmetric and the central C atom is located on its ideal lattice site if the neighboring atoms of the mixed sublattice are not significantly displaced themselves. In contrast, for $n = 1$, the C atom is displaced away from the single A atom and towards the three B atoms if the A-C bond length is larger than the B-C bond length. The displacement occurs along the A-C bond in one of the $\langle 111 \rangle$ directions, for the particular case shown in Fig. 25(b) along $[\bar{1}1\bar{1}]$. Similarly, for $n = 3$, the C atom is displaced away from the three A atoms towards the single B atom. The displacement occurs along the B-C bond again in one of the $\langle 111 \rangle$ directions, for the particular case shown in Fig. 25(d) along $[\bar{1}\bar{1}\bar{1}]$. For $n = 2$, the C atom is displaced away from the two A atoms towards the two B atoms in a symmetric fashion resulting in a displacement along one of the $\langle 100 \rangle$ directions, for the particular case shown in Fig. 25(c) along $[\bar{1}00]$. In summary, no displacement of the central C atom is observed for the configurations with $n = 0$ and 4, displacements along the $\langle 111 \rangle$ directions occur for $n = 1$ and 3, and displacements along the $\langle 100 \rangle$ directions are found for $n = 2$. In a random alloy, all five configurations are present with different probabilities depending on the alloy composition. Consequently, there is no single displacement of the atoms of the common sublattice and the material is characterized by an intrinsic structural inhomogeneity on the subnanometer scale.

The magnitude of these different displacements can be estimated most easily using model 5 described in Sec. III C 2. The first nearest neighbor atoms of the mixed sublattice are fixed at their ideal crystallographic lattice sites given by the alloy lattice constant according to Vegard's Law. Minimizing the bond stretching energy of the four anion-cation bonds then yields the minimum-energy position of the central C atom characterized by the fractional coordinates (x, y, z) within the zincblende unit cell. The atomic displacement (u, v, w) is thus given by

$$\begin{aligned} u &= 0.25 - x, \\ v &= 0.25 - y, \\ w &= 0.25 - z. \end{aligned} \tag{16}$$

For $n = 0$ and 4, no displacement occurs and $u^{(0)} = u^{(4)} = v^{(0)} = v^{(4)} = w^{(0)} = w^{(4)} = 0$. For $n = 1$ and 3, the displacement occurs along the $\langle 111 \rangle$ direction with $|u^{(1)}| = |v^{(1)}| = |w^{(1)}|$ and $|u^{(3)}| = |v^{(3)}| = |w^{(3)}|$ all being different from zero. However, these configurations are present in the random alloy in all possible orientations with equal probability. As a consequence, the average displacement of the C atoms along any of the three unit cell directions vanishes and $\langle u^{(1)} \rangle = \langle v^{(1)} \rangle = \langle w^{(1)} \rangle = 0$ and $\langle u^{(3)} \rangle = \langle v^{(3)} \rangle = \langle w^{(3)} \rangle = 0$. For $n = 2$, the displacement occurs along the $\langle 100 \rangle$ direction such that one of the three values $u^{(2)}$, $v^{(2)}$, and $w^{(2)}$

This article is copyrighted as indicated in the article. Reuse of AIP content is subject to the terms at: http://scitation.aip.org/termsconditions. Downloaded to IP: 131.169.38.71 On: Tue, 17 Nov 2015 09:25:17

is different from zero (positive or negative) while the other two vanish. Again, all possible orientations of this configuration are present with equal probabilities and $\langle u^{(2)}\rangle = \langle v^{(2)}\rangle = \langle w^{(2)}\rangle = 0$. Therefore, the average displacement of all C atoms along any of the three unit cell directions is zero independent of the composition, $\langle u\rangle = \langle v\rangle = \langle w\rangle = 0$, in perfect agreement with the experimental observation that the average long-range structure of the alloy resembles the zincblende crystal structure.

Interestingly, the *overall displacement* of the C atoms from the ideal lattice site, $\delta = \sqrt{u^2 + v^2 + w^2}$, does not vanish even for the random alloy. Obviously, $\delta^{(0)} = \delta^{(4)} = 0$. In contrast, δ is always larger than zero for $n = 1$, 2, and 3 independent of the orientation of the different configurations. As an example, Fig. 35(a) plots the δ values calculated according to model 5 for all five first nearest neighbor configurations surrounding the central P atom in $In_xGa_{1-x}P$ versus composition x.[185] The distance from the ideal lattice site is nearly identical for $n = 1$ and 3 and only slightly higher for $n = 2$ and all three exhibit an almost linear decrease with increasing x. The weighted average $\langle\delta\rangle$ is shown in Fig. 35(b) together with $\langle u\rangle$, $\langle v\rangle$ and $\langle w\rangle$. Clearly, $\langle\delta\rangle$ equals zero only for the binary parent compounds as expected. For the ternary alloy, $\langle\delta\rangle$ is larger than zero over the whole compositional range and exhibits a strong positive bowing with a maximum around $x \sim 0.5$. This means that even though the average *position* of the P atom corresponds to the ideal lattice site, the average *overall displacement* from this ideal lattice site is not equal to zero. The latter is of great importance as a displacement of the anion from its ideal lattice site significantly affects the material bandgap as discussed in Sec. III E.

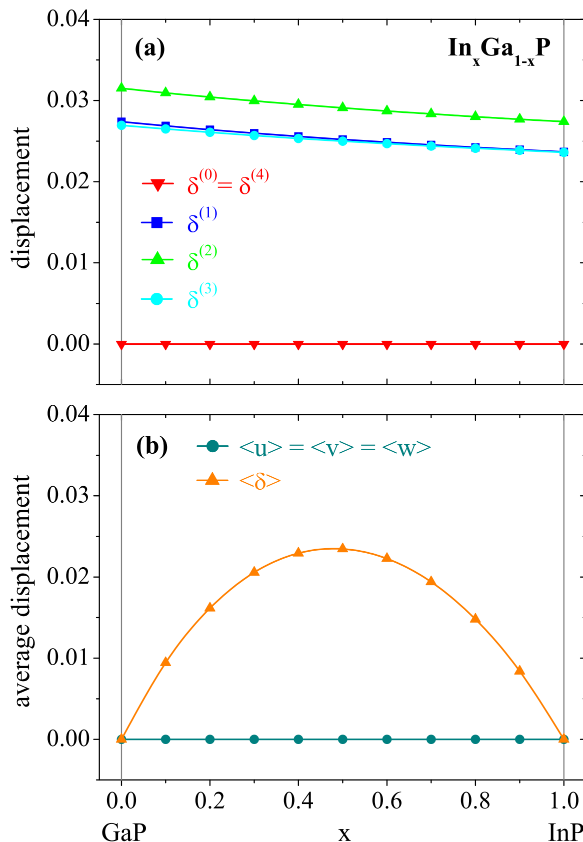

FIG. 35. Calculated displacement of the P atoms in $In_xGa_{1-x}P$ versus composition x.[185] (a) Overall displacement δ from the ideal lattice site for each of the five possible first nearest neighbor configurations surrounding the P anion as shown in Fig. 25. (b) Average displacements $\langle u\rangle$, $\langle v\rangle$, and $\langle w\rangle$ in the x-, y-, and z-directions of the unit cell, respectively, and average overall displacement $\langle\delta\rangle$.

E. Bandgap bowing

1. Experimental bowing parameters

The energies of the different bandgaps typically change continuously but nonlinearly with composition x for $A_xB_{1-x}C$ or CA_xB_{1-x} ternary alloys with zincblende structure.[26,71] In most cases, the bandgap energy can be described by a quadratic function as given in Eq. (2). The lowest direct and indirect bandgap energies for a number of III-V and II-VI binary compounds with zincblende structure are listed in Table I while the corresponding bowing parameters, b, for the ternary alloys are summarized in Table VII. Typically, the bowing parameters are positive and range from 0 to 1 eV for most cation-mixed alloys while values as high as nearly 4 eV have been reported for some anion-mixed alloys. Furthermore, b increases with increasing difference in lattice constants and electronegativity of the binary parent compounds.[26,71]

For the direct semiconductor $In_xGa_{1-x}As$, the composition dependence of the bandgap energy is shown in Fig. 7, whereas Fig. 36 plots the lowest direct and indirect energy gap versus composition x for $In_xGa_{1-x}P$.[26,33,198–200] Room temperature values reported for the lowest direct energy gap are between 2.76 and 2.78 eV for GaP and between 1.34 and 1.35 eV for InP. The lowest indirect energy gap for GaP occurs at 2.26 eV with a cross-over between direct and indirect bandgap for $In_xGa_{1-x}P$ at a composition of $x \sim 0.3$. The bowing parameters reported for the direct energy gap range from 0.50 to 0.79 eV.

TABLE VII. Bowing parameter, b, for the lowest direct energy bandgap of III-V and II-VI ternary alloys with zincblende structure at 300 K.[26]

$A_xB_{1-x}C$	b (eV)	CA_xB_{1-x}	b (eV)
$Ga_xAl_{1-x}P$	0	$AlAs_xP_{1-x}$	
$Ga_xAl_{1-x}As$		$AlSb_xP_{1-x}$	
$Ga_xAl_{1-x}Sb$		$AlSb_xAs_{1-x}$	
$In_xAl_{1-x}P$	0.40	$GaAs_xP_{1-x}$	0.19
$In_xAl_{1-x}As$	0.72	$GaSb_xP_{1-x}$	2.70
$In_xAl_{1-x}Sb$	0.43	$GaSb_xAs_{1-x}$	1.25
$In_xGa_{1-x}P$	0.65	$InAs_xP_{1-x}$	0.15
$In_xGa_{1-x}As$	0.58	$InSb_xP_{1-x}$	1.60
$In_xGa_{1-x}Sb$	0.42	$InSb_xAs_{1-x}$	0.60
$Cd_xZn_{1-x}S$	0.83	$ZnSe_xS_{1-x}$	0.58
$Cd_xZn_{1-x}Se$	0.39	$ZnTe_xS_{1-x}$	3.75
$Cd_xZn_{1-x}Te$	0.31	$ZnTe_xSe_{1-x}$	1.50
$Hg_xZn_{1-x}S$	1.00	$CdSe_xS_{1-x}$	
$Hg_xZn_{1-x}Se$		$CdTe_xS_{1-x}$	1.80
$Hg_xZn_{1-x}Te$	0.46	$CdTe_xSe_{1-x}$	0.84
$Hg_xCd_{1-x}S$		$HgSe_xS_{1-x}$	
$Hg_xCd_{1-x}Se$	0	$HgTe_xS_{1-x}$	
$Hg_xCd_{1-x}Te$	0.21	$HgTe_xSe_{1-x}$	

This article is copyrighted as indicated in the article. Reuse of AIP content is subject to the terms at: http://scitation.aip.org/termsconditions. Downloaded to IP: 131.169.38.71 On: Tue, 17 Nov 2015 09:25:17

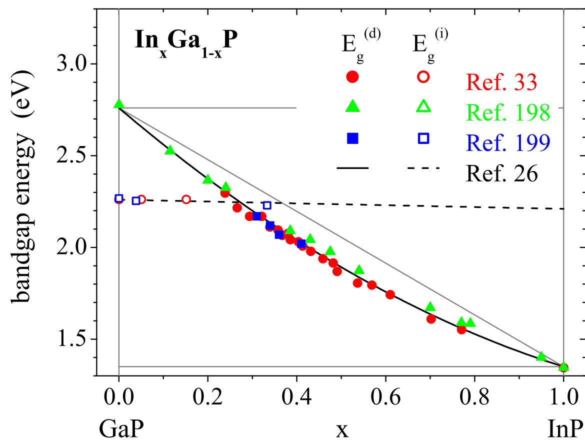

FIG. 36. Lowest direct (full symbols) and indirect (open symbols) bandgap energy versus composition x for $In_xGa_{1-x}P$. The data are taken from Refs. 33 (red circles), 198 (green triangles), and 199 (blue squares). The solid black line corresponds to a quadratic dependence as given by Eq. (2) with an average bowing parameter, b, of 0.65 eV, while the dashed black line shows the linear change between the lowest indirect bandgap, E_g^X, of GaP and InP.[26] The thin gray lines represent the binary values and their weighted average.

2. Theoretical models

A number of different models have been proposed to explain and predict the bandgap bowing in ternary III-V and II-VI semiconductor alloys and care has to be taken when comparing the various works since the different authors often use similar expressions for different physical effects. In particular, the term "disorder" is often used with different meanings. An excellent overview of the different approaches to model the bandgap bowing is presented in Ref. 201. Here, a short summary is given focusing on the aspects related to the correlation between atomic-scale structure and alloy bandgap.

The earliest models of the bandgap bowing in $A_xB_{1-x}C$ or CA_xB_{1-x} alloys are based on the VCA assuming a perfect zincblende structure where the mixed sublattice is occupied by a single virtual element that represents the weighted average of the A and B species.[202] As a consequence, chemical effects such as charge redistribution or polarization due to the different properties of the A and B atoms are neglected. Similarly, structural effects caused by the unequal A-C and B-C bond lengths and the resulting atomic displacements are not taken into account either. Nevertheless, even within the framework of the VCA the alloys can exhibit bandgap bowing because the bandgap energy is not a linear function of the potential for most methods of band-structure calculation.[201,202] Bowing parameters were calculated based on the VCA approach using the dielectric two-band method,[202,203] the empirical pseudopotential method,[204–209] and the empirical tight-binding method.[210–213] In many cases, the calculated b values are significantly smaller than those observed experimentally and it was proposed to separate the bowing parameter into a contribution b_I already present in a fictitiously periodic alloy and a contribution b_{II} due to disorder effects caused by the aperiodicity of random alloys with distinct A and B atoms[202]

$$b = b_I + b_{II}. \tag{17}$$

In the framework of the VCA models, the first term is taken as the calculated value, $b_I = b_{VCA}$, whereas the disorder term is taken as the difference between the experimentally observed and calculated value, $b_{II} = b_{exp} - b_I$. However, the b_{VCA} values vary significantly depending on the method of calculation used and the potential parameters chosen.[201] For example, calculations using the dielectric two-band method yield bowing parameters that are noticeably smaller than those observed experimentally for various III-V and II-VI alloys.[202] In contrast, some empirical pseudopotential calculations result in bowing parameters comparable with the experimental ones for a number of different III-V and II-VI alloys[205,207] while other calculations for $In_xGa_{1-x}As$ find b_{II} to be significant.[208] As a consequence, the relative importance of the two different bowing contributions b_I and b_{II} cannot be reliably evaluated based on the VCA approach. Direct estimations of the disorder term b_{II} were performed using perturbation theory resulting once more in significant contributions to the experimentally observed bandgap bowing for several III-V and II-VI ternary alloys.[214–216]

The effects of chemical disorder due to the different energies of the A-C and B-C bonds are taken into account using the coherent-potential approximation (CPA).[217–223] The calculated bowing parameters for $Ga_xAl_{1-x}As$, $In_xGa_{1-x}P$, $In_xGa_{1-x}As$, and $GaAs_xP_{1-x}$ are larger than those obtained with the VCA approach demonstrating the significance of disorder effects taken as $b_{II} = b_{CPA} - b_{VCA}$.[217,220] However, the fraction of b that is assigned to disorder effects strongly varies for different materials and also depends on the details of the VCA calculation as discussed above. In addition to chemical disorder, effects of structural disorder due to the different A-C and B-C bond lengths are considered for $In_xGa_{1-x}As$ and $ZnTe_xSe_{1-x}$ applying a molecular coherent-potential approximation[224,225] and for $In_{0.5}Ga_{0.5}P$ with a chalcopyrite structure using all-electron first-principles mixed-based band structure calculations.[226] The effects arising from structural relaxation are found to be of a similar magnitude as the effects caused by the chemical differences of the A-C and B-C bonds demonstrating for the first time the significance of the atomic-scale structure for electronic properties such as the bandgap energy.

Based on these findings, the decomposition of the bowing parameter, b, into three separate contributions has been proposed corresponding to the transformation of the AC and BC binary parent compounds to the $A_xB_{1-x}C$ ternary alloy via three subsequent steps.[201,227–229] (i) In the first step, the AC and BC compounds are compressed and dilated, respectively, from their binary lattice constants, a_A and a_B, to the alloy lattice constant, $a(x)$. This volume change leads to a change in the bandgap energy given by the hydrostatic deformation potential, $\gamma = dE/d(\ln V)$, where $V = a^3$ represents the volume of the unit cell. The resulting energy differences for the AC and BC compounds can be written as

$$\begin{aligned} \Delta E_g^A(x) &= 3\gamma_A \ln[a_A/a(x)], \\ \Delta E_g^B(x) &= 3\gamma_B \ln[a_B/a(x)]. \end{aligned} \tag{18}$$

Taking a fraction x of the compressed AC compound and a fraction $(1-x)$ of the dilated BC compound thus yields an energy change ΔE_g^{VD} due to *volume deformation* of

This article is copyrighted as indicated in the article. Reuse of AIP content is subject to the terms at: http://scitation.aip.org/termsconditions. Downloaded to IP: 131.169.38.71 On: Tue, 17 Nov 2015 09:25:17

$$\Delta E_g^{VD}(x) = x\Delta E_g^A(x) + (1-x)\Delta E_g^B(x) = 3x\gamma_A \ln[a_A/a(x)] + 3(1-x)\gamma_B \ln[a_B/a(x)]. \quad (19)$$

This bowing contribution reflects the differences in lattice constants and hydrostatic deformation potentials of the two binary parent compounds. (ii) In the second step, the appropriate fractions of AC and BC compounds with the alloy lattice constant are mixed together allowing for a charge redistribution between the A, B, and C atoms while maintaining the perfect zincblende structure. This *charge redistribution* reflects the difference in chemical electronegativity and yields the energy change ΔE_g^{CE}. (iii) In the third step, the atoms are allowed to relax to their minimum-energy configuration thus realizing the actual alloy structure. The resulting energy difference due to *structural relaxation* is denoted by ΔE_g^{SR} and reflects the difference between the average A-C and B-C bond lengths in the ternary alloy. The overall bandgap bowing then amounts to the sum of the contributions due to volume deformation, charge redistribution, and structural relaxation

$$\Delta E_g = \Delta E_g^{VD} + \Delta E_g^{CE} + \Delta E_g^{SR} \quad (20)$$

with the total bowing parameter

$$b = b^{VD} + b^{CE} + b^{SR}. \quad (21)$$

It is worth noting that these three contributions to the bandgap bowing represent different structural and electronic aspects. The volume deformation contribution arises from a geometrical change in the bond lengths while the symmetry of the AC and BC compounds is fully preserved. ΔE_g^{VD} thus represents a purely structural effect. In contrast, the charge redistribution of the second step takes place for a fixed structural arrangement and thus represents a purely electronic effect due to the different chemical properties of the A, B, and C atoms. Interestingly, the subsequent structural relaxation changes the local atomic structure, most prominently the element-specific bond lengths, while it also allows for a further charge redistribution accompanying the structural changes. ΔE_g^{SR} thus represents a combination of both structural and electronic effects.

The decomposition of the bowing parameter into contributions due to volume deformation, charge redistribution, and structural relaxation has been studied for $ZnSe_{0.5}S_{0.5}$, $ZnTe_{0.5}S_{0.5}$, and $ZnTe_{0.5}Se_{0.5}$ using all-electron mixed-basis band structure calculations.[201,227] However, instead of modeling a random alloy structure, CuAu-like ordering was assumed for the ternary compounds. In this case, the mixed sublattice consists of layers with either A *or* B atoms alternating along one of the $\langle 100 \rangle$ directions leading to space group $P\bar{4}m2$. Assuming such an ordered structure instead of a random alloy significantly simplifies the calculations and maintains all the electronic and structural effects arising from the different geometrical and chemical properties of the A-C and B-C bonds. It does, however, neglect the disorder effects of a truly random alloy such that the calculated bowing parameter corresponds to b_I in Eq. (17). For all three ternary compounds, volume deformation yields a negative contribution to the bandgap bowing while charge redistribution and structural relaxation result in positive bowing. Furthermore, the contribution due to structural relaxation is larger than that arising from charge redistribution in all three cases and the absolute value of each contribution increases from $ZnSe_{0.5}S_{0.5}$ over $ZnTe_{0.5}Se_{0.5}$ to $ZnTe_{0.5}S_{0.5}$. The total bowing parameters agree reasonably well with the experimental values given in Table VII.

A similar study uses the first-principles semirelativistic linear augmented-plane-wave method to calculate the individual bowing contributions of $GaSb_{0.5}As_{0.5}$ with chalcopyrite, CuAu-like or CuPt-like ordering.[228] For the latter, the mixed sublattice consists of layers with either A *or* B atoms alternating along one of the $\langle 111 \rangle$ directions leading to space group R3*m*. The calculated contribution due to volume deformation is almost zero for all three structures while structural relaxation yields again a positive contribution larger than or equal to that arising from charge redistribution. The total bowing parameter depends sensitively on the type of long-range order with the chalcopyrite structure producing the smallest and the CuPt-like structure the largest bandgap bowing. Similar observations were also made for other III-V and II-VI ternary compounds.[230]

The dependence of the bowing parameter on the type of long-range order raises the question to what extent the bandgap bowing is comparable in ordered ternary compounds and random ternary alloys. Even without long-range order, a variation of the bandgap was observed for different configurations of large $In_{0.5}Ga_{0.5}P$ supercells highlighting the statistical nature of alloy properties.[192] Reliable band structure calculations for random alloys have long been hampered by the need for averaging a large number of different configurations or using large supercells with more than thousand atoms[231,232] for which first-principles self-consistent calculations are still often impractical. This difficulty can be overcome by the use of so-called special quasi-random structures (SQS).[233–235] These SQS consist of periodic structures the unit cells of which are designed specifically to best mimic the correlation functions of a random alloy. A rather good match is obtained already with a fairly small number of atoms in the order of ten to twenty thus enabling the use of sophisticated first-principles approaches for the band structure calculations.

Total bowing parameters, including now both the b_I and b_{II} contribution in Eq. (17), have been calculated based on SQS for a variety of III-V and II-VI ternary alloys with $x = 0.5$ using the linear augmented-plane-wave method.[230,233,234,236,237] The values are found in good agreement with the experimental bowing parameters listed in Table VII. Furthermore, a comparison with calculations assuming the CuPt-like ordering shows that the bowing parameters of the random alloys are significantly smaller than those of the ordered compounds.[233,234] A continuous decrease of the bandgap energy and thus a continuous increase of the bowing parameter with increasing degree of CuPt-like long-range order has also been observed for $In_{0.5}Ga_{0.5}P$, $In_{0.5}Al_{0.5}As$, and $Ga_{0.5}Al_{0.5}As$ in a number of

This article is copyrighted as indicated in the article. Reuse of AIP content is subject to the terms at: http://scitation.aip.org/termsconditions. Downloaded to IP: 131.169.38.71 On: Tue, 17 Nov 2015 09:25:17

other studies.[61–63,191,238,239] Short-range order such as local clustering also decreases and increases the bandgap energy and the bowing parameter, respectively, albeit not as strongly as observed for complete long-range order.[62,239]

Individual bowing contributions were calculated for random $In_{0.5}Ga_{0.5}As$, $Ga_{0.5}Al_{0.5}As$, and $GaAs_{0.5}P_{0.5}$ alloys using SQS and a first-principles self-consistent pseudopotential approach.[229,234] As expected, the contributions due to volume deformation and structural relaxation vanish for the lattice-matched alloy $Ga_{0.5}Al_{0.5}As$ and the calculated total bowing parameter of 0.2 eV arises solely from charge redistribution between the As anions and the two different cations. In contrast, the bowing contribution due to charge redistribution is negligible for the two lattice-mismatched alloys $In_{0.5}Ga_{0.5}As$ and $GaAs_{0.5}P_{0.5}$. For the latter, the calculated total bowing parameter of 0.19 eV stems almost equally from volume deformation and structural relaxation. For $In_{0.5}Ga_{0.5}As$ the dominant contribution due to volume deformation is slightly reduced by a small negative contribution due to structural relaxation yielding a calculated total bowing parameter of 0.40 eV. These values for the lattice-mismatched systems were obtained by averaging the three different energy levels at the valence band maximum which are degenerate in the zincblende structure but differ in the random alloy due to crystal-field splitting. Using the highest level as reference instead yields a bowing contribution due to structural relaxation twice as high as that arising from volume deformation for $GaAs_{0.5}P_{0.5}$ with a total b value of 0.34 eV. For $In_{0.5}Ga_{0.5}As$, the contribution due to volume deformation is still dominant but structural relaxation now gives a positive contribution to the bandgap bowing resulting in a total bowing parameter of 0.58 eV. This demonstrates that there is no clear trend in the significance of the different bowing contributions for these three ternary III-V alloys. Furthermore, the contribution arising from structural relaxation contains changes of the bandgap energy due to both a change in the first nearest neighbor bond lengths and the associated charge redistribution as already discussed above. An unambiguous distinction between structural and electronic effects on the bandgap bowing is thus not possible based on this three-step process. However, the two effects can indeed be estimated separately based on the atomic-scale structural parameters determined by EXAFS as discussed in Secs. III E 3 and III E 4 for the specific case of $In_xGa_{1-x}P$.[185]

For some materials, including $GaAs_xN_{1-x}$ and $ZnTe_xS_{1-x}$, very large and composition-dependent bowing parameters have been observed.[193,240] For example, the incorporation even of very small amounts of N into GaAs extremely reduces the bandgap energy although the bandgap of GaN is more than twice that of GaAs.[241] For these materials, two different compositional regions can therefore be distinguished: (i) a band-like region where the bowing parameter is relatively small and nearly constant and (ii) an impurity-like region where the bowing parameter is considerably larger and depends on the alloy composition.[193,240] In principle, this distinction can be made for all ternary III-V and II-VI alloys, however, for most materials with chemically similar elements populating the mixed sublattice, the compositional range of the impurity-like region is $0.99 \ll x \leq 1$ and hence negligibly small. For alloys where the elements occupying the mixed sublattice have very different properties, in contrast, the impurity-like region can span a considerable compositional range from $x = 1$ down to $x \sim 0.9 - 0.8$. A characteristic feature of these materials are strongly localized states introduced by the impurity atoms in the dilute limit which occur as either deep levels in the bandgap or as resonant states within the conduction band.[242] If these localized impurity states are close enough in energy to the conduction band minimum associated with the extended states of the host matrix, the resulting interaction leads to level repulsion and thus to a reduction of the bandgap energy.[242,243] This band anticrossing (BAC) model was used to reproduce successfully both the pressure and composition dependence of the energy levels in $GaAs_xN_{1-x}$,[243] $ZnTe_xS_{1-x}$,[242] and $ZnTe_xSe_{1-x}$[242] for compositions x down to ~0.85. The BAC model thus provides a good description of the extremely large and composition-dependent bowing parameters in the impurity-like region of these highly mismatched ternary III-V and II-VI alloys.

3. Volume deformation, charge redistribution, and structural relaxation

As already mentioned in Sec. III E 2, the bowing contributions arising from volume deformation, charge redistribution, and structural relaxation can have different signs and magnitudes for different semiconductor alloys. Furthermore, they arise from both the structural and electronic differences of the two parent compounds. These different aspects are now discussed in more detail for the specific example of $In_xGa_{1-x}P$ based on experimentally available parameters.[185] Figure 37 plots the bandgap bowing, ΔE_g, versus alloy composition x. Bowing parameters, b, determined experimentally range from 0.50 eV (Ref 198) to 0.76 eV (Refs. 33 and 200) and 0.79 eV (Ref. 199) resulting in an average value of 0.65 eV.[26,71] The corresponding energy differences ΔE_g at $x = 0.5$ range from approximately 0.12 to 0.20 eV.

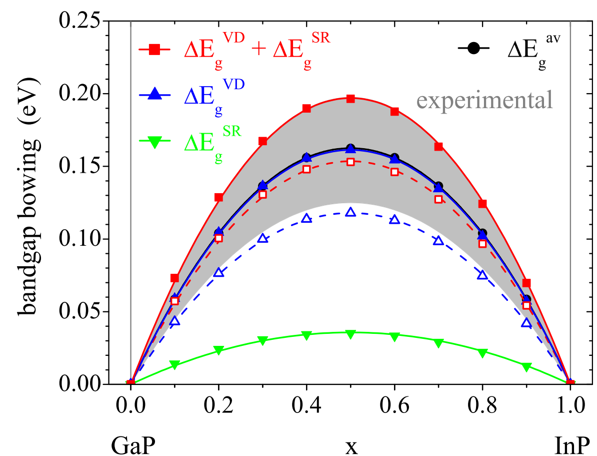

FIG. 37. Bowing of the lowest direct bandgap versus composition x for $In_xGa_{1-x}P$.[185] The shaded area denotes the range of experimental values reported in the literature[33,198–200] together with the average values given in Ref. 26 (black circles). The bowing contributions originating from volume deformation (blue up triangles) and structural relaxation (green down triangles) as well as their sum (red squares) are also plotted. Full and open symbols correspond to different sets of deformation potentials used for the calculations.

This article is copyrighted as indicated in the article. Reuse of AIP content is subject to the terms at: http://scitation.aip.org/termsconditions. Downloaded to IP: 131.169.38.71 On: Tue, 17 Nov 2015 09:25:17

Bowing parameters for random $In_xGa_{1-x}P$ alloys calculated theoretically with different methods and approaches range from $b = 0.40$ to 0.80 eV (Refs. 239, 62, 63 202, 220, and 233) corresponding to ΔE_g values of 0.1 to 0.2 eV at $x = 0.5$ in good agreement with the experimental values. Early works further differentiate between the bowing contribution for a fictitiously periodic alloy, b_I, and the bowing contribution due to disorder effects, b_{II}, (see Sec. III E 2).[202,220] The b_I values are 0.39 and 0.31 eV and thus similar for both works while the b_{II} values of 0.31 and 0.09 eV differ substantially. The only differentiation between bowing contributions due to volume deformation, charge redistribution and structural relaxation for $In_xGa_{1-x}P$ is reported for an ordered $In_{0.5}Ga_{0.5}P$ compound with chalcopyrite structure.[226] The calculated $b_I^{SR} = 0.17$ eV is of a similar order as the sum of b_I^{VD} and b_I^{CE} which equals 0.25 eV demonstrating the importance of structural relaxation in this material.

The bowing contribution ΔE_g^{VD} due to volume deformation can be calculated based on experimental values for the deformation potential γ of InP and GaP according to Eq. (19).[185] The lattice constant $a(x)$ is determined using Eq. (1) based on the fact that $In_xGa_{1-x}P$ was shown to closely follow Vegard's Law.[33,34] The results obtained with $\gamma_{InP} = -6.35$ eV (Ref. 244) and $\gamma_{GaP} = -8.83$ eV (Ref. 245) are plotted in Fig. 37 as full symbols while the values calculated with $\gamma_{InP} = -7.6$ eV (Ref. 70) and $\gamma_{GaP} = -9.3$ eV (Ref. 70) are shown as open symbols. Clearly, the choice of the deformation potentials noticeably affects the calculated ΔE_g^{VD}. In any case, however, volume deformation yields a strong positive bowing the magnitude of which is of a similar order as that of the total bowing observed experimentally.

The bowing contribution ΔE_g^{SR} due to structural relaxation can be calculated based on the displacement δ of the P anion and on the coefficient $d(\Delta E_g^{SR})/d\delta$ that describes the change in the bandgap energy arising from a certain anion displacement

$$\Delta E_g^{SR} = \frac{d\left(\Delta E_g^{SR}\right)}{d\delta}\ \delta. \tag{22}$$

For ordered $In_{0.5}Ga_{0.5}P$ with the chalcopyrite structure, each P atom has two In and two Ga first nearest neighbors corresponding to the $n = 2$ configuration (see Figs. 2(e) and 25(c)). For such an ordered compound, the displacement of the P atom from its ideal lattice site was calculated to be $\delta^{(2)} = 0.028$ (Ref. 226) in excellent agreement with the value $\delta^{(2)} = 0.029$ obtained with model 5 as described in Sec. III D (see Fig. 35).[185] Note that this displacement $\delta^{(2)}$ differs significantly from the average displacement $\langle\delta\rangle = 0.023$ also shown in Fig. 35 which clearly demonstrates once more the importance of differentiating between the local and the average structure of random ternary alloys. For the ordered $In_{0.5}Ga_{0.5}P$ compound with the chalcopyrite structure, the change in bandgap energy arising from the single anion displacement $\delta^{(2)} = 0.028$ was calculated to be $\Delta E_g^{SR} = 0.0425$ eV using a first-principles self-consistent band structure approach.[226] The corresponding coefficient $d(\Delta E_g^{SR})/d\delta^{(2)}$ thus equals 1.5 eV. First-principles self-consistent calculations of ordered $In_nGa_{4-n}P_4$ compounds with $n = 1$, 2, and 3 further resulted in similar total bowing parameters for all three compositions thereby suggesting that also the coefficients $d(\Delta E_g^{SR})/d\delta^{(n)}$ are similar in all three cases. A single coefficient $d(\Delta E_g^{SR})/d\delta = 1.5$ eV can hence be assumed independent of the local configuration and the bowing contribution ΔE_g^{SR} due to structural relaxation of the random alloy can be estimated as[185]

$$\Delta E_g^{SR} = \frac{d\left(\Delta E_g^{SR}\right)}{d\delta}\ \langle\delta\rangle. \tag{23}$$

The bowing contribution obtained with the $\langle\delta\rangle$ values from Fig. 35 is plotted in Fig. 37 together with ΔE_g^{VD} and the experimentally determined range for ΔE_g. Clearly, structural relaxation from the ideal zincblende geometry constitutes a positive and noticeable contribution to the bandgap bowing for this ternary alloy system even though it is significantly smaller than the contribution due to volume deformation.

At $x = 0.5$, ΔE_g^{SR} and ΔE_g^{VD} amount to 0.035 eV and 0.161 or 0.118 eV, respectively. These values are similar to those of 0.024 and 0.128 eV calculated for random $In_xGa_{1-x}As$ at $x = 0.5$ using a first-principles, self-consistent pseudopotential approach.[229] Furthermore, the sum $\Delta E_g^{SR} + \Delta E_g^{VD}$ is well within the range of experimentally observed ΔE_g values (see Fig. 37) indicating that the third contribution ΔE_g^{CE} is of minor importance for $In_xGa_{1-x}P$ alloys. This is again in good agreement with the value of $\Delta E_g^{CE} = -0.007$ eV calculated for random $In_xGa_{1-x}As$ at $x = 0.5$.[229] This clearly shows that no major change in the bandgap occurs due to charge redistribution when mixing the different cations at *equal* first nearest neighbor distances. However, as discussed above, both structural and electronic effects contribute to ΔE_g^{SR} and it is not clear whether charge redistribution does become important for *unequal* first nearest neighbor bond lengths. An unambiguous assignment of the effects due to changes of the first nearest neighbor structural environment and due to changes of the charge distribution is thus not possible based on this three step process.

4. Structural and electronic effects

In order to distinguish structural and electronic effects, a slightly different process has been proposed based on the transformation of the AC and BC parent compounds to the $A_xB_{1-x}C$ alloy via two subsequent steps.[185] (i) In the first step, the A-C and B-C *bonds* are compressed or dilated directly to the different individual first nearest neighbor distances found in the alloy at any given composition x. This yields a contribution ΔE_g^{struc} to the bandgap bowing which is caused solely by a *structural change* of the local atomic arrangements. (ii) In the second step, appropriate fractions of the different A-C and B-C bonds are mixed together allowing for a charge redistribution between the A, B, and C atoms while maintaining all first nearest neighbor distances at their values prepared in the first step. The resulting contribution ΔE_g^{elec} to the bandgap bowing thus arises solely from a change in the charge configuration and hence represents the *electronic effects* due to the different chemical properties

This article is copyrighted as indicated in the article. Reuse of AIP content is subject to the terms at: http://scitation.aip.org/termsconditions. Downloaded to IP: 131.169.38.71 On: Tue, 17 Nov 2015 09:25:17

of the atoms. The total bandgap bowing can then be written as the sum of the structural and electronic contributions

$$\Delta E_g = \Delta E_g^{struc} + \Delta E_g^{elec} \tag{24}$$

with the corresponding bowing parameter

$$b = b^{struc} + b^{elec}. \tag{25}$$

The structural contribution, ΔE_g^{struc}, is estimated based on model 5 described in Sec. III C 2 where the *individual* A-C and B-C distances are calculated for each of the five different first nearest neighbor configurations characterized by the number, n, of A atoms (see Fig. 25).[185] The energy differences that result from compressing or dilating the A-C and B-C bonds, respectively, are then given by

$$\begin{aligned} \Delta E_g^{A-C}(x) &= \sum_{n=0}^{4} P^{(n)}(x)\ \frac{n}{4}\ 3\gamma_A \ln\left[\frac{d_A^{bin}}{d_A^{(n)}(x)}\right], \\ \Delta E_g^{B-C}(x) &= \sum_{n=0}^{4} P^{(n)}(x)\ \frac{(4-n)}{4}\ 3\gamma_B \ln\left[\frac{d_B^{bin}}{d_B^{(n)}(x)}\right], \end{aligned} \tag{26}$$

where $P^{(n)}(x)$ represents the probability of finding a certain configuration at a given composition x and the sums run over all possible configurations. The individual A-C and B-C first nearest neighbor distances for each configuration are denoted by $d_A^{(n)}(x)$ and $d_B^{(n)}(x)$, respectively, whereas d_A^{bin} and d_B^{bin} stand for the bond lengths of the binary parent compounds. The factors $n/4$ and $(4-n)/4$ give the fraction of A-C and B-C bonds, respectively, in each of the five different configurations. The structural contribution, ΔE_g^{struc}, then follows as the sum of the two terms in Eq. (26), namely,

$$\Delta E_g^{struc}(x) = \Delta E_g^{A-C}(x) + \Delta E_g^{B-C}(x). \tag{27}$$

The results obtained for $In_xGa_{1-x}P$[185] are plotted as a function of composition x in Fig. 38 together with the experimentally determined ΔE_g values.[33,198–200] Similar to the calculation of ΔE_g^{VD} in Sec. III E 3, two sets of deformation potentials were used, namely, $\gamma_{InP} = -6.35$ eV (Ref. 244) and $\gamma_{GaP} = -8.83$ eV (Ref. 245) (full symbols), and $\gamma_{InP} = -7.6$ eV (Ref. 70) and $\gamma_{GaP} = -9.3$ eV (Ref. 70) (open symbols). In this case, however, the resulting differences are small and can be neglected. At $x = 0.5$, for example, ΔE_g^{struc} amounts to 0.067 or 0.059 eV, respectively. As apparent in Fig. 38, ΔE_g^{struc} represents a significant contribution to the bandgap bowing but fails to account for the full magnitude of ΔE_g. The remaining bandgap bowing corresponds to ΔE_g^{elec} which therefore also constitutes a significant contribution to ΔE_g. Consequently, structural and electronic effects both contribute to the bandgap change in a similar way and neither structural relaxation nor charge redistribution can be neglected.

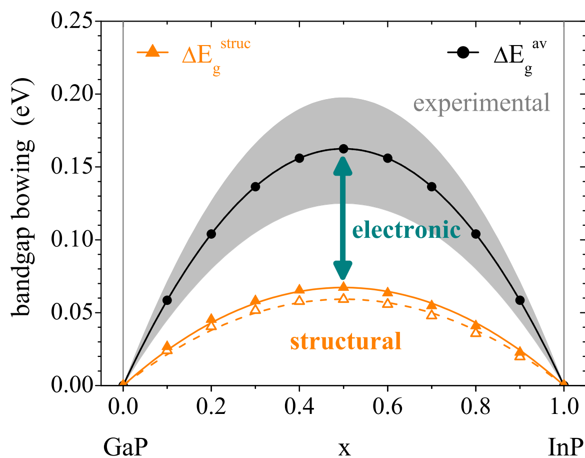

FIG. 38. Bowing of the lowest direct bandgap versus composition x for $In_xGa_{1-x}P$.[185] The shaded area denotes the range of experimental values reported in the literature[33,198–200] together with the average values given in Ref. 26 (black circles). The bowing contribution arising from structural effects is plotted as orange triangles while the remaining electronic contribution is indicated by the cyan arrow. Full and open symbols correspond to different sets of deformation potentials used for the calculations.

Comparing Figs. 37 and 38, it becomes clear that the purely structural contribution, ΔE_g^{struc}, to the bandgap bowing is much smaller than the contribution ΔE_g^{VD} due to volume deformation. Obviously, the latter strongly overestimates the change in the bandgap energy due to structural changes since it assumes that the element-specific bond lengths of the ternary alloy agree with the VCA prediction. In reality, however, the bond lengths are much closer to the values of the binary parent compounds than to the ones predicted by the VCA as discussed in detail in Sec. III A 1. In the three step process, this effect is taken into account by the bowing contribution ΔE_g^{SR} arising from structural relaxation in the ternary alloy. The *structural* contribution to ΔE_g^{SR} thus must be negative to compensate for the overestimation of the bond length changes made by ΔE_g^{VD}. In fact, the sum of ΔE_g^{VD} and this structural contribution of ΔE_g^{SR} is given precisely by the purely structural contribution, ΔE_g^{struc}.

As discussed in Sec. III E 3, ΔE_g^{CE} is small and charge redistribution at *equal* A-C and B-C bond lengths can be neglected for $In_xGa_{1-x}P$ and $In_xGa_{1-x}As$. In contrast, Fig. 38 very clearly shows that charge redistribution at *unequal* A-C and B-C bond lengths represents an important contribution to the bandgap bowing in $In_xGa_{1-x}P$. In the three step process, this effect is again taken into account by the bowing contribution originating from structural relaxation in the ternary alloy and ΔE_g^{elec} represents precisely the *electronic* contribution to ΔE_g^{SR}. In fact, it is only this strong electronic contribution that leads to an overall positive ΔE^{SR} as the structural contribution is negative as discussed above. Charge redistribution thus contributes significantly to the change in the bandgap energy but only in combination with the *unequal* first nearest neighbor distances in the random ternary alloy. These findings clearly highlight the strong influence of the atomic-scale structure of III-V and II-VI ternary alloys on important material properties most prominently the bandgap energy.[185]

IV. CHALCOPYRITE MATERIALS

The I-III-VI_2 ternary compounds and their quaternary alloys typically crystallize in the chalcopyrite structure shown in Figs. 2(e) and 2(f). They comprise a large material group that spans a wide parameter range similar to the

This article is copyrighted as indicated in the article. Reuse of AIP content is subject to the terms at: http://scitation.aip.org/termsconditions. Downloaded to IP: 131.169.38.71 On: Tue, 17 Nov 2015 09:25:17

zincblende materials discussed in Sec. III. This section, however, is focused on the two alloy systems $CuIn_xGa_{1-x}Se_2$ and $CuIn_xGa_{1-x}S_2$ for which detailed studies of the atomic-scale structure have been reported. Table VIII summarizes important structural parameters for the corresponding ternary parent compounds.[246–250] The a and c lattice constants range from 5.35 and 10.47 Å for $CuGaS_2$ to 5.78 and 11.62 for $CuInSe_2$. The tetragonal distortion, $\eta = c/2a$, is just below one for the Ga compounds while it is slightly larger than one for the In compounds. Similarly, the x coordinate of the anion is very close to the ideal value of 0.25 for both $CuGaS_2$ and $CuGaSe_2$, whereas it is notably smaller than 0.25 for $CuInS_2$ and $CuInSe_2$. The relationship between the anion position x and the two different bond lengths, d_{Cu} and d_{III}, is given by

$$d_{Cu} = a\sqrt{x^2 + \frac{(\eta^2+1)}{16}},\qquad d_{III} = a\sqrt{\left(x-\frac{1}{2}\right)^2 + \frac{(\eta^2+1)}{16}}, \tag{28}$$

and

$$x = \frac{1}{4} + \frac{d_{Cu}^2 - d_{III}^2}{a^2}. \tag{29}$$

For each of the two Ga compounds, the Cu-VI and Ga-VI bond lengths are very similar as can be seen from Table VIII corresponding to an anion displacement $u = 0.25 - x$ close to zero. In contrast, the Cu-VI bond length of the In compounds is significantly smaller than the In-VI bond length corresponding to u values of approximately 0.02 to 0.05. The anion is thus displaced away from the In atoms towards the Cu atoms when compared with the ideal tetrahedral site. All four materials are direct semiconductors with bandgap energies that range from approximately 1.0 eV for $CuInSe_2$ to about 2.4 eV for $CuGaS_2$. Table IX lists a range of values reported in the literature for the different ternary compounds.[37,38,44,251–257] The variation of the values is typically less than 10%.

TABLE VIII. Lattice constants, a and c, tetragonal distortion, $\eta = c/2a$, anion position, x, anion displacement, $u = 0.25 - x$, and first nearest neighbor bond lengths, d_{Cu} and d_{III}, at 300 K for the Cu-III-VI_2 chalcopyrites with III = Ga or In and VI = S or Se.

	a (Å)	c (Å)	η	x	u	d_{Cu} (Å)	d_{III} (Å)	Reference
$CuGaS_2$	5.349	10.47	0.979	0.25	0.00	2.300	2.300	246
	5.356	10.435	0.974	0.275	−0.025	2.380	2.224	247
	5.347	10.474	0.979	0.254	−0.004	2.312	2.287	248
$CuGaSe_2$	5.607	10.99	0.980	0.25	0.00	2.412	2.412	246
	5.614	11.03	0.982	0.25	0.00	2.417	2.417	247
	5.596	11.004	0.983	0.243	0.007	2.387	2.433	249
$CuInS_2$	5.517	11.06	1.002	0.20	0.05	2.243	2.560	246
	5.523	11.12	1.007	0.214	0.036	2.288	2.517	247
	5.523	11.133	1.008	0.229	0.021	2.333	2.466	248
$CuInSe_2$	5.773	11.55	1.000	0.22	0.03	2.404	2.604	246
	5.784	11.616	1.004	0.224	0.026	2.424	2.598	247
	5.782	11.62	1.005	0.235	0.015	2.459	2.559	250

TABLE IX. Bandgap energy, E_g, at 300 K for the Cu-III-VI_2 chalcopyrites with III = Ga or In and VI = S or Se.

Material	E_g (eV)	References
$CuGaS_2$	2.38	254
$CuGaSe_2$	1.63	252, 37, and 256
	1.66	38
	1.69	257
	1.70	255
$CuInS_2$	1.43	44
	1.44	251 and 254
	1.49	253
$CuInSe_2$	0.93	44
	0.96	253 and 37
	0.98	38
	0.99	251 and 252
	1.01	256
	1.03	257 and 255

The group-III cation-mixed alloys and the group-VI anion-mixed alloys also crystallize in the chalcopyrite structure over the whole compositional range. The lattice mismatch ranges from 3% to 6% and the lattice constants, a and c, were found to follow Vegard's Law for both $CuIn_xGa_{1-x}Se_2$[35–39] and $CuIn_xGa_{1-x}S_2$.[40–42] As an example, Fig. 39 plots a and c versus composition x for $CuIn_xGa_{1-x}Se_2$.[36,38] Clearly, both lattice constants change linearly with composition yet the slope of the two curves is distinctly different. The latter corresponds to the fact that the tetragonal distortion is smaller than one for $CuGaSe_2$ but larger than one for $CuInSe_2$. The ideal ratio of $c = 2a$ is observed for a composition $x \sim 0.8$. A similar behavior is found for $CuIn_xGa_{1-x}S_2$.[40–42] The anion-mixed system $CuIn(Se_xS_{1-x})_2$ also obeys Vegard's Law.[43–45] However, in this case a and $c/2$ exhibit nearly the same slope with composition x in agreement with the nearly identical η values of the two parent compounds (see Table VIII).

The bandgap energy changes continuously but nonlinearly with composition similar to that of the zincblende materials discussed in Sec. III E. Figure 40 plots the bandgap energy versus composition x for $CuIn_xGa_{1-x}Se_2$ as an

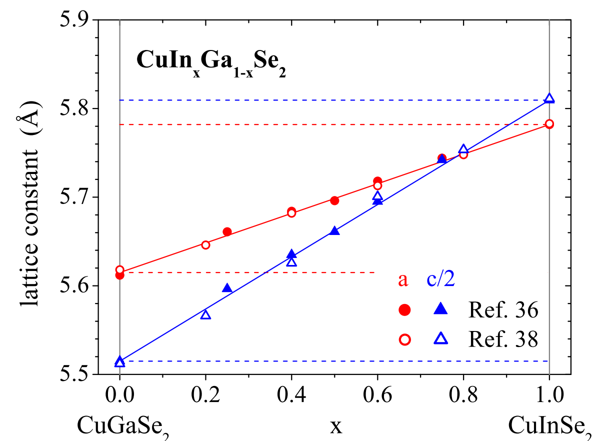

FIG. 39. Lattice constants, a (red circles) and $c/2$ (blue triangles), versus composition x for $CuIn_xGa_{1-x}Se_2$. The data are taken from Refs. 36 (full symbols) and 38 (open symbols). The dashed and solid lines represent the ternary values and Vegard's Law, respectively.

This article is copyrighted as indicated in the article. Reuse of AIP content is subject to the terms at: http://scitation.aip.org/termsconditions. Downloaded to IP: 131.169.38.71 On: Tue, 17 Nov 2015 09:25:17

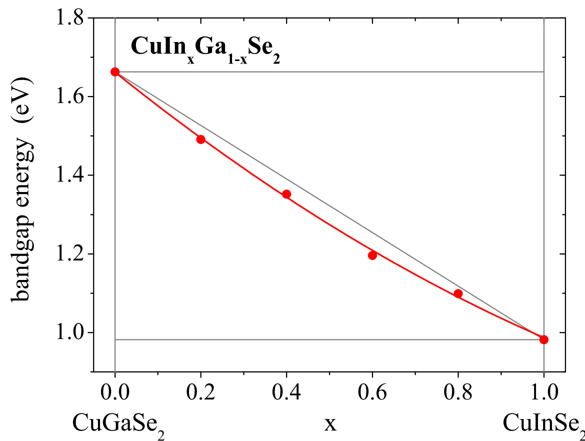

FIG. 40. Bandgap energy versus composition x for the direct semiconductor $CuIn_xGa_{1-x}Se_2$.[38] The solid line corresponds to a quadratic dependence as given by Eq. (2) with a bowing parameter of $b = 0.20$ eV. The thin gray lines represent the ternary values and their weighted average.

example.[38] As can be seen, the experimental values are well described by Eq. (2) and a bowing parameter, b, of 0.20 eV. Other studies report b values between 0.15 and 0.26 eV.[37,252,256,257] The bandgap energy of $CuIn_xGa_{1-x}S_2$ also follows a quadratic dependence with composition x and bowing parameters of 0.20 and 0.31 eV were reported.[254,258] In contrast, the anion-mixed alloys $CuGa(Se_xS_{1-x})_2$ and $CuIn(Se_xS_{1-x})_2$ exhibit a practically linear change in the bandgap energy with composition x and the bowing parameter is identical or close to zero.[44,251,253,258,259] The b values for all four quaternary alloys are summarized in Table X.

It is interesting to note that the bowing for the cation-mixed chalcopyrite alloys equals only one-third to one-half of that observed in cation-mixed III-V ternary alloys with III = In and Ga such as $In_xGa_{1-x}P$ and $In_xGa_{1-x}As$ (see Table VII). Intuitively, this can be understood by the fact that only half of the cations are affected by the alloying in the chalcopyrite structure.[237,260] In contrast, the much smaller bowing of the anion-mixed chalcopyrite alloys compared to the anion-mixed II-VI ternary alloys with VI = Se and S such as $ZnSe_xS_{1-x}$ (see Table VII) originates from the stronger coupling of the anion p states and the Cu d states in the chalcopyrites.[237] This reduces the valence band offset between the parent compounds and hence part of the

TABLE X. Bowing parameter, b, at 300 K for Cu-III-VI$_2$ quaternary chalcopyrite alloys with III = Ga or In and VI = S or Se.

Material	b	References
$CuIn_xGa_{1-x}S_2$	0.20	254
	0.31	258
$CuIn_xGa_{1-x}Se_2$	0.15	252 and 37
	0.18	256
	0.20	38
	0.26	257
$CuGa(Se_xS_{1-x})_2$	−0.01	259
	0.00	258
$CuIn(Se_xS_{1-x})_2$	0.00	251 and 44
	0.02	253

disparity which causes the bandgap bowing. Independent of these differences, however, the bandgap energy of the chalcopyrite alloys changes continuously with composition x similar to that of the zincblende alloys. Therefore, it can be tuned in much the same way by adjusting, for example, the In to Ga ratio. This allows the controlled tailoring of important material properties such as the bandgap in order to optimize device performance, in particular, the conversion efficiency in thin film solar cells.

A. Atomic-scale structure

Studies of the atomic-scale structure of quaternary chalcopyrite alloys using EXAFS were reported for $CuIn_xGa_{1-x}Se_2$[35,261–263] and $CuIn_xGa_{1-x}S_2$.[262] In these materials, each cation is bonded to four Se or S anions while each anion has two Cu and two group-III first nearest neighbors as shown in Figs. 2(e) and 2(f). The group-III lattice site is populated by In and Ga atoms leading to a total of three different bonds, namely, Cu-Se, Ga-Se, and In-Se or Cu-S, Ga-S, and In-S for $CuIn_xGa_{1-x}Se_2$ or $CuIn_xGa_{1-x}S_2$, respectively. As can be seen from Table VIII, the Cu-VI bond lengths are similar in the pure Ga and pure In compound for a given anion species and therefore little change is expected for the Cu-VI bond length of the corresponding cation-mixed alloys. In contrast, the In-VI and Ga-VI bond lengths of the ternary compounds with a common anion strongly differ from each other corresponding to the significant differences in both lattice constants and anion position. Based on Vegard's Law and the VCA, the In-VI and Ga-VI bond lengths of the corresponding cation-mixed alloys should be equal and change linearly with composition x between the values of the two ternary parent compounds.

Figure 41 plots the element-specific Cu-Se, Ga-Se, and In-Se bond lengths measured with EXAFS for $CuIn_xGa_{1-x}Se_2$ as a function of composition x.[261,263] The

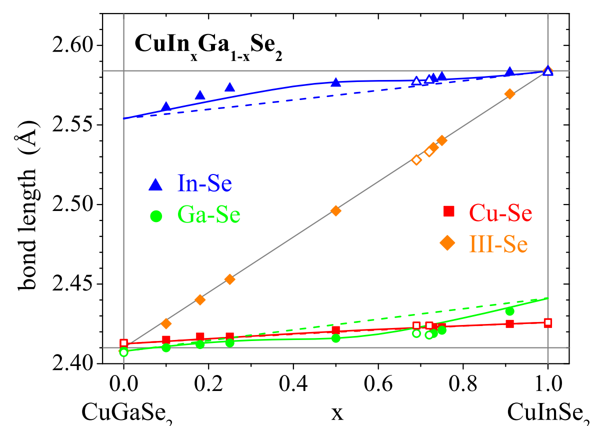

FIG. 41. Element-specific In-Se (blue triangles), Ga-Se (green circles), and Cu-Se (red squares) bond lengths as a function of composition x for $CuIn_xGa_{1-x}Se_2$.[261–263] Full and open symbols correspond to powder samples and polycrystalline thin films, respectively. The uncertainty of the values is ±0.002 Å and thus similar to the size of the symbols. The solid and dashed lines show the bond lengths calculated with a VFF model (model 5, see Sec. III C 2) based on a distribution of the different cation configurations according to the law of mass action and to a random distribution, respectively. The thin gray lines represent the binary values and the ones predicted by the VCA.

This article is copyrighted as indicated in the article. Reuse of AIP content is subject to the terms at: http://scitation.aip.org/termsconditions. Downloaded to IP: 131.169.38.71 On: Tue, 17 Nov 2015 09:25:17

values for the ternary parent compounds agree well with those listed in Table VIII obtained from diffraction measurements and with those reported for other EXAFS studies of $CuGaSe_2$,[264] $CuInSe_2$,[265–267] and $CuIn_xGa_{1-x}Se_2$.[35] Regarding the $CuIn_xGa_{1-x}Se_2$ alloy, the Cu-Se bond length changes almost linearly between the values of the ternary parent compounds as expected from the VCA. In contrast, the In-Se and Ga-Se bond lengths are very different from each other and remain nearly constant over the whole compositional range. In particular, they are much closer to the values of the ternary parent compounds than to the ones predicted by the VCA. Nevertheless, their weighted average agrees well with the VCA prediction in perfect accord with diffraction studies which measure the average III-Se bond length.[261] A very similar behavior was also found for $CuIn_xGa_{1-x}S_2$.[262] The mixed lattice site of these chalcopyrite alloys thus clearly exhibits a bimodal bond length distribution very similar to that observed for ternary zincblende alloys as discussed in Sec. III. Furthermore, the lattice mismatch between the parent compounds is again accommodated mostly by bond bending and only to a small extent by bond stretching. Consequently, the short-range atomic arrangements show a striking deviation from the average long-range crystallographic structure in both ternary zincblende and quaternary chalcopyrite alloys.

Closer examination of the $CuIn_xGa_{1-x}Se_2$ bond lengths also reveals some slight differences between chalcopyrite and zincblende alloys. For the latter, a small *linear* change in the element-specific bond lengths was observed in nearly all cases amounting to roughly 20% of the change predicted by the VCA (see Sec. III A). In contrast, the In-Se and Ga-Se bond lengths of $CuIn_xGa_{1-x}Se_2$ plotted in Fig. 41 exhibit a clearly *nonlinear* dependence on the composition x. For $x < 0.7-0.8$, the Ga-Se bond length changes linearly with composition but the change amounts to only 10% of that expected from the VCA. For $x > 0.7-0.8$, the slope of the curve noticeably increases such that the change in the Ga-Se bond length in the dilute limit corresponds to roughly 20% of the difference between the ternary Ga-Se and In-Se bond lengths. Similarly, the In-Se bond length changes by about 10% of the difference expected from the VCA for $x > 0.2-0.3$. For smaller In contents, the slope increases leading once more to an impurity bond length that differs from the bond length of the ternary parent compound by approximately 20% of the difference between the two ternary values. This behavior seems to be independent of the preparation conditions as it is observed for both powder samples and polycrystalline thin films (see Fig. 41).[263] A similarly nonlinear behavior was also observed for the Ga-S and In-S bond lengths of $CuIn_xGa_{1-x}S_2$.[262] The amount of bond length relaxation in the dilute limit is thus nearly identical for zincblende and chalcopyrite semiconductor alloys. This confirms the fundamental nature of the energetic balance between bond stretching and bond bending in tetrahedrally coordinated materials of the adamantine structural family. At the same time, the nonlinear change in the element-specific bond lengths, which is not observed for the zincblende alloys, points out additional effects caused by the increased complexity of the chalcopyrite structure.

Similar to the zincblende alloys, the atomic-scale structure of $CuIn_xGa_{1-x}Se_2$ and $CuIn_xGa_{1-x}S_2$ can be modeled using a VFF approach (see Sec. III B 1). In principle, the Keating potential for the chalcopyrite structure contains two different bond stretching force constants, α, and five different bond bending force constants, β.[147,149] However, the model is typically simplified using only one bond stretching and one bond bending force constant for each of the two different bonds. These force constants were determined from infrared and Raman spectroscopy measurements and are summarized in Table XI.[148,149,151] The Cu-VI bond stretching force constant is very similar for all four materials and varies between 25 and 30 N/m. The III-VI bond stretching force constants are roughly twice as high and vary between 40 and 60 N/m. Hence, the Cu-VI bond is much softer than the III-VI bond in accordance with the higher ionicity of the former compared to the latter.[268] Comparing α values from the same studies, it becomes clear that the In-VI bond stretching force constant is slightly smaller than the Ga-VI bond stretching force constant for any given anion. Furthermore, α is slightly smaller for the III-Se bond than for the III-S bond for both In and Ga. The bond stretching force constants thus decrease with increasing lattice constants and increasing bond lengths[149,150,269] very similar to what was observed for the III-V and II-VI zincblende compounds.[141,145,146] The absolute α values for the III-VI bond of the chalcopyrite compounds are, however, somewhat larger than those of comparable zincblende materials (see Table III). The values of the bond bending force constants listed for the chalcopyrite compounds in Table XI vary considerably for the different studies but are typically one tenth or less of the corresponding bond stretching force constant. Bond stretching thus requires significantly more energy than bond bending and the lattice mismatch in both zincblende and chalcopyrite semiconductor alloys is accommodated by bond angle relaxation rather than bond length relaxation.

Effective bond stretching force constants, $k_{||}$, for the Cu-Se and III-Se bonds of $CuInSe_2$ and $CuGaSe_2$ were also determined with temperature-dependent EXAFS measurements as described in Sec. III B 2 and are listed in Table XII.[265,270,271] Similar to what was observed for the zincblende materials, the $k_{||}$ values are similar to or slightly smaller than the α values

TABLE XI. Bond stretching force constant, α, and bond bending force constant, β, of the Keating VFF potential for the two different bonds of the Cu-III-VI_2 chalcopyrites with III = Ga or In and VI = S or Se obtained from phonon frequencies measured by infrared and Raman spectroscopy.

	α (N/m)		β (N/m)		
Material	Cu-VI	III-VI	Cu-VI	III-VI	Reference
$CuGaS_2$	25.0	50.8	2.0	6.0	148
	32.4	58.4	0	0	149
$CuGaSe_2$	24.7	47.8	0	0	149
	26.5	45.7	0.4	3.6	151
$CuInS_2$	25.1	41.2	2.0	4.0	148
	28.1	53.1	0	0	149
$CuInSe_2$	25.8	44.7	0	0	149
	25.3	41.9	2.3	1.3	151

This article is copyrighted as indicated in the article. Reuse of AIP content is subject to the terms at: http://scitation.aip.org/termsconditions. Downloaded to IP: 131.169.38.71 On: Tue, 17 Nov 2015 09:25:17

TABLE XII. Effective bond stretching force constant, $k_{||}$, determined from temperature-dependent EXAFS measurements for the ternary chalcopyrite compounds $CuGaSe_2$ and $CuInSe_2$.

Material	$k_{\|\|}$ (N/m) Cu-Se	III-Se	Reference
$CuGaSe_2$	96	126	270
$CuInSe_2$	63	107	265
	80		271

listed in Table XII multiplied with a factor of 3. In particular, the force constants of the Cu-Se bond are again significantly smaller than those of the III-Se bond while the force constant of the Ga-Se bond is only slightly higher than that of the In-Se bond.

The atomic-scale structure of $CuIn_xGa_{1-x}Se_2$ and $CuIn_xGa_{1-x}S_2$ was modeled based on the VFF approach of model 5 described in detail in Sec. III C 2.[261,262] Within this approach, the first step consists of calculating the *individual* element-specific first nearest neighbor distances for each local atomic configuration present in the alloy system. In the second step, the *average* element-specific bond lengths are determined as the weighted average of the corresponding individual first nearest neighbor distances. In the chalcopyrite structure of the Cu-III-VI_2 compounds, each anion is bonded to two Cu and two group-III first nearest neighbors. For the cation-mixed alloys $CuIn_xGa_{1-x}Se_2$ and $CuIn_xGa_{1-x}S_2$, this leads to three possible cation configurations surrounding the Se or S anions as shown schematically in Fig. 42. The different configurations are characterized by the number, n, of In atoms and are two Cu and two Ga atoms ($n=0$), two Cu, one Ga, and one In atom ($n=1$) and two Cu and two In atoms ($n=2$). The different first nearest neighbor distances for each configuration are calculated by minimizing the sum of the bond stretching energies of all four bonds assuming that the cations occupy the ideal lattice sites given by the VCA and Vegard's Law.[261] Neglecting the distortion energy caused by bond bending is reasonable given that the bond bending force constants are approximately one order of magnitude smaller than the corresponding bond stretching force constants (see Table XI). Moreover, including neither bond bending nor cation relaxation yields better results than including only one of the two effects as discussed in Sec. III C.

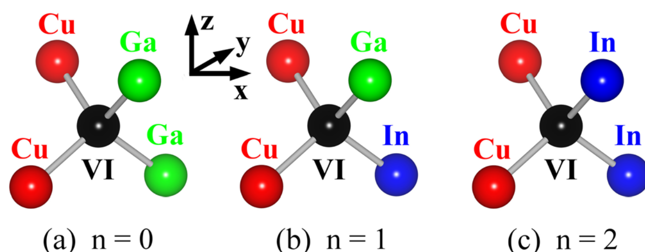

FIG. 42. Different first nearest neighbor cation configurations surrounding the central group-VI Se or S anion (black) in $CuIn_xGa_{1-x}Se_2$ or $CuIn_xGa_{1-x}S_2$ with chalcopyrite structure. The anions always have two Cu (red) and two group-III first nearest neighbors such that the number, n, of In atoms (blue) can be 0, 1, or 2 while the number of Ga atoms (green) is given by $2-n$. Images created with VESTA.[29]

Assuming a perfectly random distribution of the In and Ga atoms on the group-III lattice site, the probabilities $P^{(n)}(x)$ for the different cation configurations at any composition x are given by the binomial distribution (Bernoulli distribution)

$$\begin{aligned} P^{(0)}(x) &= (1-x)^2, \\ P^{(1)}(x) &= 2x(1-x), \\ P^{(2)}(x) &= x^2. \end{aligned} \tag{30}$$

The resulting *average* element-specific bond lengths are plotted as dashed lines in Fig. 41 for $CuIn_xGa_{1-x}Se_2$.[262] Clearly, the overall trend of the experimental values is well reproduced by the model calculation. In particular, the relaxation of the In-Se and Ga-Se bond lengths in the dilute limit are predicted quite accurately. For the Cu-Se bond length, excellent agreement between calculated and measured values is also observed for intermediate compositions while some notable differences are visible for the In-Se and Ga-Se bonds. The model calculation yields a linear increase of the element-specific bond lengths similar to the case of the zincblende alloys (see Sec. III C 2). The measured In-Se and Ga-Se bond lengths of the chalcopyrite $CuIn_xGa_{1-x}Se_2$ alloy, however, exhibit a nonlinear increase with increasing composition x as discussed above. These differences between measured and calculated bond lengths could originate from either cation relaxations or charge redistributions both of which are neglected in this simple VFF approach. Alternatively, deviations from a fully random distribution of the Ga and In atoms on the group-III lattice sites also yield differences between the experimental and theoretical bond lengths and can explain the observed discrepancy.

To study the effect of the cation distribution in more detail, the frequency of occurrence of each cation configuration shown in Fig. 42 was determined from the calculated individual first nearest neighbor distances and the measured average Ga-Se and In-Se bond lengths. The results for the mixed configuration with $n=1$ are shown in Fig. 43 for $CuIn_xGa_{1-x}Se_2$ together with the probability $P^{(1)}$ of the binomial distribution plotted as dashed line.[262] Obviously, the mixed configuration occurs significantly more often than expected for a strictly random distribution of the In and Ga atoms. The pure In ($n=2$) and pure Ga ($n=0$) configurations consequently occur less often than for a binomial distribution. This is in contrast to the demixing predicted by theoretical Monte Carlo calculations[272] but can be explained by the distortion energy, $E^{(n)}(x)$, associated with the different configurations. For lattice constants according to Vegard's Law, the calculated strain energy is smaller for two mixed configurations than for one In and one Ga configuration over the whole compositional range

$$2E^{(1)}(x) < E^{(0)}(x) + E^{(2)}(x). \tag{31}$$

Energy minimization would thus lead to the maximum number of mixed configurations possible for a given composition x as plotted by the dotted line in Fig. 43. In reality, the frequency of occurrence of the mixed configuration is determined by a competition between energy minimization on the

This article is copyrighted as indicated in the article. Reuse of AIP content is subject to the terms at: http://scitation.aip.org/termsconditions. Downloaded to IP: 131.169.38.71 On: Tue, 17 Nov 2015 09:25:17

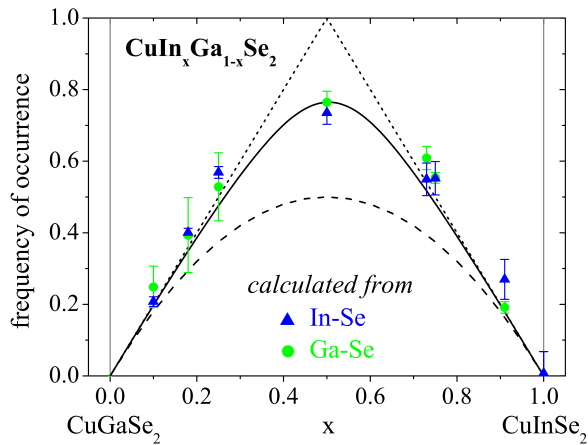

FIG. 43. Frequency of occurrence of the mixed cation configuration ($n=1$) as a function of composition x for $CuIn_xGa_{1-x}Se_2$ calculated from the In-Se (blue triangles) and Ga-Se (green circles) bond length.[262] The solid line represents the best fit based on the law of mass action while the dashed and dotted lines show the maximum entropy (random distribution) and minimum energy limits, respectively.

one hand and entropy maximization on the other hand with the latter corresponding to a strictly random distribution of the In and Ga atoms. This competition can be modeled by a law of mass action approach with an equilibrium temperature as only free parameter yielding good fits to the experimentally determined frequency for both $CuIn_xGa_{1-x}Se_2$ and $CuIn_xGa_{1-x}S_2$.[262] The resulting fit for $CuIn_xGa_{1-x}Se_2$ is shown by the solid line in Fig. 43.

The average In-Se, Ga-Se and Cu-Se bond lengths corresponding to this distribution of cation configurations are given as solid lines in Fig. 41. They clearly provide a much closer representation of the experimental values than the calculation based on a strictly random distribution of In and Ga atoms. In particular, they capture most of the nonlinearity observed in the increase of the In-Se and Ga-Se first nearest neighbor distances. The agreement between calculated and measured bond lengths is thus significantly improved just by assuming a not fully random distribution of the In and Ga atoms on the mixed group-III lattice site. Furthermore, this distribution of the different first nearest neighbor cation configurations is determined by the competition between energy minimization on the one hand and entropy maximization on the other hand.

B. Anion displacement

As discussed above, the anions are located close to the ideal tetrahedral lattice site for $CuGaSe_2$ and $CuGaS_2$ while they are significantly displaced along the x-direction for $CuInSe_2$ and $CuInS_2$ (see Table VIII). The anion displacement $u = 0.25 - x$ due to the different properties of the Cu and group-III atoms is thus nearly zero for the Ga compounds and ranges from approximately 0.02 to 0.05 for the In compounds. The anion displacements in the quaternary $CuIn_xGa_{1-x}Se_2$ and $CuIn_xGa_{1-x}S_2$ alloys can be studied based on the minimum-energy positions calculated with the VFF approach described in Sec. IV A (see also model 5 in Sec. III C 2).[261,262] Figure 44(a) plots the calculated u values versus composition x for the three different cation configurations shown in Fig. 42 for the case of $CuIn_xGa_{1-x}Se_2$. Clearly, the anion displacement strongly depends on the kind of first nearest neighbors being smallest for $n=0$, intermediate for $n=1$ and largest for $n=2$. As a consequence, there is no single u value for the alloy system and the material is characterized by the presence of different anion positions in the x-direction.

The individual u values for each configuration decrease with increasing composition x because the softer Cu-Se bonds expand proportionally more than the stiffer III-Se bonds for the given increase of the lattice constants according to Vegard's Law. In contrast, the weighted average $\langle u \rangle$ shown in Fig. 44(c) increases monotonically from approximately zero for $CuGaSe_2$ to almost 0.024 for $CuInSe_2$ in excellent agreement with diffraction studies that measure the average long-range crystallographic structure. Interestingly, the dependence is slightly nonlinear as can be seen by the nonlinear contribution $\langle u \rangle_{nl}$ shown in Fig. 44(c) multiplied by a factor of ten. Furthermore, neither $\langle u \rangle$ nor $\langle u \rangle_{nl}$ are

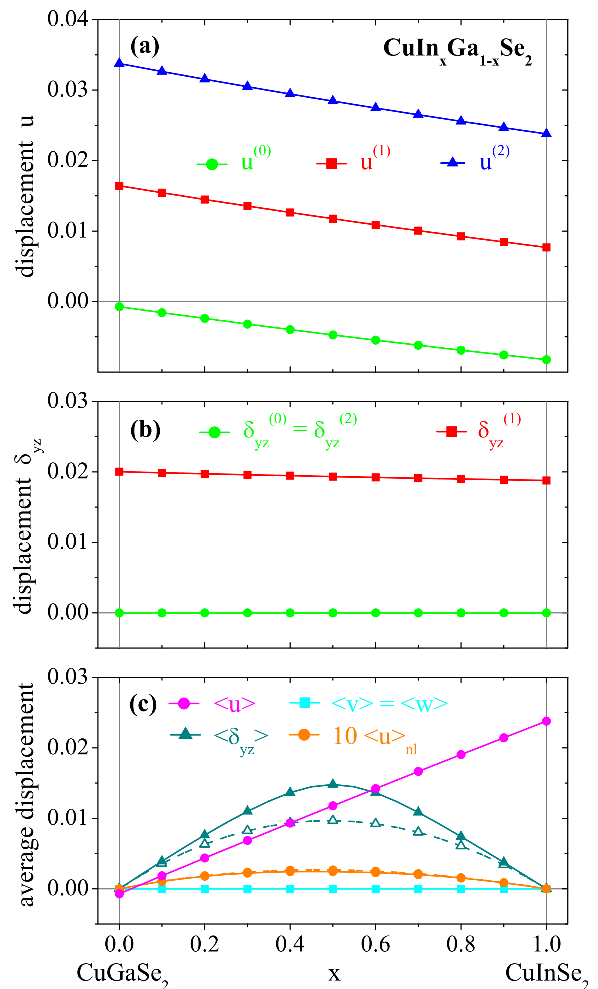

FIG. 44. (a) Displacement u of the Se anions with respect to Cu and group-III atoms and (b) displacement δ_{yz} of the Se anions with respect to In and Ga atoms as a function of composition x for $CuIn_xGa_{1-x}Se_2$. The displacements are plotted for each of the three different cation configurations with $n=0$, $n=1$, and $n=2$ denoting the number of In first nearest neighbors (see Fig. 42). The average displacements $\langle u \rangle$, $\langle v \rangle$, $\langle w \rangle$, and $\langle \delta_{yz} \rangle$ are shown in panel (c) together with the nonlinear contribution $\langle u \rangle_{nl}$ of $\langle u \rangle$ multiplied by a factor of 10. The full and open symbols in panel (c) correspond to a distribution of the different cation configurations according to the law of mass action and to a random distribution, respectively (see Fig. 43).

This article is copyrighted as indicated in the article. Reuse of AIP content is subject to the terms at: http://scitation.aip.org/termsconditions. Downloaded to IP: 131.169.38.71 On: Tue, 17 Nov 2015 09:25:17

notably affected by the distribution of the different cation configurations yielding similar values for both a frequency of occurrence according to the law of mass action and according to a random distribution of the In and Ga atoms (see Fig. 43).

Similarly to what has been discussed for the zincblende alloys in Sec. III D, the anions in $CuIn_xGa_{1-x}Se_2$ and $CuIn_xGa_{1-x}S_2$ are also displaced from their ideal tetrahedral lattice site due to the different properties of the In and Ga atoms.[261] Obviously, this effect is only present for the mixed cation configuration with $n=1$ and the displacement occurs in the y-z-plane perpendicular to the x-direction (see Fig. 42). In particular, $v=-w$ with $v=0.25-y$, $w=2\eta(0.125-z)\sim 2(0.125-z)$ and v either positive or negative depending on which of the two group-III atoms is the In atom. Figure 44(b) plots the calculated overall displacement, $\delta_{yz}=\sqrt{v^2+w^2}$, in the y-z-plane versus composition x for $CuIn_xGa_{1-x}Se_2$. For $n=0$ and $n=2$, δ_{yz} equals zero as expected from the symmetry of the corresponding cation configurations. For $n=1$, δ_{yz} amounts to approximately 0.02 over the whole compositional range. Each of the two group-III atoms of the mixed configuration can be the In atom with the same probability. The average values $\langle v\rangle$ and $\langle w\rangle$ therefore equal zero as indeed observed with diffraction measurements. The average displacement $\langle\delta_{yz}\rangle$, in contrast, does not vanish as shown in Fig. 44(c). It is zero only for the ternary parent compounds and shows a strong positive bowing for the alloy system reaching its maximum value at $x=0.5$. This behavior is very similar to the displacement of the atoms occupying the common sublattice in ternary zincblende alloys discussed in detail in Sec. III D. However, for the chalcopyrite alloys, the magnitude of $\langle\delta_{yz}\rangle$ clearly depends on the frequency of occurrence of the mixed configuration and thus on the In and Ga distribution as shown in Fig. 44(c). A similar behavior is observed for $CuIn_xGa_{1-x}S_2$.[262]

The atoms of the common sublattice thus exhibit substantial displacements from their ideal tetrahedral lattice site for both ternary zincblende alloys and quaternary chalcopyrite alloys. The local atomic arrangements therefore deviate significantly from the long-range crystallographic structure. Furthermore, direction and magnitude of the displacement strongly depend on the nature of the first nearest neighbor atoms and both zincblende and chalcopyrite alloys are characterized by structural inhomogeneity on the subnanometer scale. However, due to the increased complexity of the chalcopyrite structure compared to the zincblende structure, two different displacement mechanisms have to be distinguished for the cation-mixed Cu-III-VI_2 alloys. (i) The displacement of the anion with respect to Cu and group-III atoms represents a feature inherent to the chalcopyrite structure while (ii) the displacement of the anion with respect to In and Ga atoms is characteristic for the mixed occupation of the group-III lattice site in the alloy system. Both effects show a nonlinear dependence on the composition x and thus contribute to the bandgap bowing as discussed in Sec. IV C.

C. Bandgap bowing

The presence of two different types of cations in the chalcopyrite structure also affects the electronic properties of the Cu-III-VI_2 compounds and their quaternary alloys. The Cu d states, in particular, strongly influence the band structure of the material due to their high energy levels and non-localized nature.[273] As a result, the chalcopyrite compounds feature significantly reduced bandgap energies, spin-orbit splittings, valence band offsets, and pressure coefficients compared to the corresponding II-VI or III-V zincblende semiconductors.[237,274–277] Among these effects, the bandgap reduction is the most prominent and was even termed *bandgap anomaly*. Comparing, for example, the bandgap energies of $CuGaSe_2$ (Table IX) and its binary analogue ZnSe (Table I), a difference of approximately 1 eV is observed. Theoretical studies revealed that this bandgap reduction originates from three different effects the first two of which are of a chemical nature while the third represents a structural effect.[274,276] (i) Hybridization of the Cu d states and the anion p states in the valence band leads to level repulsion and an upward shift of the valence band maximum. The resulting reduction of the bandgap energy amounts to about 0.7 eV for $CuInSe_2$. (ii) The different cation electronegativities lead to a charge redistribution between the Cu and group-III atoms which leads to a small decrease of the bandgap energy by 0.1–0.2 eV. (iii) The displacement of the anion away from its ideal tetrahedral site towards lower x coordinates increases and decreases the energy of the valence and conduction band states, respectively. For $CuInSe_2$, this leads to a reduction of the bandgap energy by approximately 0.5 eV. The anion displacement and the p-d-repulsion are thus the dominant sources for the bandgap reduction observed in ternary chalcopyrite compounds when compared to their binary II-VI analogues with zincblende structure.

The influence of charge redistribution and atomic displacements on the bandgap energy in chalcopyrite compounds is, in principle, similar to that observed for III-V and II-VI ternary alloys as discussed in Sec. III E. Displacements of the P anions in ordered $In_{0.5}Ga_{0.5}P$ with the chalcopyrite structure, for example, significantly affect the bandgap energy with a corresponding coefficient of $d(\Delta E_g)/du=1.5$ eV.[226] As demonstrated in detail in Sec. III E 3, this also leads to a significant contribution to the bandgap bowing observed for random $In_xGa_{1-x}P$ alloys. The main difference between these structural effects in ternary zincblende alloys and Cu-III-VI_2 chalcopyrite compounds is the magnitude by which a certain anion displacement affects the bandgap energy. Depending on the method of calculation, coefficients $d(\Delta E_g)/du$ of approximately 12 to 32 eV were predicted for $CuInSe_2$.[274,276–278] These values are one order of magnitude larger than the corresponding coefficient for $In_{0.5}Ga_{0.5}P$ due to the fact that the electronegativity difference between Cu and In is nearly twice as high as that between In and Ga.[68,276] Regarding the cation-mixed Cu-III-VI_2 quaternary alloys, it was shown in Sec. IV B that a displacement of the anions occurs with respect to both the Cu and group-III atoms and the In and Ga atoms. Consequently, both displacement mechanisms have to be taken into account when studying the influence of the atomic-scale structure on the alloy bandgap.

Bandgap energies, E_g, are listed in Table IX for the Cu-III-VI_2 compounds with III = In or Ga and VI = Se or S

This article is copyrighted as indicated in the article. Reuse of AIP content is subject to the terms at: http://scitation.aip.org/termsconditions. Downloaded to IP: 131.169.38.71 On: Tue, 17 Nov 2015 09:25:17

while the bowing parameters, b, of the corresponding cation-mixed and anion-mixed alloys are summarized in Table X. In a simple phenomenological model, it was proposed that b is directly proportional to the difference in electronegativity of the two atoms occupying the mixed lattice site with a proportionality factor of 1.25.[279] While this approach yields reasonable agreement for the cation-mixed alloys listed in Table X, it fails for other chalcopyrite alloys and therefore does not provide a generally valid description of the bowing parameter.[237] Bandgap energies for the Cu-III-VI_2 quaternary alloys with III = In or Ga and VI = Se or S were also calculated using a modified bond charge model.[280,281] The resulting b values amount to 0.07 and 0.09 eV for $CuIn_xGa_{1-x}Se_2$ and $CuIn_xGa_{1-x}S_2$, respectively, while bowing parameters of 0.09 and −0.07 are obtained for $CuIn(Se_xS_{1-x})_2$ and $CuGa(Se_xS_{1-x})_2$, respectively. The model thus significantly underestimates the bandgap bowing of the cation-mixed alloys and of $CuGa(Se_xS_{1-x})_2$ while it overestimates b for $CuIn(Se_xS_{1-x})_2$ when compared to the experimental values given in Table X.

First-principles band structure calculations of different Cu-III-VI_2 quaternary alloys with III = In or Ga and VI = Se or S were performed applying special quasi-random structures already discussed in Sec. III E 2.[237,282] The bowing parameters thus obtained equal 0.21 eV for $CuIn_xGa_{1-x}Se_2$ (Ref. 237) and 0.04 eV for $CuIn(Se_xS_{1-x})_2$ (Ref. 237) in good agreement with the values listed in Table X, whereas the bowing parameter of 0.07 eV for $CuGa(Se_xS_{1-x})_2$ (Ref. 282) is notably larger than the experimental ones. For the III-V and II-VI ternary alloys with zincblende structure, the total bowing parameter b was decomposed into separate contributions arising from different physical effects, namely, volume deformation, charge redistribution, and structural relaxation (see Sec. III E 2). Unfortunately, no such decomposition is reported for the calculations of the bandgap bowing in quaternary chalcopyrite alloys.

However, the bowing contribution due to structural relaxation can be estimated based on the element-specific bond lengths and the corresponding atomic displacements as described in Sec. III E 3 for $In_xGa_{1-x}P$. For the $CuIn_xGa_{1-x}Se_2$ and $CuIn_xGa_{1-x}S_2$ chalcopyrite alloys, though, the two different displacement mechanisms discussed in Sec. IV B have to be distinguished.[261,262] For structural relaxation of the anion with respect to Cu and group−III atoms, coefficients $d(\Delta E_g)/du$ ranging from 12 to 32 eV were reported for $CuInSe_2$ and $CuInS_2$.[274,276–278] Furthermore, similar coefficients are predicted for $CuInSe_2$ and $CuGaSe_2$.[277] An intermediate coefficient of $d(\Delta E_g)/du = 20$ eV is thus assumed for all three cation configurations shown in Fig. 42 and the resulting contribution ΔE_g^{Cu-III} to the bandgap bowing is given by

$$\Delta E_g^{Cu-III} = \frac{d(\Delta E_g)}{du} \langle u \rangle_{nl}. \quad (32)$$

Similarly, the bowing contribution ΔE_g^{In-Ga} arising from structural relaxation of the anion with respect to In and Ga atoms can be calculated by

$$\Delta E_g^{In-Ga} = \frac{d(\Delta E_g)}{d\delta_{yz}} \langle \delta_{yz} \rangle \quad (33)$$

in close analogy to Eq. (22) for ternary zincblende alloys in Sec. III E 3. Unfortunately, no predictions are available for the coefficient $d(\Delta E_g)/d\delta_{yz}$ in $CuIn_xGa_{1-x}Se_2$ and $CuIn_xGa_{1-x}S_2$ chalcopyrite alloys. However, the corresponding coefficient $d(\Delta E_g)/d\delta$ for $In_{0.5}Ga_{0.5}P$ and $In_xGa_{1-x}As$ was calculated as 1.5 and 1.2 eV, respectively.[226,229] These two values are very similar to each other despite the different anions of the two materials. Therefore, a similar coefficient of $d(\Delta E_g)/d\delta_{yz} = 1.5$ eV was assumed for $CuIn_xGa_{1-x}Se_2$ and $CuIn_xGa_{1-x}S_2$.[261,262]

Figure 45 plots the bandgap bowing, ΔE_g, versus composition x for $CuIn_xGa_{1-x}Se_2$. Experimentally determined bowing parameters range from 0.15 to 0.26 eV with an average value of $b = 0.20$ eV. The bowing contributions ΔE_g^{Cu-III} and ΔE_g^{In-Ga} calculated according to Eqs. (32) and (33), respectively, and using the values plotted for $\langle u \rangle_{nl}$ and $\langle \delta_{yz} \rangle$ in Fig. 44(c) are also shown.[262] Clearly, structural relaxation of the Se anion with respect to Cu and group-III atoms yields only a small contribution to the experimentally observed bowing despite the remarkable influence of this type of displacement on the bandgap energy. In contrast, structural relaxation of the Se anions with respect to In and Ga atoms constitutes a significant contribution to the bandgap bowing. Naturally, the exact magnitude of this contribution depends on the frequency of occurrence of the mixed configuration and thus differs for a distribution of cation configurations according to the law of mass action and a random distribution of In and Ga atoms. However, the relatively small effect of this type of displacement on the bandgap energy is compensated in both cases by the highly nonlinear dependence of $\langle \delta_{yz} \rangle$ on the composition x thus resulting in a noticeable bowing contribution. A very similar behavior was also observed for $CuIn_xGa_{1-x}S_2$.[262] This clearly demonstrates the strong influence of the atomic-scale

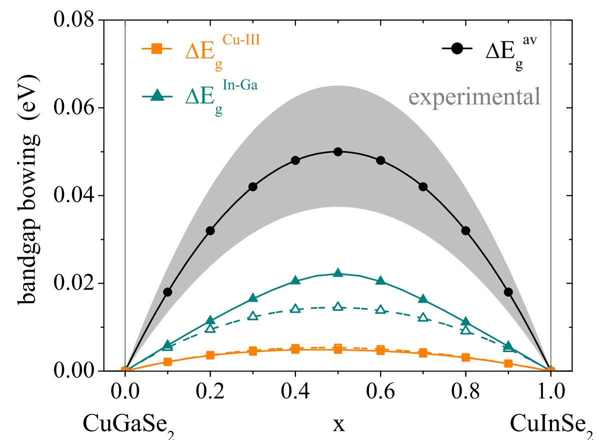

FIG. 45. Bandgap bowing versus composition x for $CuIn_xGa_{1-x}Se_2$.[261,262] The shaded area denotes the range of experimental values reported in the literature[37,38,252,256,257] together with the values corresponding to an average bowing parameter of $b = 0.20$ eV (black circles). The bowing contributions arising from structural relaxation of the Se anion with respect to Cu and group-III atoms ΔE_g^{Cu-III} (orange squares) and with respect to In and Ga atoms ΔE_g^{In-Ga} (cyan triangles) are also plotted. Full and open symbols correspond to a distribution of the different cation configurations according to the law of mass action and to a random distribution, respectively (see Fig. 43).

This article is copyrighted as indicated in the article. Reuse of AIP content is subject to the terms at: http://scitation.aip.org/termsconditions. Downloaded to IP: 131.169.38.71 On: Tue, 17 Nov 2015 09:25:17

structure of quaternary chalcopyrite alloys on important material properties such as the bandgap energy. The presence of two different displacement mechanisms that affect the bowing in very different ways further highlights the increased complexity of the chalcopyrite alloys compared to the III-V and II-VI zincblende alloys.

D. Local electronic states

The atomic-scale structure of the alloy system also affects other properties including the local electronic states as discussed in this section for the example of $CuIn_xGa_{1-x}S_2$.[283] The bandgap energy of this chalcopyrite alloy changes continuously from approximately 2.4 eV for $CuGaS_2$ to about 1.4 eV for $CuInS_2$ (see Table IX). Interestingly, this change is caused mostly by a shift of the conduction band minimum while the valence band maximum remains nearly unaltered.[237,284,285] As a consequence, the energy differences between the core level states and the lowest unoccupied states also change with changing alloy composition x. This variation is expected to result in a shift of the corresponding X-ray absorption edge positions (see also Sec. II). Figure 46 plots the normalized absorption coefficient versus X-ray energy measured at the S and Ga K-edge of $CuGaS_2$, $CuIn_{0.7}Ga_{0.3}S_2$, and $CuInS_2$.[283,285] The position of the S K-edge clearly shifts to lower X-ray energies when the Ga content of the material and thus the bandgap energy is reduced. A similar behavior is also observed for the S L_3-edge.[285] In contrast, no change is observed in the position of the Ga K-edge in Fig. 46(b) or any of the other cation edges studied, namely, the Cu K-edge, the In and Ga L_3-edge, and the In $M_{4,5}$-edge.[285] This means that although the bandgap energy and thus the conduction band minimum change significantly with composition x, only the anion absorption edges exhibit the corresponding shift in position whereas the cation absorption edges remain unchanged. X-ray absorption measurements of $CuIn_xGa_{1-x}Se_2$ (Ref. 261) and $In_xGa_{1-x}P$ (Ref. 78) also show no appreciable shifts of the cation K-edges suggesting that this behavior is characteristic for the tetrahedrally coordinated semiconductor alloys of the adamantine family. As a consequence, the relationship between X-ray absorption edge position and conduction band minimum is far from trivial and care has to be taken when evaluating band structure information based on X-ray absorption spectra.

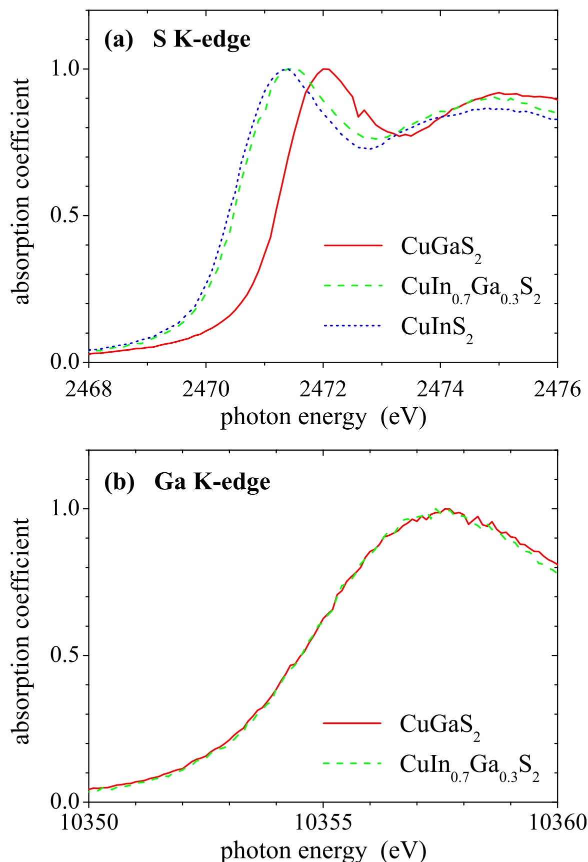

FIG. 46. Normalized X-ray absorption coefficient versus photon energy measured at the (a) S and (b) Ga K-edge of $CuGaS_2$ (solid red line), $CuIn_{0.7}Ga_{0.3}S_2$ (dashed green line), and $CuInS_2$ (dotted blue line).[283,285]

To unravel the origin of this unexpected behavior, density functional theory calculations of the electronic states of $CuIn_xGa_{1-x}S_2$ were performed using special quasi-random structures and a screened hybrid exchange-correlation potential.[283] The application of the latter turns out to be necessary to correctly reproduce both local structural parameters including the element-specific bond lengths and electronic properties such as the bandgap energy. This once more documents the strong correlation between atomic-scale structure and material properties in these semiconductor alloys. The projected partial densities of state (pDOS) were thus calculated for the S, Cu, Ga, and In s, p, and d states.[283] As an example, Fig. 47 plots the pDOS of the S and Ga p states of the conduction band which correspond to the unoccupied states sampled at the S and Ga K-edges shown in Fig. 46. Clearly, the S pDOS shifts with changing composition while the Ga pDOS remains unchanged in excellent agreement with the experimental findings. Similar agreement between the measured X-ray absorption spectra and the calculated pDOS is also observed for the other absorption edges.[283]

The explanation for this somewhat surprising behavior of the absorption edge positions and pDOS can be found in the atomic-scale structure of the $CuIn_xGa_{1-x}S_2$ alloys.[283] All cations are surrounded by four S atoms independent of the composition x (see Fig. 2(f)). Furthermore, the element-specific bond lengths remain nearly constant over the whole compositional range despite the significant change in the lattice constants as discussed in Sec. IV A.[262] The first nearest neighbor structural environment of Cu, In, and Ga is thus nearly independent of the alloy composition and the *element-specific local* electronic states remain almost unchanged. Since the core level electrons are excited predominantly into unoccupied states of the absorbing atom itself, the absorption process is sensitive to these local electronic states. As a consequence, the cation absorption edges do not shift with changing composition. In contrast, the first nearest neighbor environment of the S anions contains two Cu and two group-III atoms and thus changes dramatically with changing In to Ga ratio even if the element-specific bond lengths remain constant. Consequently, the S absorption edges shift with varying alloy composition x. The observed change in the bandgap thus arises from a changing

This article is copyrighted as indicated in the article. Reuse of AIP content is subject to the terms at: http://scitation.aip.org/termsconditions. Downloaded to IP: 131.169.38.71 On: Tue, 17 Nov 2015 09:25:17

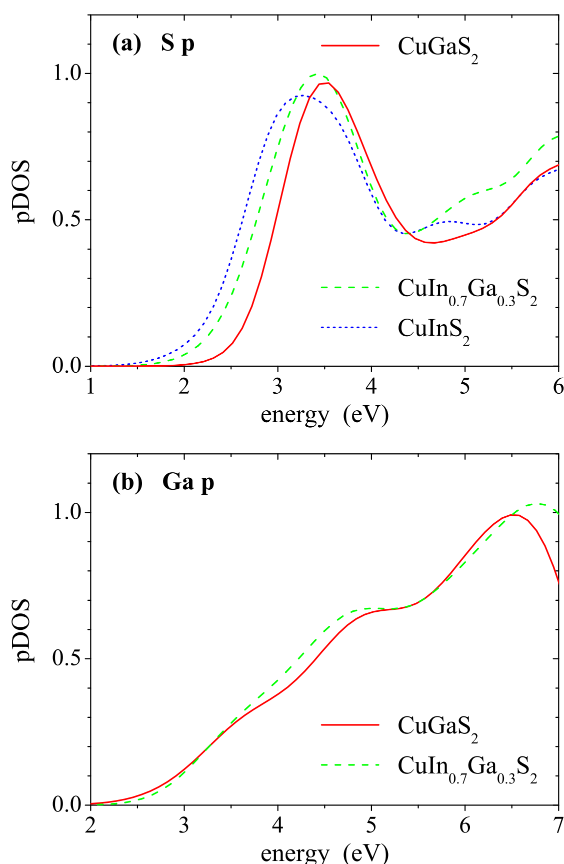

FIG. 47. Calculated projected partial density of states (pDOS) of p states on (a) S and (b) Ga atoms for the conduction band of $CuGaS_2$ (solid red line), $CuIn_{0.7}Ga_{0.3}S_2$ (dashed green line), and $CuInS_2$ (dotted blue line).[283]

spatial average of the nearly unaltered element-specific local states rather than from a change in energy of these states themselves.[283]

A very similar behavior is also observed for Cu-In-Se compounds with different Cu/In ratios varying from 1 ($CuInSe_2$) to 0.2 ($CuIn_5Se_8$).[267] While the position of the Cu and In K-edge is independent of the stoichiometry of the material, the XANES spectra of the Se K-edge exhibit significant changes as the Cu/In ratio decreases. Despite the different crystal structures of the various compounds, the Cu and In cations are always bonded to four Se anions the distance to which varies only little with stoichiometry. The local structural environment of Cu and In, and hence the pDOS, therefore remain mostly unchanged and the X-ray absorption edges do not shift. In contrast, the average first nearest neighbor environment of the Se anions changes remarkably with changing Cu/In ratio as clearly evidenced by the changes in the measured XANES spectra. This strongly suggests that the observed behavior of the absorption edge positions and pDOS in $CuIn_xGa_{1-x}S_2$ alloys and Cu-In-Se compounds is a general feature of tetrahedrally coordinated semiconductors with different cation or anion species and varying composition or stoichiometry. As a consequence, local and global properties have to be distinguished for both the structure of the material and its electronic properties. Just as the short-range atomic-scale structure of semiconductor alloys shows striking deviations from the long-range crystallographic structure, the element-specific local electronic states may differ from the macroscopic electronic properties such as the bandgap energy.

V. CONCLUSIONS AND OUTLOOK

Semiconductor alloys are increasingly employed in numerous electronic, optoelectronic, and photonic devices because their material properties can be specifically tailored over a wide parameter range by adjusting the alloy composition. The alloys typically crystallize in the same crystal structure as the parent compounds and the lattice constants mostly change linearly with alloy composition which is known as Vegard's Law. However, the local atomic arrangements strongly deviate from this average long-range crystallographic structure as demonstrated by X-ray absorption spectroscopy studies of numerous III-V and II-VI zincblende alloys and also some I-III-VI_2 chalcopyrite alloys. In all cases, the element-specific bond lengths are very different from each other and remain close to the values observed for the parent compounds over the whole compositional range. The small and often linear change with alloy composition typically amounts to only 10% to 30% of that expected from the change in lattice constants. In contrast, significant changes are observed for the tetrahedral bond angles. Consequently, some of the atoms are severely displaced from their ideal lattice sites. In particular, strong directional displacements are observed for the atoms occupying the common sublattice while the atoms of the mixed sublattice exhibit significantly smaller and much more isotropic positional variations. Different local atomic arrangements thus coexist in the material, which strongly depend on the nature of the atoms involved. As a consequence, semiconductor alloys are characterized by structural inhomogeneity on the subnanometer scale even if ordering phenomena or compositional fluctuations are absent.

These striking features of the atomic-scale structure of zincblende and chalcopyrite semiconductor alloys were also reproduced by numerous theoretical approaches ranging from simple spring models to sophisticated first-principles density functional theory calculations. In all cases, bimodal bond length distributions were obtained for the mixed sublattice accompanied by severe distortions of the common sublattice and significant variations of the tetrahedral bond angles. The origin of this characteristic behavior is found in the energy required for changing either the bond lengths or the bond angles in these tetrahedrally coordinated systems. As clearly evidenced by the corresponding bond stretching and bond bending force constants, the former requires significantly more energy than the latter. The lattice mismatch in semiconductor alloys is thus accommodated mostly by bond angle relaxation and only to a small extent by bond length relaxation. The balance between these two competing mechanisms is strikingly similar for all III-V, II-VI, and I-III-VI_2 alloys investigated independent of their crystal structure or the chemical nature of their constituent atoms. It can thus be concluded that the energetic preference of bond bending over bond stretching is a fundamental feature of all tetrahedrally coordinated semiconductors of the adamantine

This article is copyrighted as indicated in the article. Reuse of AIP content is subject to the terms at: http://scitation.aip.org/termsconditions. Downloaded to IP: 131.169.38.71 On: Tue, 17 Nov 2015 09:25:17

structural family. As a consequence, very similar features as those discussed above can also be expected for the atomic-scale structure of all other alloy systems belonging to this class of materials, including other I-III-VI_2 chalcopyrites and II-IV-V_2 pnictides but also materials crystallizing in the kesterite or stannite structures such as $Cu_2ZnSn(Se_xS_{1-x})_4$ or $Cu_2FeSn_xGe_{1-x}S_4$.

Interestingly, the local structural parameters, in particular, the atomic displacements, have a strong influence on the bandgap energy. The latter also changes continuously but in most cases nonlinearly with the alloy composition. This bandgap bowing originates from different physical effects, namely, volume deformation, charge redistribution, and structural relaxation. For III-V and II-VI ternary alloys with zincblende structure, the average displacement of the atoms occupying the common sublattice shows a strongly nonlinear dependence on the alloy composition. Structural relaxation therefore represents a significant contribution to the experimentally observed bandgap bowing. Furthermore, there is a strong interplay between the interatomic distances and the charge distribution between the different atoms constituting the alloy system. Based on experimentally determined element-specific bond lengths, it was shown that both structural and electronic changes lead to the nonlinear behavior of the bandgap energy. Charge redistribution, however, is only significant in combination with the unequal bond lengths associated with the mixed sublattice and thus sensitively depends on the atomic-scale structure of the alloy system. For the cation-mixed Cu-III-VI_2 chalcopyrite alloys, the behavior is more complex and two different displacement mechanisms of the anions have to be distinguished. They vary with respect to direction and magnitude of the displacement and both affect the bandgap bowing in a different way. This clearly demonstrates the strong influence of the atomic-scale structure in semiconductor alloys on important material properties, most prominently the bandgap energy. Similar effects can be expected for other tetrahedrally coordinated semiconductors, including but not limited to pnictide, kesterite, or stannite alloys.

In order to get a comprehensive picture of semiconductor alloys, it is thus imperative to fully understand the correlation between local structural parameters on the one hand and electronic and optical material properties on the other hand. Theoretical calculations must correctly reproduce not only the long-range crystallographic structure but also the short-range atomic-scale structure in order to make valid predictions of these material properties. Furthermore, a clear distinction between element-specific local properties and averaged global or macroscopic properties is needed due to the coexistence of different atomic arrangements within the alloy system. Only a comprehensive understanding of this correlation allows to further exploit the full potential of these vast and versatile material systems with increasing compositional and structural complexity.

ACKNOWLEDGMENTS

The author would like to thank her many colleagues listed in the references and P. Fornasini for the excellent collaborations on topics related to this review and for many fruitful discussions. The continued support from various synchrotron light sources including the Photon Factory, Japan, the Australian Synchrotron, Australia, the Deutsche Elektronen-Synchrotron, Germany, the European Synchrotron Radiation Facility, France, and the Swiss Light Source, Switzerland, is gratefully acknowledged. The author's work was further supported by the Australian Research Council, the Australian Synchrotron Research Program, the Carl-Zeiss-Stiftung Germany, the Friedrich-Schiller-Universität Jena, Germany, and the German Federal Ministry for Economic Affairs and Energy. Additional thanks go to S. Eckner for careful reading of the manuscript and C. Ronning for valuable advice and support.

[1]Y. Zhu and M. K. Hudait, Nanotechnol. Rev. **2**, 637 (2013).
[2]Z. Alferov, Proc. IEEE **101**, 2176 (2013).
[3]Y. Yao, A. J. Hoffman, and C. F. Gmachl, Nat. Photonics **6**, 432 (2012).
[4]R. Chen, T.-T. D. Tran, K. W. Ng, W. S. Ko, L. C. Chuang, F. G. Sedgwick, and C. Chang-Hasnain, Nat. Photonics **5**, 170 (2011).
[5]M. A. Itzler, X. Jiang, M. Entwistle, K. Slomkowski, A. Tosi, F. Acerbi, F. Zappa, and S. Cova, J. Mod. Opt. **58**, 174 (2011).
[6]S.-I. Park, A.-P. Le, J. Wu, Y. Huang, X. Li, and J. A. Rogers, Adv. Mater. **22**, 3062 (2010).
[7]S. Mokkapati and C. Jagadish, Mater. Today **12**, 22 (2009).
[8]C. Ghezzi, R. Magnanini, A. Parisini, L. Tarricone, E. Gombia, and M. Longo, Phys. Rev. B **77**, 125317 (2008).
[9]M. Feng, N. Holonyak, Jr., G. Walter, and R. Chan, Appl. Phys. Lett. **87**, 131103 (2005).
[10]M. Razeghi, Eur. Phys. J.: Appl. Phys. **23**, 149 (2003).
[11]F. Dimroth, M. Grave, P. Beutel, U. Fiedeler, C. Karcher, T. N. D. Tibbits, E. Oliva, G. Siefer, M. Schachtner, A. Wekkeli, A. W. Bett, R. Krause, M. Piccin, N. Blanc, C. Drazek, E. Guiot, B. Ghyselen, T. Salvetat, A. Tauzin, T. Signamarcheix, A. Dobrich, T. Hannappel, and K. Schwarzburg, Prog. Photovoltaics **22**, 277 (2014).
[12]H. Cotal, C. Fetzer, J. Boisvert, G. Kinsey, R. King, P. Hebert, H. Yoon, and N. Karam, Energy Environ. Sci. **2**, 174 (2009).
[13]The Nobel Prize in Physics 2014, Nobel Media AB 2014, http://www.nobelprize.org/nobel_prizes/physics/laureates/2014.
[14]A. Rogalski, Rep. Prog. Phys. **68**, 2267 (2005).
[15]A. Singh, V. Srivastav, and R. Pal, Opt. Laser Technol. **43**, 1358 (2011).
[16]P. Martyniuk, J. Antoszewski, M. Martyniuk, L. Faraone, and A. Rogalski, Appl. Phys. Rev. **1**, 041102 (2014).
[17]A. Owens, J. Synchrotron Radiat. **13**, 143 (2006).
[18]S. Del Sordo, L. Abbene, E. Caroli, A. M. Mancini, A. Zappettini, and P. Ubertini, Sensors **9**, 3491 (2009).
[19]Q. Zhang, C. Zhang, Y. Lu, K. Yang, and Q. Ren, Sensors **13**, 2447 (2013).
[20]M. C. Tamargo, W. Lin, S. P. Guo, Y. Guo, Y. Luo, and Y. C. Chen, J. Cryst. Growth **214–215**, 1058 (2000).
[21]X. Wang, X. Ren, K. Kahen, M. A. Hahn, M. Rajeswaran, S. Maccagnano-Zacher, J. Silcox, G. E. Cragg, A. L. Efros, and T. D. Krauss, Nature **459**, 686 (2009).
[22]S. K. Panda, S. G. Hickey, C. Waurisch, and A. Eychmüller, J. Mater. Chem. **21**, 11550 (2011).
[23]P. Jackson, D. Hariskos, R. Wuerz, O. Kiowski, A Bauer, T. M. Friedlmeier, and M. Powalla, Phys. Status Solidi RRL **9**, 28 (2015).
[24]M. Nakamura, N. Yoneyama, K. Horiguchi, Y. Iwata, K. Yamaguchi, H. Sugimoto, and T. Kato, in *Proceedings of the 40th IEEE Photovoltaic Specialists Conference* (2014), p. 0107.
[25]A. Chirilă, P. Reinhard, F. Pianezzi, P. Bloesch, A. R. Uhl, C. Fella, L. Kranz, D. Keller, C. Gretener, H. Hagendorfer, D. Jaeger, R. Erni, S. Nishiwaki, S. Buecheler, and A. N. Tiwari, Nat. Mater. **12**, 1107 (2013).
[26]S. Adachi, *Properties of Semiconductor Alloys: Group-IV, III-V and II-VI Semiconductors* (Wiley, New York, 2009).
[27]B. R. Pamplin, Prog. Cryst. Growth Charact. **1**, 331 (1979).
[28]B. Pamplin, Prog. Cryst. Growth Charact. **3**, 179 (1980).
[29]K. Momma and F. Izumi, J. Appl. Crystallogr. **41**, 653 (2008).
[30]L. Vegard, Z. Phys. **5**, 17 (1921).
[31]J. C. Woolley and B. A. Smith, Proc. Phys. Soc. London **72**, 214 (1958).

This article is copyrighted as indicated in the article. Reuse of AIP content is subject to the terms at: http://scitation.aip.org/termsconditions. Downloaded to IP: 131.169.38.71 On: Tue, 17 Nov 2015 09:25:17

[32]J. C. Mikkelsen and J. B. Boyce, Phys. Rev. B **28**, 7130 (1983).
[33]A. Onton, M. R. Lorenz, and W. Reuter, J. Appl. Phys. **42**, 3420 (1971).
[34]E. K. Müller and J. L. Richards, J. Appl. Phys. **35**, 1233 (1964).
[35]G. Antonioli, S. Bini, P. P. Lottici, and C. Razzetti, J. Phys. **47**, 431 (1986).
[36]D. K. Suri, K. C. Nagpal, and G. K. Chadha, J. Appl. Cryst. **22**, 578 (1989).
[37]T. Tinoco, C. Rincon, M. Quintero, and G. S. Perez, Phys. Status Solidi A **124**, 427 (1991).
[38]C. A. D. Rincon, E. Hernandez, M. I. Alonso, M. Garriga, S. M. Wasim, C. Rincon, and M. Leon, Mater. Chem. Phys. **70**, 300 (2001).
[39]M. R. Balboul, H. W. Schock, S. A. Fayak, A. A. El-Aal, J. H. Werner, and A. A. Ramadan, Appl. Phys. A **92**, 557 (2008).
[40]N. Yamamoto and T. Miyauchi, Jpn. J. Appl. Phys, Part 1 **11**, 1383 (1972).
[41]T. Kato, S. Hayashi, T. Kiuchi, Y. Ishihara, Y. Nabetani, and T. Matsumoto, J. Cryst. Growth **237–239**, 2005 (2002).
[42]K. Oishi, K. Yoneda, O. Yoshida, M. Yamazaki, K. Jimbo, H. Katagiri, H. Araki, S. Kobayashi, and N. Tsuboi, Thin Solid Films **515**, 6265 (2007).
[43]I. V. Bodnar, A. P. Bologa, and B. V. Korzun, Krist. Tech. **15**, 1285 (1980).
[44]Y. D. Themburkar and J. P. Hirde, Bull. Mater. Sci. **15**, 143 (1992).
[45]K. Zeaiter, Y. Llinares, and C. Llinarès, Sol. Energy Mater. Sol. Cells **61**, 313 (2000).
[46]L. Nordheim, Ann. Phys. **401**, 607 and 641 (1931).
[47]L. Pauling and M. L. Huggins, Z. Kristallogr. **87**, 205 (1934).
[48]D. C. Koningsberger and R. Prins, *X-Ray Absorption: Principles, Applications, Techniques of EXAFS, SEXAFS, and XANES* (Wiley, New York, 1988).
[49]G. Bunker, *Introduction to XAFS* (Cambridge University Press, Cambridge, 2010).
[50]S. Calvin, *XAFS for Everyone* (CRC Press, Boca Raton, 2013).
[51]*X-Ray Absorption Spectroscopy of Semiconductors*, Springer Series in Optical Sciences Vol. 190, edited by C. S. Schnohr and M. C. Ridgway (Springer, Berlin, Heidelberg, 2015).
[52]J. C. Woicik, C. E. Bouldin, K. E. Miyano, and C. A. King, Phys. Rev. B **55**, 15386 (1997).
[53]J. C. Woicik, K. E. Miyano, C. A. King, R. W. Johnson, J. G. Pellegrino, T.-L. Lee, and Z. H. Lu, Phys. Rev. B **57**, 14592 (1998).
[54]J. C. Aubry, T. Tyliszczak, A. P. Hitchcock, J. M. Baribeau, and T. E. Jackman, Phys. Rev. B **59**, 12872 (1999).
[55]M. C. Ridgway, K. M. Yu, C. J. Glover, G. J. Foran, C. Clerc, J. L. Hansen, and A. N. Larsen, Phys. Rev. B **60**, 10831 (1999).
[56]I. Yonenaga and M. Sakurai, Phys. Rev. B **64**, 113206 (2001).
[57]Z. H. Sun, W. S. Yan, H. Oyanagi, Z. Y. Pan, and S. Q. Wei, Phys. Rev. B **74**, 092101 (2006).
[58]M. R. Weidmann and K. E. Newman, Phys. Rev. B **45**, 8388 (1992).
[59]N. Mousseau and M. F. Thorpe, Phys. Rev. B **48**, 5172 (1993).
[60]C. S. Schnohr, "Binary and ternary random alloys," in *X-ray Absorption Spectroscopy of Semiconductors*, Springer Series in Optical Sciences Vol. 190, edited by C. S. Schnohr and M. C. Ridgway (Springer, Berlin, Heidelberg, 2015).
[61]S.-H. Wei, D. B. Laks, and A. Zunger, Appl. Phys. Lett. **62**, 1937 (1993).
[62]K. A. Mäder and A. Zunger, Phys. Rev. B **51**, 10462 (1995).
[63]Y. Zhang, A. Mascarenhas, and L.-W. Wang, Phys. Rev. B **63**, 201312 (2001).
[64]S. M. Islam and B. A. Bunker, Phys. Lett. A **156**, 247 (1991).
[65]A. Kisiel, J. Łazewski, M. Zimnal-Starnawska, E. Burattini, and A. Mycielski, Acta Phys. Pol., A **90**, 1032 (1996).
[66]Q. Lu, B. A. Bunker, H. Luo, A. J. Kropf, K. M. Kemner, and J. K. Furdyna, Phys. Rev. B **55**, 9910 (1997).
[67]C. S. Schnohr and M. C. Ridgway, "Introduction to x-ray absorption spectroscopy," in *X-ray Absorption Spectroscopy of Semiconductors*, Springer Series in Optical Sciences Vol. 190, edited by C. S. Schnohr and M. C. Ridgway (Springer, Berlin, Heidelberg, 2015).
[68]J. C. Phillips, *Bonds and Bands in Semiconductors* (Academic, New York, 1973).
[69]J. A. Van Vechten, Phys. Rev. **187**, 1007 (1969).
[70]S. Adachi, *Properties of Group-IV, III-V and II-VI Semiconductors* (Wiley, New York, 2005).
[71]I. Vurgaftman, J. R. Meyer, and L. R. Ram-Mohan, J. Appl. Phys. **89**, 5815 (2001).
[72]R. E. Nahory, M. A. Pollack, and J. C. DeWinter, J. Appl. Phys. **46**, 775 (1975).
[73]D. K. Gaskill, N. Bottka, L. Aina, and M. Mattingly, Appl. Phys. Lett. **56**, 1269 (1990).
[74]T. J. Kim, T. H. Ghong, Y. D. Kim, S. J. Kim, D. E. Aspnes, T. Mori, T. Yao, and B. H. Koo, Phys. Rev. B **68**, 115323 (2003).
[75]J. C. Mikkelsen and J. B. Boyce, Phys. Rev. Lett. **49**, 1412 (1982).
[76]J. B. Boyce and J. C. Mikkelsen, *Ternary and Multinary Compounds* (Materials Research Society, Pittsburgh, 1987), p. 359.
[77]J. B. Boyce and J. C. Mikkelsen, J. Cryst. Growth **98**, 37 (1989).
[78]C. S. Schnohr, L. L. Araujo, P. Kluth, D. J. Sprouster, G. J. Foran, and M. C. Ridgway, Phys. Rev. B **78**, 115201 (2008).
[79]S. Hosokawa, T. Ozaki, N. Takata, N. Happo, H. Ikemoto, T. Shishido, and K. Hayashi, J. Cryst. Growth **311**, 978 (2009).
[80]G. J. Camargo-Gamboa, J. S. Lezama Pacheco, J. Mustre de León, S. D. Conradson, and I. Hernández-Calderón, Thin Solid Films **490**, 165 (2005).
[81]N. Motta, A. Balzarotti, P. Letardi, A. Kisiel, M. T. Czyzyk, M. Zimnal-Starnawska, and M. Podgorny, J. Cryst. Growth **72**, 205 (1985).
[82]N. Motta, A. Balzarotti, P. Letardi, A. Kisiel, M. T. Czyzyk, M. Zimnal-Starnawska, and M. Podgorny, Solid State Commun. **53**, 509 (1985).
[83]P. Letardi, N. Motta, and A. Balzarotti, J. Phys. C **20**, 2853 (1987).
[84]A. Balzarotti, Physica B **146**, 150 (1987).
[85]V. Koteski, H. Haas, E. Holub-Krappe, N. Ivanovic, and H. E. Mahnke, J. Alloys Compd. **371**, 138 (2004).
[86]A. Marbeuf, D. Ballutaud, R. Triboulet, H. Dexpert, P. Lagarde, and Y. Marfaing, J. Phys. Chem. Solids **50**, 975 (1989).
[87]W.-F. Pong, R. A. Mayanovic, and B. A. Bunker, Physica B **158**, 617 (1989).
[88]R. A. Mayanovic, W.-F. Pong, and B. A. Bunker, Phys. Rev. B **42**, 11174 (1990).
[89]T. Sasaki, T. Onda, R. Ito, and N. Ogasawara, Jpn. J. Appl. Phys., Part 1 **25**, 231 (1986).
[90]Z. Wu, K. Lu, Y. Wang, J. Dong, H. Li, C. Li, and Z. Fang, Phys. Rev. B **48**, 8694 (1993).
[91]C.-J. Wu, Z.-C. Feng, W.-M. Chang, C.-C. Yang, and H.-H. Lin, App. Phys. Lett. **101**, 091902 (2012).
[92]J. Pellicer-Porres, A. Polian, A. Segura, V. Muños-Sanjosé, A. Di Cicco, and A. Traverse, J. Appl. Phys. **96**, 1491 (2004).
[93]D. N. Talwar, Z. C. Feng, J.-F. Lee, and P. Becla, Phys. Rev. B **87**, 165208 (2013).
[94]R. A. Mayanovic, W.-F. Pong, and B. A. Bunker, Bull. Am. Phys. Soc. **34**, 593 (1989).
[95]M. Zimnal-Starnawska, J. Łazewski, A. Kisiel, F. Boscherini, S. Pascarelli, and W. Giriat, Acta Phys. Pol., A **86**, 763 (1994).
[96]J. Łazewski, M. Zimnal-Starnawska, A. Kisiel, F. Boscherini, S. Pascarelli, and W. Giriat, Phys. Status Solidi B **197**, 7 (1996).
[97]R. J. Iwanowski, K. Ławniczak-Jabłońska, I. Winter, and J. Hormes, Solid State Commun. **97**, 879 (1996).
[98]B. A. Bunker, J. Vac. Sci. Technol., A **5**, 3003 (1987).
[99]W.-F. Pong, R. A. Mayanovic, B. A. Bunker, J. K. Furdyna, and U. Debska, Phys. Rev. B **41**, 8440 (1990).
[100]N. Happo, H. Sato, T. Mihara, K. Mimura, S. Hosokawa, Y. Ueda, and M. Taniguchi, J. Phys.: Condens. Matter **8**, 4315 (1996).
[101]A. Balzarotti, M. Czyzyk, A. Kisiel, N. Motta, M. Podgórny, and M. Zimnal-Starnawska, Phys. Rev. B **30**, 2295 (1984).
[102]A. Balzarotti, N. Motta, A. Kisiel, M. Zimnal-Starnawska, M. T. Czyżyk, and M. Podgórny, Phys. Rev. B **31**, 7526 (1985).
[103]N. Liu, C. K. Shih, J. Geisz, A. Mascarenhas, and J. M. Olson, Appl. Phys. Lett. **73**, 1979 (1998).
[104]B. Grandidier, H. Chen, R. M. Feenstra, D. T. McInturff, P. W. Juodawlkis, and S. E. Ralph, Appl. Phys. Lett. **74**, 1439 (1999).
[105]R. Carles, G. Landa, and J. B. Renucci, Solid State Commun. **53**, 179 (1985).
[106]D. N. Talwar, K. S. Suh, and C. S. Ting, Philos. Mag. **56**, 593 (1987).
[107]J. Groenen, R. Carles, G. Landa, C. Guerret-Piécourt, C. Fontaine, and M. Gendry, Phys. Rev. B **58**, 10452 (1998).
[108]A. V. Postnikov, O. Pagès, and J. Hugel, Phys. Rev. B **71**, 115206 (2005).
[109]O. Pagès, A. Chafi, D. Fristot, and A. V. Postnikov, Phys. Rev. B **73**, 165206 (2006).
[110]O. Pagès, T. Tite, K. Kim, P. A. Graf, O. Maksimov, and M. C. Tamargo, J. Phys.: Condens. Matter **18**, 577 (2006).
[111]O. Pagès, A. V. Postnikov, M. Kassem, A. Chafi, A. Nassour, and S. Doyen, Phys. Rev. B **77**, 125208 (2008).

This article is copyrighted as indicated in the article. Reuse of AIP content is subject to the terms at: http://scitation.aip.org/termsconditions. Downloaded to IP: 131.169.38.71 On: Tue, 17 Nov 2015 09:25:17

[112]O. Pagès, J. Souhabi, A. V. Postnikov, and A. Chafi, Phys. Rev. B **80**, 035204 (2009).
[113]V. Petkov, I.-K. Jeong, J. S. Chung, M. F. Thorpe, S. Kycia, and S. J. L. Billinge, Phys. Rev. Lett. **83**, 4089 (1999).
[114]V. Petkov and S. J. L. Billinge, Physica B **305**, 83 (2001).
[115]I.-K. Jeong, F. Mohiuddin-Jacobs, V. Petkov, S. J. L. Billinge, and S. Kycia, Phys. Rev. B **63**, 205202 (2001).
[116]Y. Kuwahara, H. Oyanagi, R. Shioda, Y. Takeda, H. Yamaguchi, and M. Aono, Jpn. J. Appl. Phys., Part 1 **33**, 5631 (1994).
[117]M. Tabuchi, T. Kumamoto, and Y. Takeda, J. Appl. Phys. **77**, 143 (1995).
[118]J. C. Woicik, J. G. Pellegrino, B. Steiner, K. E. Miyano, S. G. Bompadre, L. B. Sorensen, T. L. Lee, and S. Khalid, Phys. Rev. Lett. **79**, 5026 (1997).
[119]S. Pascarelli, F. Boscherini, C. Lamberti, and S. Mobilio, Phys. Rev. B **56**, 1936 (1997).
[120]J. C. Woicik, J. A. Gupta, S. P. Watkins, and E. D. Crozier, Appl. Phys. Lett. **73**, 1269 (1998).
[121]J. C. Woicik, J. O. Cross, C. E. Bouldin, B. Ravel, J. G. Pellegrino, B. Steiner, S. G. Bompadre, L. B. Sorensen, K. E. Miyano, and J. P. Kirkland, Phys. Rev. B **58**, R4215 (1998).
[122]F. Romanato, D. De Salvador, M. Berti, A. Drigo, M. Natali, M. Tormen, G. Rossetto, S. Pascarelli, F. Boscherini, C. Lamberti, and S. Mobilio, Phys. Rev. B **57**, 14619 (1998).
[123]F. Boscherini, C. Lamberti, S. Pascarelli, C. Rigo, and S. Mobilio, Phys. Rev. B **58**, 10745 (1998).
[124]M. Tormen, D. De Salvador, M. Natali, A. Drigo, F. Romanato, G. Rossetto, F. Boscherini, and S. Mobilio, J. Appl. Phys. **86**, 2533 (1999).
[125]G. Ciatto, F. D'Acapito, S. Sanna, V. Fiorentini, A. Polimeni, M. Capizzi, S. Mobilio, and F. Boscherini, Phys. Rev. B **71**, 115210 (2005).
[126]J. C. Woicik, Surf. Sci. Rep. **69**, 38 (2014).
[127]K. E. Miyano, J. C. Woicik, L. H. Robins, C. E. Bouldin, and D. K. Wickenden, Appl. Phys. Lett. **70**, 2108 (1997).
[128]K. M. Yu, W. Shan, C. J. Glover, M. C. Ridgway, W. S. Wong, and W. Yang, Appl. Phys. Lett. **75**, 4097 (1999).
[129]M. Katsikini, E. C. Paloura, F. Boscherini, F. D'Acapito, C. B. Lioutas, and D. Doppalapudi, Nucl. Instrum. Methods B **200**, 114 (2003).
[130]V. Kachkanov, K. P. O'Donnell, R. W. Martin, J. F. W. Mosselmans, and S. Pereira, Appl. Phys. Lett. **89**, 101908 (2006).
[131]J. C. Woicik, K. F. Ludwig, Jr., and T. D. Moustakas, Appl. Phys. Lett. **100**, 162105 (2012).
[132]J. B. Boyce and J. C. Mikkelsen, Phys. Rev. B **31**, 6903 (1985).
[133]A. Di Cicco, E. Principi, and A. Filipponi, Phys. Rev. B **65**, 212106 (2002).
[134]Z. S. Hussain, E. Wendler, W. Wesch, G. J. Foran, C. S. Schnohr, D. J. Llewellyn, and M. C. Ridgway, Phys. Rev. B **79**, 085202 (2009).
[135]M. Tormen, D. De Salvador, A. V. Drigo, F. Romanato, F. Boscherini, and S. Mobilio, Phys. Rev. B **63**, 115326 (2001).
[136]S. Hosokawa, N. Happo, T. Ozaki, H. Ikemoto, T. Shishido, and K. Hayashi, Phys. Rev. B **87**, 094104 (2012).
[137]J. G. Kirkwood, J. Chem. Phys. **7**, 506 (1939).
[138]M. J. P. Musgrave and J. A. Pople, Proc. R. Soc. London, Ser. A **268**, 474 (1962).
[139]P. N. Keating, Phys. Rev. **145**, 637 (1966).
[140]R. M. Martin, Phys. Rev. B **1**, 4005 (1970).
[141]H. Neumann, Cryst. Res. Technol. **20**, 773 (1985).
[142]Y. Cai and M. F. Thorpe, Phys. Rev. B **46**, 15879 (1992).
[143]J. L. Martins and A. Zunger, Phys. Rev. B **30**, 6217 (1984).
[144]A.-B. Chen and A. Sher, Phys. Rev. B **32**, 3695 (1985).
[145]H. Neumann, Cryst. Res. Technol. **24**, 325 (1989).
[146]A. S. Verma, Phys. Lett. A **372**, 7196 (2008).
[147]M. Bettini, Phys. Status Solidi B **69**, 201 (1975).
[148]W. H. Koschel and M. Bettini, Phys. Status Solidi B **72**, 729 (1975).
[149]H. Neumann, Helv. Phys. Acta **58**, 337 (1985).
[150]H. Neumann, Cryst. Res. Technol. **24**, 619 (1989).
[151]S. Nomura and S. Endo, J. Cryst. Growth **237–239**, 2014 (2002).
[152]G. Dalba and P. Fornasini, J. Synchrotron Radiat. **4**, 243 (1997).
[153]G. Beni and P. M. Platzman, Phys. Rev. B **14**, 1514 (1976).
[154]E. Sevillano, H. Meuth, and J. J. Rehr, Phys. Rev. B **20**, 4908 (1979).
[155]G. Dalba, P. Fornasini, R. Grisenti, and J. Purans, Phys. Rev. Lett. **82**, 4240 (1999).
[156]P. Fornasini, F. Monti, and A. Sanson, J. Synchrotron Radiat. **8**, 1214 (2001).
[157]P. Fornasini, S. A. Beccara, G. Dalba, R. Grisenti, A. Sanson, M. Vaccari, and F. Rocca, Phys. Rev. B **70**, 174301 (2004).
[158]M. Vaccari and P. Fornasini, J. Synchrotron Radiat. **13**, 321 (2006).
[159]G. Dalba, P. Fornasini, M. Grazioli, and F. Rocca, Phys. Rev. B **52**, 11034 (1995).
[160]P. Fornasini, "Vibrational anisotropy," in *X-ray Absorption Spectroscopy of Semiconductors*, Springer Series in Optical Sciences Vol. 190, edited by C. S. Schnohr and M. C. Ridgway (Springer, Berlin, Heidelberg, 2015).
[161]A. I. Frenkel and J. J. Rehr, Phys. Rev. B **48**, 585 (1993).
[162]T. Yokoyama, J. Synchrotron Radiat. **6**, 323 (1999).
[163]C. S. Schnohr, P. Kluth, L. L. Araujo, D. J. Sprouster, A. P. Byrne, G. J. Foran, and M. C. Ridgway, Phys. Rev. B **79**, 195203 (2009).
[164]C. S. Schnohr, P. Kluth, A. P. Byrne, G. J. Foran, and M. C. Ridgway, Phys. Rev. B **77**, 073204 (2008).
[165]M. C. Ridgway, C. J. Glover, K. M. Yu, G. J. Foran, C. Clerc, J. L. Hansen, and A. N. Larsen, Phys. Rev. B **61**, 12586 (2000).
[166]G. de M. Azevedo, C. J. Glover, M. C. Ridgway, K. M. Yu, and G. J. Foran, Phys. Rev. B **68**, 115204 (2003).
[167]S. I. Ahmed, G. Aquilanti, N. Novello, L Olivi, R. Grisenti, and P. Fornasini, J. Chem. Phys. **139**, 164512 (2013).
[168]N. Abd el All, B. Thiodjio Sendja, R. Grisenti, F. Rocca, D. Diop, O. Mathon, S. Pascarelli, and P. Fornasini, J. Synchrotron Radiat. **20**, 603 (2013).
[169]C. S. Schnohr, L. L. Araujo, and M. C. Ridgway, J. Phys. Soc. Jpn., Part 1 **83**, 094602 (2014).
[170]M. Krbal, A. V. Kolobov, B. Hyot, B. Andre, P. Fons, R. E. Simpson, T. Uruga, H. Tanida, and J. Tominaga, J. Appl. Phys. **108**, 023506 (2010).
[171]J. Purans, N. D. Afify, G. Dalba, R. Grisenti, S. De Panfilis, A. Kuzmin, V. I. Ozhogin, F. Rocca, A. Sanson, S. I. Tiutiunnikov, and P. Fornasini, Phys. Rev. Lett. **100**, 055901 (2008).
[172]G. Dalba, D. Diop, P. Fornasini, and F. Rocca, J. Phys.: Condens. Matter **6**, 3599 (1994).
[173]G. Dalba, P. Fornasini, R. Grisenti, D. Pasqualini, D. Diop, and F. Monti, Phys. Rev. B **58**, 4793 (1998).
[174]N. Abd el All, G. Dalba, D. Diop, P. Fornasini, R. Grisenti, O. Mathon, F. Rocca, B. T. Sendja, and M. Vaccari, J. Phys.: Condens. Matter **24**, 115403 (2012).
[175]W. Bohmer and P. Rabe, J. Phys. C **12**, 2465 (1979).
[176]M. Schowalter, A. Rosenauer, J. T. Titantah, and D. Lamoen, Acta Crystallogr. A **65**, 5 (2009).
[177]J. S. Reid, Acta Crystallogr. A **39**, 1 (1983).
[178]G. D. Barrera, J. A. O. Bruno, T. H. K. Barron, and N. L. Allan, J. Phys.: Condens. Matter **17**, R217 (2005).
[179]P. Fornasini, S. I. Ahmed, A. Sanson, and M. Vaccari, Phys. Status Solidi B **245**, 2497 (2008).
[180]C. K. Shih, W. E. Spicer, W. A. Harrison, and A. Sher, Phys. Rev. B **31**, 1139 (1985).
[181]K. Biswas, A. Franceschetti, and S. Lany, Phys. Rev. B **78**, 085212 (2008).
[182]M. C. Schabel and J. L. Martins, Phys. Rev. B **43**, 11873 (1991).
[183]A. Silverman, A. Zunger, R. Kalish, and J. Adler, Phys. Rev. B **51**, 10795 (1995).
[184]G. P. Srivastava, J. L. Martins, and A. Zunger, Phys. Rev. B **31**, 2561 (1985).
[185]C. S. Schnohr, J. Phys.: Condens. Matter **24**, 325802 (2012).
[186]J. C. Woicik, Phys. Rev. B **57**, 6266 (1998).
[187]J. C. Woicik, J. Appl. Phys. **112**, 113515 (2012).
[188]M. F. Thorpe and E. J. Garboczi, Phys. Rev. B **42**, 8405 (1990).
[189]Y. Cai and M. F. Thorpe, Phys. Rev. B **46**, 15872 (1992).
[190]M. Podgórny, M. T. Czyżyk, A. Balzarotti, P. Letardi, N. Motta, A. Kisiel, and M. Zimnal-Starnawska, Solid State Commun. **55**, 413 (1985).
[191]R. B. Capaz and B. Koiller, Phys. Rev. B **47**, 4044 (1993).
[192]Y. Zhang, A. Mascarenhas, and L.-W. Wang, Phys. Rev. B **64**, 125207 (2001).
[193]L. Bellaiche, S.-H. Wei, and A. Zunger, Phys. Rev. B **54**, 17568 (1996).
[194]Z. Q. Li and W. Pötz, Phys. Rev. B **46**, 2109 (1992).
[195]P. S. Branicio, R. K. Kalia, A. Nakano, J. P. Rino, F. Shimojo, and P. Vashishta, Appl. Phys. Lett. **82**, 1057 (2003).
[196]P. S. Branicio, J. P. Rino, F. Shimojo, R. K. Kalia, A. Nakano, and P. Vashishta, J. Appl. Phys. **94**, 3840 (2003).
[197]J. T. Titantah, D. Lamoen, M. Schowalter, and A. Rosenauer, J. Appl. Phys. **101**, 123508 (2007).
[198]C. Alibert and G. Bordure, Phys. Rev. B **6**, 1301 (1972).
[199]R. J. Nelson and N. Holonyak, Jr., J. Phys. Chem. Solids **37**, 629 (1976).
[200]H. Lange, J. Donecker, and H. Friedrich, Phys. Status Solidi B **73**, 633 (1976).

This article is copyrighted as indicated in the article. Reuse of AIP content is subject to the terms at: http://scitation.aip.org/termsconditions. Downloaded to IP: 131.169.38.71 On: Tue, 17 Nov 2015 09:25:17

[201]J. E. Bernard and A. Zunger, Phys. Rev. B **36**, 3199 (1987).
[202]J. A. Van Vechten and T. K. Bergstresser, Phys. Rev. B **1**, 3351 (1970).
[203]D. Richardson and R. Hill, J. Phys. C **5**, 821 (1972).
[204]D. Richardson, J. Phys. C **4**, L289 (1971).
[205]R. Hill and D. Richardson, J. Phys. C **4**, L339 (1971).
[206]J. F. Hunter, G. Ball, and D. J. Morgan, Phys. Status Solidi B **45**, 679 (1971).
[207]R. Hill, J. Phys. C **7**, 521 (1974).
[208]K.-R. Schulze, H. Neumann, and K. Unger, Phys. Status Solidi B **75**, 493 (1976).
[209]A. Baldereschi, E. Hess, K. Maschke, H. Neumann, K.-R. Schulze, and K. Unger, J. Phys. C **10**, 4709 (1977).
[210]D. J. Chadi, Phys. Rev. B **16**, 790 (1977).
[211]A.-B. Chen and A. Sher, Phys. Rev. B **22**, 3886 (1980).
[212]W. Porod, D. K. Ferry, and K. A. Jones, J. Vac. Sci. Technol. **21**, 965 (1982).
[213]N. Tit, I. M. Obaidat, and H. Alawadhi, J. Phys.: Condens. Matter **21**, 075802 (2009).
[214]D. Stroud, Phys. Rev. B **5**, 3366 (1972).
[215]E. D. Siggia, Phys. Rev. B **10**, 5147 (1974).
[216]A. Baldereschi and K. Maschke, Solid State Commun. **16**, 99 (1975).
[217]A.-B. Chen and A. Sher, Phys. Rev. Lett. **40**, 900 (1978).
[218]A.-B. Chen and A. Sher, Phys. Rev. B **17**, 4726 (1978).
[219]S. Sakai and T. Sugano, J. Appl. Phys. **50**, 4143 (1979).
[220]A.-B. Chen and A. Sher, Phys. Rev. B **23**, 5360 (1981).
[221]H. Ehrenreich and K. C. Hass, J. Vac. Sci. Technol. **21**, 133 (1982).
[222]M. Bugajski, A. M. Kontkiewicz, and H. Mariette, Phys. Rev. B **28**, 7105 (1983).
[223]K. C. Hass, H. Ehrenreich, and B. Velický, Phys. Rev. B **27**, 1088 (1983).
[224]K. C. Hass, R. J. Lempert, and H. Ehrenreich, Phys. Rev. Lett. **52**, 77 (1984).
[225]R. J. Lempert, K. C. Hass, and H. Ehrenreich, Phys. Rev. B **36**, 1111 (1987).
[226]A. Zunger and J. E. Jaffe, Phys. Rev. Lett. **51**, 662 (1983).
[227]J. E. Bernard and A. Zunger, Phys. Rev. B **34**, 5992 (1986).
[228]S.-H. Wei and A. Zunger, Phys. Rev. B **39**, 6279 (1989).
[229]R. Magri, S. Froyen, and A. Zunger, Phys. Rev. B **44**, 7947 (1991).
[230]S.-H. Wei, S. B. Zhang, and A. Zunger, J. Appl. Phys. **87**, 1304 (2000).
[231]T. B. Boykin, N. Kharche, G. Klimeck, and M. Korkusinski, J. Phys.: Condens. Matter **19**, 036203 (2007).
[232]D. Mourad, G. Czycholl, C. Kruse, S. Klembt, R. Retzlaff, D. Hommel, M. Gartner, and M. Anastasescu, Phys. Rev. B **82**, 165204 (2010).
[233]A. Zunger, S.-H. Wei, L. G. Ferreira, and J. E. Bernard, Phys. Rev. Lett. **65**, 353 (1990).
[234]S.-H. Wei, L. G. Ferreira, J. E. Bernard, and A. Zunger, Phys. Rev. B **42**, 9622 (1990).
[235]K. C. Hass, L. C. Davis, and A. Zunger, Phys. Rev. B **42**, 3757 (1990).
[236]S.-H. Wei and A. Zunger, Phys. Rev. B **43**, 1662 (1991).
[237]S.-H. Wei and A. Zunger, J. Appl. Phys. **78**, 3846 (1995).
[238]D. B. Laks, S.-H. Wei, and A. Zunger, Phys. Rev. Lett. **69**, 3766 (1992).
[239]K. A. Mäder and A. Zunger, Appl. Phys. Lett. **64**, 2882 (1994).
[240]S.-H. Wei and A. Zunger, Phys. Rev. Lett. **76**, 664 (1996).
[241]M. Weyers, M. Sato, and H. Ando, Jpn. J. Appl. Phys., Part 2 **31**, L853 (1992).
[242]W. Walukiewicz, W. Shan, K. M. Yu, J. W. Ager III, E. E. Haller, I. Miotkowski, M. J. Seong, H. Alawadhi, and A. K. Ramdas, Phys. Rev. Lett. **85**, 1552 (2000).
[243]W. Shan, W. Walukiewicz, J. W. Ager III, E. E. Haller, J. F. Geisz, D. J. Friedman, J. M. Olson, and S. R. Kurtz, Phys. Rev. Lett. **82**, 1221 (1999).
[244]H. Müller, R. Trommer, M. Cardona, and P. Vogl, Phys. Rev. B **21**, 4879 (1980).
[245]S. Ves, K. Strössner, C. K. Kim, and M. Cardona, Solid State Commun. **55**, 327 (1985).
[246]H. Hahn, G. Frank, W. Klingler, A.-D. Meyer, and G. Störger, Z. Anorg. Allg. Chem. **271**, 153 (1953).
[247]H. W. Spiess, U. Haeberlen, G. Brandt, A. Räuber, and J. Schneider, Phys. Status Solidi B **62**, 183 (1974).
[248]S. C. Abrahams and J. L. Bernstein, J. Chem. Phys. **59**, 5415 (1973).
[249]S. C. Abrahams and J. L. Bernstein, J. Chem. Phys. **61**, 1140 (1974).
[250]J. Parkes, R. D. Tomlinson, and M. J. Hampshire, J. Appl. Cryst. **6**, 414 (1973).
[251]I. V. Bodnar, B. V. Korzun, and A. I. Lukomskii, Phys. Status Solidi B **105**, K143 (1981).
[252]I. V. Bodnar, A. P. Bologa, and B. V. Korzun, Phys. Status Solidi B **109**, K31 (1982).
[253]M. Quintero and J. C. Woolley, J. Appl. Phys. **55**, 2825 (1984).
[254]I. V. Bodnar and A. I. Lukomskii, Phys. Status Solidi A **98**, K165 (1986).
[255]S. Chichibu, T. Mizutani, K. Murakami, T. Shioda, T. Kurafuji, H. Nakanishi, S. Niki, P. J. Fons, and A. Yamada, J. Appl. Phys. **83**, 3678 (1998).
[256]K. Yoshino, M. Iwamoto, H. Yokoyama, A. Fukuyama, K. Maeda, S. Niki, and T. Ikari, Jpn. J. Appl. Phys., Part 1 **38**, 3171 (1999).
[257]P. D. Paulson, R. W. Birkmire, and W. N. Shafarman, J. Appl. Phys. **94**, 879 (2003).
[258]S. Shirakata, A. Ogawa, S. Isomura, and T. Kariya, Jpn. J. Appl. Phys., Part 1 **32–33**, 94 (1993).
[259]L. Roa, C. Rincon, J. Gonzalez, and M. Quintero, J. Phys. Chem. Solids **51**, 551 (1990).
[260]S.-H. Wei, S. B. Zhang, and A. Zunger, Appl. Phys. Lett. **72**, 3199 (1998).
[261]C. S. Schnohr, H. Kämmer, C. Stephan, S. Schorr, T. Steinbach, and J. Rensberg, Phys. Rev. B **85**, 245204 (2012).
[262]S. Eckner, H. Kämmer, T. Steinbach, M. Gnauck, A. Johannes, C. Stephan, S. Schorr, and C. S. Schnohr, Appl. Phys. Lett. **103**, 081905 (2013).
[263]C. S. Schnohr, H. Kämmer, T. Steinbach, M. Gnauck, T. Rissom, C. A. Kaufmann, C. Stephan, and S. Schorr, Thin Solid Films **582**, 356 (2015).
[264]V. Koteski, S. Doka-Yamigno, J. Hofstetter, M. Rusu, H. E. Mahnke, M. Ch. Lux-Steiner, Th. Schedel-Niedrig, and E. Arushanov, Phys. Rev. B **81**, 245213 (2010).
[265]Y. Kuwahara, H. Oyanagi, H. Yamaguchi, M. Aono, S. Shirakata, and S. Isomura, J. Appl. Phys. **76**, 7864 (1994).
[266]J. M. Merino, S. Díaz-Moreno, G. Subías, and M. León, Thin Solid Films **480–481**, 295 (2005).
[267]S. Yamazoe, H. Kou, and T. Wada, J. Mater. Res. **26**, 1504 (2011).
[268]H. Neumann, Cryst. Res. Technol. **18**, 1299 (1983).
[269]A. S. Verma, Solid State Commun. **149**, 1236 (2009).
[270]P. P. Lottici, G. Antonioli, and C. Razzetti, Phys. Rev. B **37**, 9017 (1988).
[271]R. Shioda, Y. Okada, H. Oyanagi, S. Niki, A. Yamada, and Y. Makita, J. Cryst. Growth **150**, 1196 (1995).
[272]C. D. R. Ludwig, T. Gruhn, C. Felser, T. Schilling, J. Windeln, and P. Kratzer, Phys. Rev. Lett. **105**, 025702 (2010).
[273]V. V. Kindyak, A. S. Kindyak, V. F. Gremenok, and I. A. Victorov, Thin Solid Films **293**, 75 (1997).
[274]J. E. Jaffe and A. Zunger, Phys. Rev. B **27**, 5176 (1983).
[275]J. E. Jaffe and A. Zunger, Phys. Rev. B **28**, 5822 (1983).
[276]J. E. Jaffe and A. Zunger, Phys. Rev. B **29**, 1882 (1984).
[277]S.-H. Wei, A. Zunger, I. H. Choi, and P. Y. Yu, Phys. Rev. B **58**, R1710 (1998).
[278]J. Vidal, S. Botti, P. Olsson, J.-F. Guillemoles, and L. Reining, Phys. Rev. Lett. **104**, 056401 (2010).
[279]T. Tinoco, M. Quintero, and C. Rincón, Phys. Rev. B **44**, 1613 (1991).
[280]L. K. Samanta, D. K. Ghosh, and G. C. Bhar, Phys. Rev. B **33**, 4145 (1986).
[281]L. K. Samanta, D. K. Ghosh, and G. C. Bhar, Phys. Rev. B **35**, 4519 (1987).
[282]S. Y. Chen, X. G. Gong, and S.-H. Wei, Phys. Rev. B **75**, 205209 (2007).
[283]R. Sarmiento-Pérez, S. Botti, C. S. Schnohr, I. Lauermann, A. Rubio, and B. Johnson, J. App. Phys. **116**, 093703 (2014).
[284]M. Turcu, I. M. Kötschau, and U. Rau, Appl. Phys. A **73**, 769 (2001).
[285]B. Johnson, J. Klaer, S. Merdes, M. Gorgoi, B. Höpfner, A. Vollmer, and I. Lauermann, J. Electron Spectrosc. Relat. Phenom. **190A**, 42 (2013).

This article is copyrighted as indicated in the article. Reuse of AIP content is subject to the terms at: http://scitation.aip.org/termsconditions. Downloaded to IP: 131.169.38.71 On: Tue, 17 Nov 2015 09:25:17